PE&RS

LANDSAT'S ENDURING LEGACY

PIONEERING GLOBAL LAND OBSERVATIONS FROM SPACE
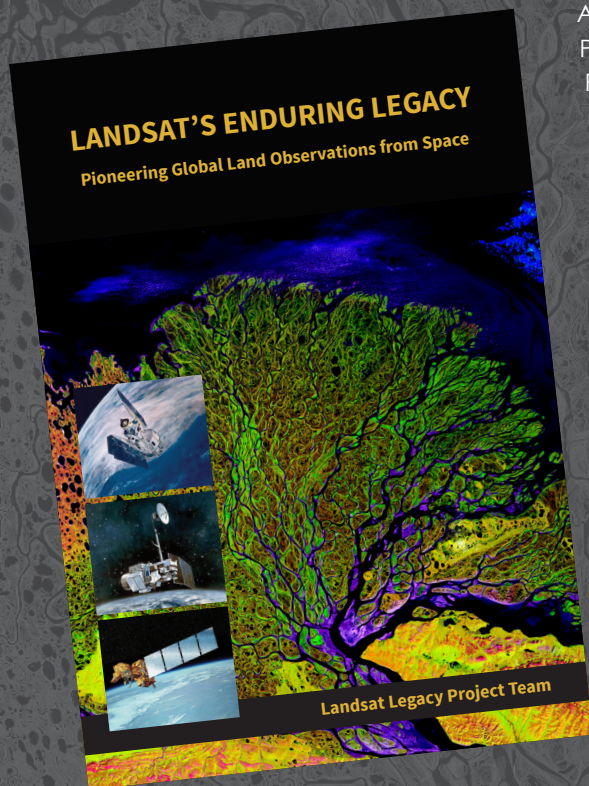
After more than 15 years of research and writing, the Landsat Legacy Project Team published, in collaboration with the American Society for Photogrammetry and Remote Sensing (ASPRS), a seminal work on the nearly half-century of monitoring the Earth's lands with Landsat. Born of technologies that evolved from the Second World War, Landsat not only pioneered global land monitoring but in the process drove innovation in digital imaging technologies and encouraged development of global imagery archives. Access to this imagery led to early breakthroughs in natural resources assessments, particularly for agriculture, forestry, and geology. The technical Landsat remote sensing revolution was not simple or straightforward. Early conflicts between civilian and defense satellite remote sensing users gave way to disagreements over whether the Landsat system should be a public service or a private enterprise. The failed attempts to privatize Landsat nearly led to its demise. Only the combined engagement of civilian and defense organizations ultimately saved this pioneer satellite land monitoring program. With the emergence of 21st century Earth system science research, the full value of the Landsat concept and its continuous 45-year global archive has been recognized and embraced. Discussion of Landsat's future continues but its heritage will not be forgotten.

The pioneering satellite system's vital history is captured in this notable volume on Landsat's Enduring Legacy.

Landsat Legacy Project Team

Samuel N. Goward
Darrel L. Williams
Terry Arvidson
Laura E. P. Rocchio
James R. Irons
Carol A. Russell
Shaida S. Johnston

Landsat's Enduring Legacy

Hardback. 2017, ISBN 1-57083-101-7

Student	$36*
Member	$48*
Non-member	$60*

* Plus shipping

Order online at
www.asprs.org/landsat

INDUSTRYNEWS

ANNOUNCEMENTS

Teledyne Geospatial is pleased to announce that the next generation Optech CZMIL SuperNova topo/bathy lidar system has been awarded both the Geospatial Excellence Award for Technology Innovation and the Geospatial Excellence - Project of the Year Grand Award.

The Optech CZMIL SuperNova boasts the best depth performance and the highest green laser point density in its class. With SmartSpacing technology for even and efficient point spacing, real-time processing capability for reduced post-processing time and configurable modes for maximizing performance in different water environments, the SuperNova provides a wide range of inputs for climate change modelling and is Ideal for inland water environments, base mapping for coastal zones and shoreline.

A true geospatial solution, the CZMIL SuperNova's workflow is integrated with CARIS Base Editor software for seamless data processing capability and built-in AI techniques for land/water classification.

Teledyne Geospatial Director of Product Management Karen Cove comments, "We are thrilled to have the CZMIL Super-Nova recognized by MAPPS and excited to see customers like Dewberry and Terratec tackle challenging projects with its demonstrated efficacy in environments like coastal beaches, inland waterways, coral reefs and deep-water mapping."

Teledyne Geospatial unifies the hardware and software expertise of both Teledyne CARIS and Teledyne Optech. The new group provides customers with innovative integrated solutions. Offerings include turnkey systems, lidar and sonar integrated workflows and a range of systems and solutions that support holistic, precision data collection.

❧

NCEES seeks professional surveyors' and mapping scientists' expertise and advice NCEES is currently seeking licensed professional surveyors and mapping scientists to participate in a professional activities and knowledge study, or PAKS, for the Principles and Practice of Surveying (PS) exam. The results of this study will be used to update the specifications for the exam, which is used throughout the United States for licensing purposes.

NCEES requires a cross section of licensed professional surveyors and mapping scientists—including those working in consulting, the public sector, and academia—to complete an online questionnaire about the knowledge, skills, and abilities required of a newly licensed surveyor or mapping scientist to practice in a manner that safeguards the health, safety, and welfare of the public. The questionnaire can be completed in 35–45 minutes.

"These studies help NCEES ensure its licensing exams reflect current professional practice," explained Chief Officer of Examinations Jason J. Gamble, P.E. "We need input from as many professional surveyors and mapping scientists as possible to ensure that the PS exam continues to meet the demands of the profession."

For access to the online questionnaire, visit ncees.org/PSPAKS. Responses must be received no later than May 30, 2022. For more information, contact NCEES Exam Development Engineer John (Andy) Bindewald, P.E., at abindewald@ncees.org.

❧

LAND INFO Worldwide Mapping LLC recently completed up-to-date 10m resolution thematic raster GIS data covering all 50 U.S. states. Optimized for low-band (broad-area coverage) 5G wireless planning, the dataset supports additional applications including utilities, insurance and government, and complements LAND INFO's 1m resolution datasets that are used for mid-band and high-band 5G in more densely populated areas.

"The dataset is unique in that in addition to using 2020-2021 Sentinel imagery and numerous ancillary layers, we were able to create best-in-class mapping by incorporating into our processing aerial-derived Digital Surface Model (DSM) elevation data via our longstanding partnership with Hexagon's HxGN Content Program," said LAND INFO president Nick Hubing.

The HxGN Content Program offers high-resolution, countrywide aerial imagery and elevation data of the contiguous United States and Western European countries. Hexagon continuously advances the program with higher resolution products for digital twin initiatives.

"We are proud to support LAND INFO's land-use/cover mapping solution with our high-quality DSMs," says John Welter, President, Geospatial Content Solutions at Hexagon. "LAND INFO is a well-established partner of Hexagon, and the partnership enables various industries to gain real-world analytics for reliable insights and better-informed decision making."

LAND INFO's proprietary automated geospatial processing technologies include object-based image analysis and artificial intelligence where smart rulesets analyzed, classified, and merged the imagery, DSM and ancillary layers into a single information rich dataset. There are currently just over 20 classes, and additional classes can be added upon request.

Visit www.landinfo.com for more information.

TECHNOLOGY

Phase One, a leading developer of digital imaging technologies, has announced its new iX Suite, a fully integrated software package for aerial mapping project management. Compatible with all Phase One PAS airborne systems, iX Suite handles mission planning, flight management, data acquisition, image selection and processing and in a common workflow.

"We developed the iX Suite for efficient collection and delivery of high-quality aerial image products," said Oodi Menaker, Phase One iX Suite Product Manager. "Every step of the workflow is planned and executed to ensure mapping projects are completed on time and on budget."

With the iX Suite, Phase One has taken a novel approach to managing aerial mapping projects by making quality control a key focus throughout the workflow to guarantee the generated image products meet end user specifications. A unique aspect of the iX Suite workflow is that imagery can be reviewed inflight and re-collected immediately if necessary, reducing the need for budget- and schedule-killing re-flights days or weeks later.

The iX Suite is comprised of three software tools that automate many functions to reduce workloads for pilots and operators in the air and streamline processing activities for technicians on the ground. These three software components are:

- iX Plan is a 3D photogrammetric flight planning application that takes end user requirements, terrain, and sensor properties into account to chart flightlines. The software includes a sensor database containing details of all Phase One PAS cameras and lidar sensors so that each image and point cloud acquisition is planned with exact area coverage, overlap, and resolution.

- iX Flight Pro is the flight and sensor management application that guides the pilot through the flight and triggers acquisition of sensor data. Images are displayed and overlaid on digital terrain model (DTM) in the graphical user interface so the onboard operator can view their quality and confirm precise coverage of the AOI.

- iX Process is an all-in-one mission review, quality assurance, and image export application. Using the mission report generated by iX Flight Pro, the processing tool overlays captured images on the flightline map and 3D DTMs, allowing the photogrammetric technician to check again for data quality and precise coverage of geographic areas. Accepted data sets are processed to generate and export images in commercial formats for delivery to end users.

"The iX Suite is tightly coupled with Phase One sensors, making our PAS aerial mapping systems easier, more intuitive, and cost-effective to operate," said Menaker. "Also, iX Suite interfaces with Riegl LiDAR systems, enabling customers to simultaneously operate a Phase One PAS camera and Riegl LiDAR with one management software in flight."

The Phase One PAS line of sensor systems was designed specifically to address the challenges of aerial image acquisition for 2D and 3D city modelling, photogrammetric mapping and surveying, agriculture, and other geospatial applications. The PAS product line includes the five-camera PAS 880 oblique and nadir system, PAS 280 large-format system, and PAS 150 systems.

Learn more at https://phaseone.ws/iX-suite.

CALENDAR

- 8 April, **ASPRS GeoByte—A History of the Landsat Program**. For more information, visit https://www.asprs.org/geobytes.html.

- 22 April, **ASPRS GeoByte— Using Geospatial Data to Evaluate Climate Hazards and Inform Environmental Justice**. For more information, visit https://www.asprs.org/geobytes.html.

- 27 May, **ASPRS GeoByte—Deep Fake Geography? A Humanistic GIS Reflection upon Geospatial Artificial Intelligence.** For more information, visit https://www.asprs.org/geobytes.html.

- 23 September, **ASPRS GeoByte— Allen Coral Atlas: A New Technology for Coral Reef Conservation.** For more information, visit https://www.asprs.org/geobytes.html.

- 3-6 October, **GIS-PRO 2022**, Boise, Idaho. For more information, visit https://www.urisa.org/gis-pro.

- 23-27 October, **Pecora 22**, Denver, Colorado. For more information, visit https://pecora22.org/.

223 Research on Machine Intelligent Perception of Urban Geographic Location Based on High Resolution Remote Sensing Images

Jun Chen, Cunjian Yang, and *Zhengyang Yu*

Machine intelligent perception (MIP) provides a novel way for human beings to recognize geographical locations automatically. MIP of geographical locations enables computers to describe locations automatically and quantitatively by extracting Earth's surface features and building relationships. Using the main cities in China as the experimental area, we have made a useful exploration in the field of MIP of geographical location, hoping to promote the development of human cognition of geographical location.

233 Identifying the Driving Factors of Urban Land Surface Temperature

Lifeng Liang, Benhua Tan, Sicheng Li, Zhiming Kang, Xiujuan Liu, and *Lihua Wang*

Land surface temperature (LST) has a profound impact on urban climate and ecology, and is widely used to quantify surface urban heat islands. The spatial heterogeneity of LST is affected by natural and human factors, with seasonal differences. This study selected Dongguan, a rapidly urbanizing city in China, as an example to analyze the relationship between the spatial heterogeneity of LST in different seasons and influencing factors in six dimensions.

243 Urban Land Cover/Use Mapping and Change Detection Analysis Using Multi-Temporal Landsat OLI with Lidar-DEM and Derived TPI

Clement E. Akumu and *Sam Dennis*

The mapping and change detection of land cover and land use are essential for urban management. The aim of this article was to map and monitor the spatial and temporal change in urban land cover and land use in Davidson County, Tennessee in the periods of 2013, 2016, and 2020.

255 Use of Commercial Satellite Imagery to Monitor Changing Arctic Polygonal Tundra

Amit Hasan, Mahendra Udawalpola, Anna Liljedahl, and *Chandi Witharana*

Commercial satellite sensors offer the luxury of mapping of individual permafrost features and their change over time. Deep learning convolutional neural nets (CNNs) demonstrate a remarkable success in automated image analysis. In this article, we systematically investigate the effectiveness of a spectrum of augmentation methods.

263 An Evaluation of Pan-Sharpening Methods for SuperView-1 Satellite Imagery

Lei Zhang, Bowen Wen, Ming Zhang, Qiongqiong Lan, and *Qian Wang*

At present, little research focuses on the application of pan-sharpening methods to SuperView-1 satellite imagery. There is a lack of suitability assessment for existing pan-sharpening methods applied to SuperView-1 images. This article proposes an evaluation method that integrates visual evaluation, spectral analysis of typical objects, and quantitative indicators to evaluate the advantages of different pan-sharpening methods in different scenes of SuperView-1 imagery.

271 Floating Solar Park Impacts Urban Land Surface Temperature Distribution Pattern

Bo Yingjie, Li Guoqing, Zeng Yelong, and *Liu Zhe*

In recent years, the global photovoltaic industry has developed rapidly. It is significant for evaluating the impact of large-scale solar parks on the environment for the sustainable development of the photovoltaic industry. At present, researchers have paid attention to changes in the local thermal environment caused by solar parks. As a new type of solar park, the influence of floating solar parks on urban land surface temperature distribution patterns is still unclear. In this article, we examine solar parks in Huainan City, China and adjacent areas.

COLUMNS

ANNOUNCEMENTS

DEPARTMENTS

facebook.com/ASPRS.org   linkedin.com/groups/2745128   twitter.com/ASPRSorg   youtube.com/user/ASPRS

COVER DESCRIPTION

The Pilbara in northwestern Australia exposes some of the oldest rocks on Earth, over 3.6 billion years old. The iron-rich rocks formed before the presence of atmospheric oxygen, and life itself. Found upon these rocks are 3.45 billion-year-old fossil stromatolites, colonies of microbial cyanobacteria. The image, acquired in October 2004, is a composite of ASTER bands 4-2-1 displayed in RGB.

With its 14 spectral bands from the visible to the thermal infrared wavelength region and its high spatial resolution of about 50 to 300 feet (15 to 90 meters), ASTER images Earth to map and monitor the changing surface of our planet and is one of five Earth-observing instruments launched Dec. 18, 1999, on the Terra satellite. The instrument was built by Japan's Ministry of Economy, Trade and Industry. A joint U.S./Japan science team is responsible for validation and calibration of the instrument and data products.

The broad spectral coverage and high spectral resolution of ASTER provides scientists in numerous disciplines with critical information for surface mapping and monitoring of dynamic conditions and temporal change. Example applications are monitoring glacial advances and retreats; monitoring potentially active volcanoes; identifying crop stress; determining cloud morphology and physical properties; wetlands evaluation; thermal pollution monitoring; coral reef degradation; surface temperature mapping of soils and geology; and measuring surface heat balance.

Image Credit: NASA/METI/AIST/Japan Space Systems, and U.S./Japan ASTER Science Team.

For more information on this image, visit https://www.nasa.gov/image-feature/36-billion-years-in-pastel-colors.

Be a part of ASPRS Social Media:

f facebook.com/ASPRS.org

in linkedin.com/groups/2745128/profile

twitter.com/ASPRSorg

You Tube youtube.com/user/ASPRS

GIS
Tips&Tricks

Savannah Carter & Al Karlin, Ph.D.
CMS-L, GISP

Need Help Finding GIS Tools – Here are a Few Tips

At some time, everyone comes to a point where they need help finding something that they know they have used before, but just cannot find. I frequently tell my students that "GOOGLE knows everything, so just ask GOOGLE!" GOOGLE is available 24/7 while I am available, hit or miss, so… What to do when GOOGLE cannot answer your question, or you know that you have used a GIS tool but just can't remember where to find it.

The solution is actually pretty simple, don't go to the "Help Menu"; use the Search functions. Here are some of Savannah's and my tips for (1) finding and (2) using the Search functions effectively.

FOR ARCGIS DESKTOP:

In ArcGIS Desktop there are multiple ways to open the Search functions. For those who prefer keyboard shortcuts, the <CTRL>-+F combination will open the search dialog box. For those who prefer mouse clicks, the Search dialog can be accessed from either the Geoprocessing tab (Figure 1) or the Windows tab (Figure 2) on the Main toolbar.
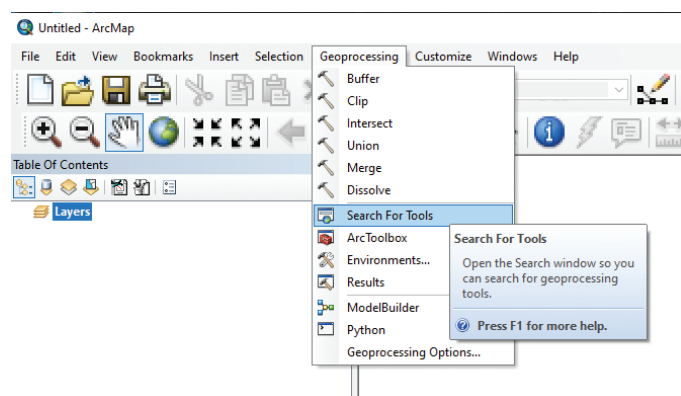
Figure 1. Accessing the Search functions from the Geoprocessing tab.
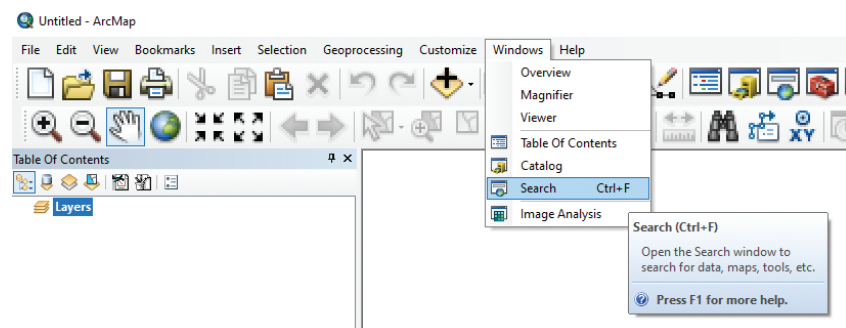
Figure 2. Accessing the Search functions from the Windows tab.

Once the Search dialog (Figure 3) opens, there are multiple tabs across the top to choose from for the search. Using the "All" tab will search for all objects in the ArcGIS environment containing the EXACT character string that you type.
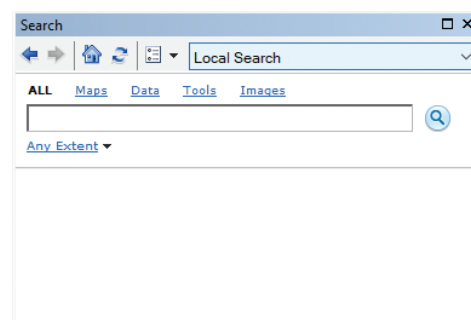
Figure 3. The Search dialog showing multiple tab filters acroass the top. The ALL filter tab is chosen in this example.

This can be extremely frustrating, particularly when you make a small typo (which we often do) as in the example in Figure 4, where a small typo, entering **raser** rather than **raster**, in the search yielded no results!
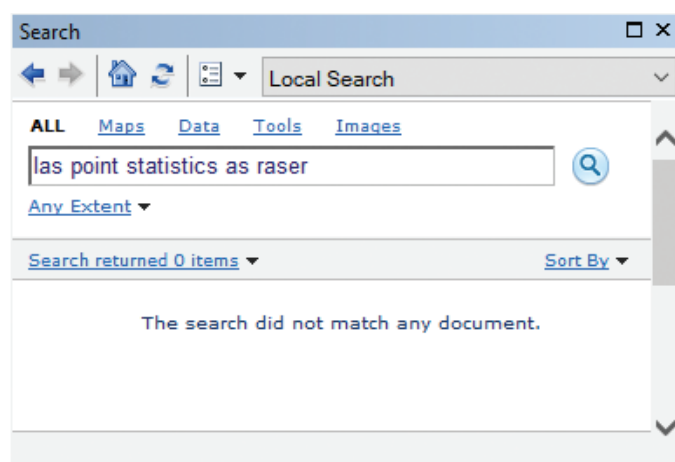
Figure 4. A small typo, raser instead of raster, in the search string failed to yield any results.

When the typo was corrected, the search yielded the location to the desired tool as in Figure 5.
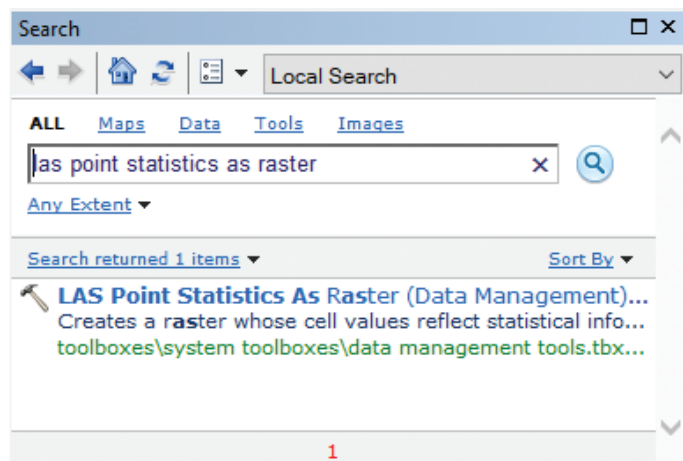
Figure 5. Correcting the typo, raster, not raser, in the search string yielded the desired tool.

TIP: An alternative is to search for tools using the Tool filter tab on the Search dialog. When using this tab, the search functions parses the search string as you type and offers suggestions to complete the string, as shown in Figure 6.
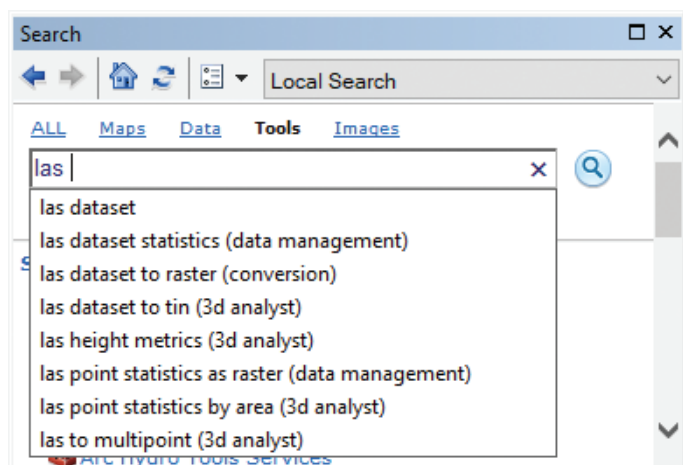
Figure 6. Using the Tools tab in the Search dialog box to search for tools.

FOR ARCGIS PRO

In ArcGIS Pro, the Geoprocessing tools are accessed through the "Analysis" Tab on the ribbon (Figure 7). Here, there are several "ready-to-use" tools and multiple ways to customize the tool groupings. But to search for a specific tool, clicking on the Tools icon will open the Geoprocessing dialog (Figure 8). Typing in the *Find Tools* box functions much like the ArcGIS Desktop search with the Tools filter and immediately starts to locate tools containing the character string and offers the options (Figure 9).
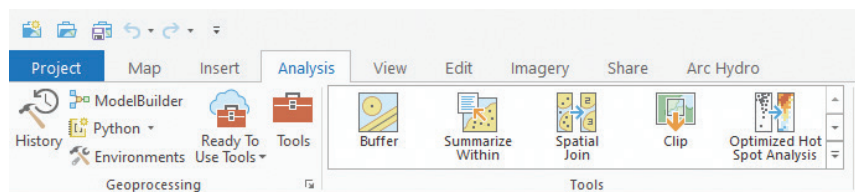
Figure 7. The "Tools" icon on the ArcGIS Pro Analysis Tab.
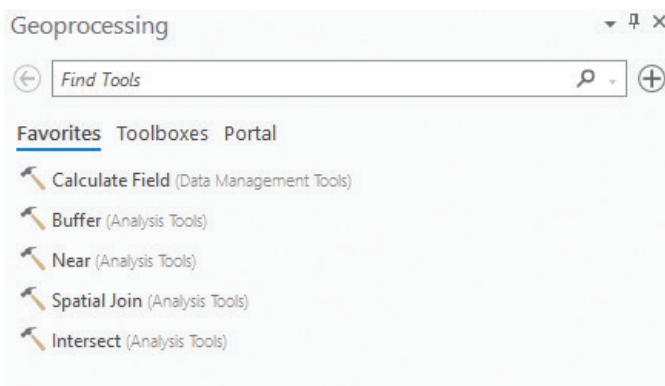
Figure 8. The Geoprocessing Dialog is used to Find Tools in ArcGIS Pro.
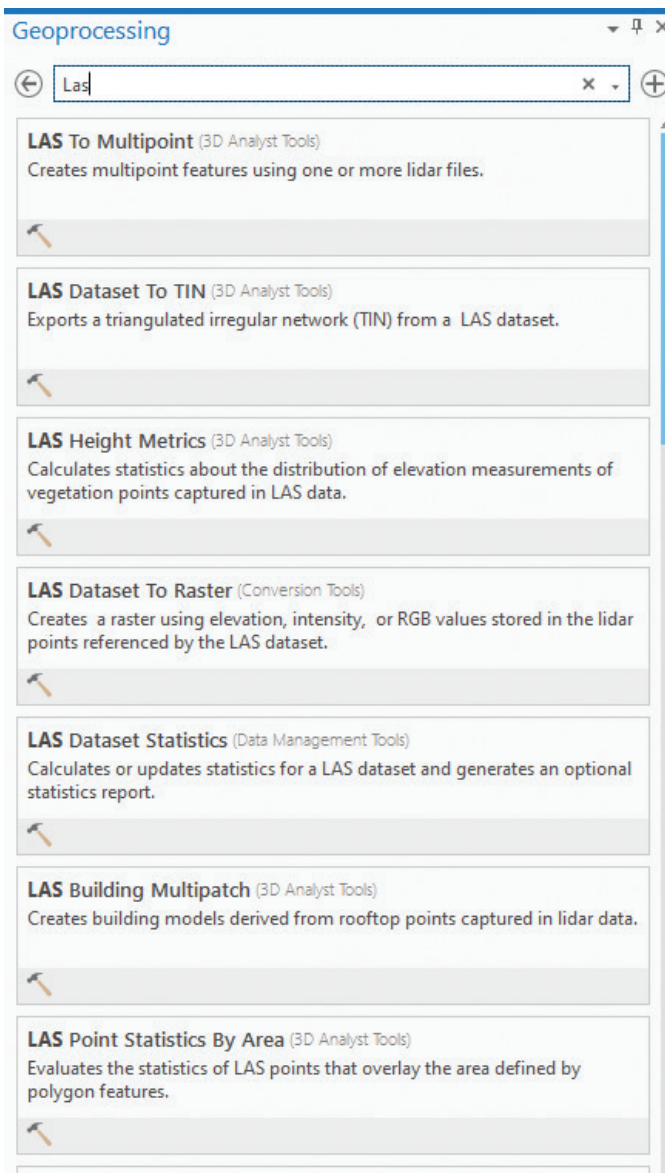
Figure 9. Typing in the Find Tools starts ArcGIS Pro to search for tools matching the character string while you type and offers list of tools to choose from.

In QGIS

In most versions of QGIS, the search for a processing tool is much the same as in ArcGIS Pro. The Processing Toolbox is opened from the Main Menu on the "Processing" tab as in Figure 10 or by the key combination <CTRL>+<ALT>+T.
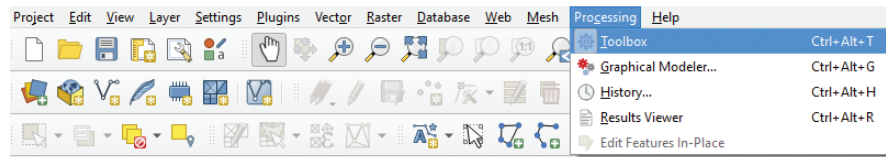
Figure10. QGIS Processing Tab opens the Toolbox.
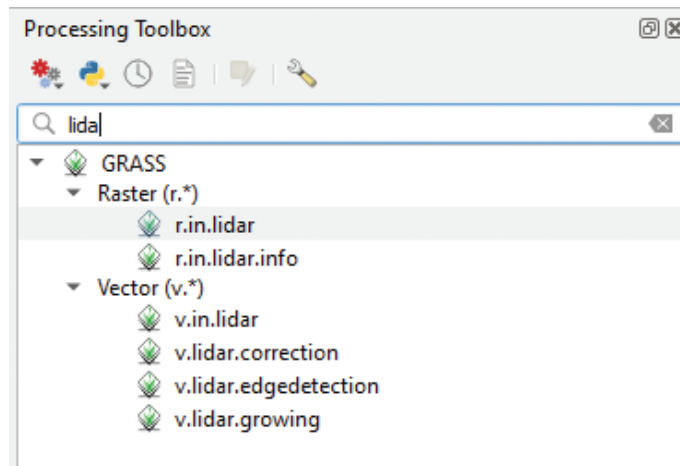
Figure 11. A search in QGIS for "lida" found 6 possible tools.

Once the Processing Toolbox is opened, the search area at the top of the toolbox will initiate searching as you type. In the example below (Figure 11), I started typing "lidar", got as far as "lida" and the search engine suggested two raster and four vector tools, much like the ArcGIS Pro tool above. Double-clicking on a tool will open its dialog box.

Not all GIS packages behave the way described above. In GlobalMapper the "Search" functions search for character strings in tables, names in files and/or geographic locations. So be aware of what your software does when you start searching.

Send your questions, comments, and tips to GISTT@ASPRS.org.

Savannah Carter is a Geospatial Analyst with Dewberry in the Tampa, FL office. She specializes in topographic and topobathymetric lidar data classification and interpretation Al Karlin, Ph.D., CMS-L, GISP is with Dewberry's Geospatial and Technology Services group in Tampa, FL. As a senior geospatial scientist, Al works with all aspects of Lidar, remote sensing, photogrammetry, and GIS-related projects.

GRIDS & DATUMS

BY Clifford J. Mugnier, CP, CMS, FASPRS

COMMONWEALTH OF THE BAHAMAS

The Grids & Datums column has completed an exploration of every country on the Earth. For those who did not get to enjoy this world tour the first time, *PE&RS* is reprinting prior articles from the column. This month's article on the Commonwealth of the Bahamas was originally printed in 2004 but contains updates to their coordinate system since then.

Inhabited by Lucayan Indians at the time of sighting by Christopher Columbus on 12 October 1492, the islands were assigned to Spain by Papal grant. Subsequently occupied only by slave traders and buccaneers, the Bahamas were granted by the British Crown to Sir Robert Heath in 1629. The Commonwealth of the Bahamas became independent from the United Kingdom (*PE&RS*, October 2003) on 10 July 1973. Comprised of a 700-island and islet archipelago with an additional 2,400 cays and rocks in the North Atlantic Ocean, the total land area is 10,070 km², and it is slightly smaller than the State of Connecticut. With a total coastline of 3,542 km, the terrain of the Bahamas is primarily long, low coral formations with some low rounded hills. The lowest point is the Atlantic Ocean (sea level) and the highest point is Mount Alvernia (63 m) on Cat Island. Twenty-two of the main islands are inhabited; 70% of the population of 316,000+ live on New Providence, and 16% live on Grand Bahama.

Prior to World War II, the only surveys performed in the Bahamas were astronomical observations (Astros) of hazards to navigation and local cadastral-type surveys for some privately held properties. Initial geodetic ties of the islands to the mainland coast of Florida were performed with flare triangulations in the 1960s that were soon followed by BC-4 ballistic camera observations of the PAGEOS satellites. Flare triangulations were performed by simultaneous theodolite observations to parachute flares dropped from airplanes flying at high altitudes in order to make geodetic connections over the horizon. BC-4 observations were performed by photogrammetric triangulations of passive

satellite reflections against a background of star fields. Dr. Helmut Schmid (one of the original V-2 rocket scientists) led that geodetic program for the U.S. Coast & Geodetic Survey. The BC-4 program was the intercontinental geodetic program that tied all of the continents into the first worldwide geodetic system. Dr. Schmid was the designer of the BC-4 ballistic camera and was the mentor to Dr. Duane C. Brown, a pioneer of modern analytical photogrammetry. The Bahamas have been referenced to the North American Datum of 1927 (Clarke 1866 ellipsoid) since the 1960s, where $a = 6,378,206.4$ m and $b = 6,356,583.8$ m. The datum origin point is Meades Ranch, Kansas (quite a distance away) at: $\Phi_O = 39^o\ 13'\ 26.686''$ N, $\Lambda_O = -98^o\ 32'\ 30.506''$ W., and the reference azimuth to station Waldo is $\alpha_O = 75^o\ 28'\ 09.64''$ (*PE&RS*, April 2000).

Thanks to John W. Hager, the following positions have been determined in the Bahamas by classical observation techniques. These following geodetic positions (φ, λ) are presumably on the NAD27 while the astro positions (Φ, Λ) are

independent: Elbow Cay Light (ECL), φ = 26° 32′ 21.715″ N, λ = −76° 57′ 10.870″ W. Also there is the Astro Observations (1940) where Φ = 26° 32′ 22.500″ N, Λ = −76° 57′ 15.353″ W, Astro Observations to light = 126.79 m, α = S 79° 01′ 27″ E true. Flamingo Cay Light (FLA), φ = 22° 52′ 43.48″ N, λ = −75° 51′ 38.28″ W. Great Inagua Island Light, φ = 20° 55′ 56.81″ N, λ = −73° 40′ 37.58″ W. Great Isaac Light (GIL), φ = 26° 01′ 48.30″ N, λ = −79° 05′ 22.08″ W. Great Ragged Island Light (GRL), φ = 22° 11′ 17.29″ N, λ = −75° 43′ 16.03″ W. Great Stirrup Cay (GSC), φ = 25° 49′ 36.41″ N, λ = −77° 53′ 50.20″ W. Gun Cay Light (GUN), φ = 25° 34′ 30.22″ N, λ = −79° 18′ 01.18″ W. Harvey Cay Light (HCL), φ = 24° 09′ 16.19″ N, λ = −76° 28′ 53.95″ W. Hog Island Light (HIL), φ = 25° 05′ 35.3″ N, λ = −77° 21′ 13.5″ W. Hogsty Reef Light (HRL), φ = 21° 41′ 27.71″ N, λ = −73° 50′ 56.81″ W. Hole-in-the-Wall Light (HIW), φ = 25° 51′ 32.522″ N, λ = −77° 10′ 37.938″ W. Observed astro (1940), Φ = 29° 51′ 22.320″ N, Λ = −77° 10′ 37.370″ W. Corrected in 1945, Φ = 29° 51′ 21.1155″ N, Λ = −77° 10′ 36.2901″ W. Little San Salvador Island (LIT), φ = 24° 33′ 53.73″ N, λ = −75° 56′ 08.00″ W. Man Island Light (MAN), φ = 25° 33′ 31.34″ N, λ = −76° 38′ 26.83″ W. Northwest Point Astro (NPA), Φ = 22° 27′ 24.42″ N, Λ = −73° 07′ 44.86″ W. Northwest Point Light (NPL), φ = 22° 27′ 35.56″ N, λ = −73° 07′ 47.43″ W. Pinder Point Light (PPL), φ = 26° 30′ 08.92″ N, λ = −78° 46′ 00.71″ W. Rum Cay Light (RUM), φ = 23° 38″ 36.1″ N., λ = −74° 50′ 05.7″ W. Santa Maria Light (SML), φ = 23° 40′ 54.54″ N., λ = −75° 20′ 27.60″ W. South Point Light (SPL), φ = 22° 50′ 56.48″ N., λ = 74° 51′ 14.42″ W. Stocking Island Astro (SIA), Φ = 23° 32′ 33.97″ N., Λ = −75° 46′ 10.75″ W. Sweetings Cay Light (SWC), φ = 26° 36′ 40.62″ N., λ = −77° 54′ 00.86″ W.

The NGA lists the three-parameter transformation from NAD27 to WGS84 for the Bahamas excluding San Salvador Island as ΔX = −4 m±5 m, ΔY = +154 m ±3 m, and ΔZ = +178 m ±5 m, where the 1987 solution is based on 11 station observations. For San Salvador Island, ΔX = +1 m ±25 m, ΔY = +140 m ±25 m, and ΔZ = +165 m ±25 m, and the 1987 solution is based on one station observation. In 1997, the U.S.

National Geodetic Survey observed a number of high-order positions in the Bahamas on the NAD83 datum. The only grid ever used in the Bahamas is the UTM.

The Commonwealth of the Bahamas Update

The U.S. Department of State issued a new paper on Limits in the Seas, No. 128 on the Bahamas Archipelagic and other Maritime Claims and Boundaries on 31 January 2014. "This study analyzes the maritime claims and maritime boundaries of the Commonwealth of The Bahamas, including its archipelagic baseline claim. The Bahamas' Archipelagic Waters and Maritime Jurisdiction (Archipelagic Baselines) Order, 2008 (Annex 1 to this study) took effect on December 8, 2008 and established the coordinates for the archipelagic baselines of The Bahamas.1 The archipelagic baselines are shown on Map 1 to this study. This Order was made in exercise of the powers conferred by section 3.2 of the Archipelagic Waters and Maritime Jurisdiction Act, 1993 (Act No. 37, Annex 2 to this study).2 The 1993 Act also established a 12- nautical mile (nm) territorial sea and 200-nm exclusive economic zone (EEZ). The Bahamas ratified the 1982 United Nations Convention on the Law of the Sea (LOS Convention) on July 29, 1983 and consented to be bound by the 1994 Agreement Relating to the Implementation of Part XI of the Convention on July 28, 1995.3." http://www.state.gov/e/oes/ocns/opa/c16065.htm.

The contents of this column reflect the views of the author, who is responsible for the facts and accuracy of the data presented herein. The contents do not necessarily reflect the official views or policies of the American Society for Photogrammetry and Remote Sensing and/or the Louisiana State University Center for GeoInformatics (C⁴G).

This column was previously published in *PE&RS*.
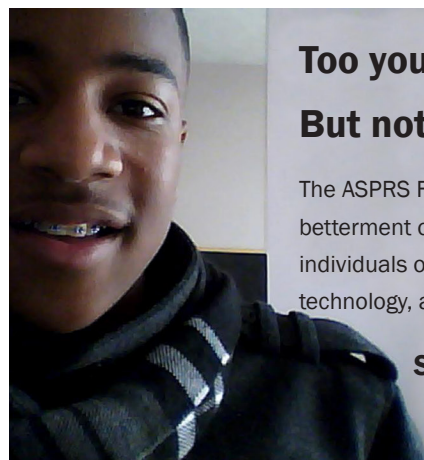
THE ASPRS STUDENT ADVISORY COUNCIL (SAC)

Resilient Research—Asking Students How the Pandemic has Impacted their Work, Strategies for Adaptation, and How SAC Can Help.

It has been a tough two years. The pandemic has dramatically changed many aspects of our lives, and the future remains uncertain. Though our individual experiences may differ, we at SAC feel that it is important that every person in our community (geospatial and beyond) knows that they are not alone. We feel that it is essential for all of us to pause and reflect on the emotional and physical toll of these past two years. This processing is not meant to simply be a rehashing of difficult times but is instead intended to help us respect where we have been, so we can understand how to continue on to a path of healing and growth.

For this special edition of SAC Signatures, the SAC team reached out to students asking them about their experiences conducting research during the COVID-19 pandemic and requested that they share any advice for other students experiencing similar issues. Finally, we asked them to share how SAC has helped or can continue to help them meet their goals and provide continued support. The responses we received touched on all spheres of student life (work, home, and social aspects), helping us to better understand that vast ripple effects caused by the pandemic, and how these effects interact and interfere with research and study.

Student Responses

1. **How did the COVID-19 pandemic affect the progress of your research?** *Answers are summarized by category.*

   - **Data Collection & Analysis**
     Unsurprisingly, a big impact of the pandemic was inability to conduct field work and collect data or in-person interviews. Furthermore, students noted that fulfilling deadlines was more difficult as they struggled to meet with peers and advisors. Communication, though possible through zoom, was lacking for some students compared to meeting in person.

   - **Technology & Education**
     During the pandemic, access to school technology has been limited, forcing students to use their own internet and computers. This has proved difficult for some with limited WIFI or computers that are not as powerful as those at school. As classes became fully remote, some students felt lapsing engagement with class content.

   - **Social Life & Wellbeing**
     Students reflected on how seeing the global and local impacts of COVID-19 (or even catching it themselves) has been a big source of stress and anxiety. Further, students reflected on how the pandemic has

Pandemic Research Impacts.

inequitably impacted caregivers who must juggle work and family life as well as the experiences of those who are, or are caring for, immunocompromised individuals. As social gatherings became impossible and public places closed, students felt isolated. Though these in-person gatherings were often replaced with virtual ones, students experienced a new issue: "zoom burn out", where endless virtual meetings became somewhat draining. Additionally, students discussed the physical impacts of working from home, including pains and stiffness from sitting at a desk all day

ASPRS STUDENT ADVISORY COUNCIL

LAUREN MCKINNEY-WISE
COUNCIL CHAIR

OSCAR DURAN
DEPUTY COUNCIL CHAIR

CHUKWUMA JOHN OKOLIE
COMMUNICATIONS COUNCIL MEMBER

TBD
EDUCATION & PROFESSIONAL NETWORKING CHAIR

ALI ALRUZUQ
DEPUTY EDUCATION & PROFESSIONAL NETWORKING CHAIR

TESINI PRECIOUS DOMBO
COMMUNICATIONS COUNCIL MEMBER

RABIA MUNSAF KHAN
COMMUNICATIONS COUNCIL CHAIR

KENNETH EKPETERE
CHAPTERS COMMITTEE CHAIR

FREDA ELIKEM DORBU
COMMUNICATIONS COUNCIL MEMBER

2. **What strategies did you use to adapt to the impacts of the pandemic? What advice do you have for students conducting research during the pandemic?** *Answers are summarized by category.*

- **Data Collection & Analysis**
  Students suggest using professional social networks, such as LinkedIn, ResearchGate, and others to expand their professional networks and learn about exciting new skills and data resources.

- **Technology & Education**
  For collaborative projects and assignments, students recommend using resources like Google Docs, as these make it easier to work together and track progress. Students also stress the importance of time management to stay productive while working remotely.

- **Social Life & Wellbeing**
  To ease isolation, students suggest using "snail mail" to correspond with friends and family and to, when safe to do so, hold small gatherings for social or

Pandemic Adaption Strategies.

study time. To help with mental and physical health, scheduling and regularly taking walks was suggested (as well as investment into a cheap standing desk). Another bit of advice for our bespectacled community members was to tape your mask across your nose to prevent your glasses steaming up. Finally, students remind us to keep going and remember that "everything will be fine".

3. **How did engagement in SAC and ASPRS assist you in achieving your professional and academic goals during the pandemic? What else can SAC do to support you?**
Students shared their gratitude for the professional, academic, and social connections SAC strives to provide to students. Furthermore, students are grateful for the opportunities shared and implemented by ASPRS, such as scholarships, events, and space to present their work. Students also expressed appreciation for the connection and resources provided by their local ASPRS student chapters. SAC will work hard to continue to share resources for students and make space for collaboration and networking. **Thank you to all the students who participated in our survey!**

If you are interested in participating in SAC activities

- Join us every other Thursday from 10-11 am PST!
- Join us via this zoom link, https://tinyurl.com/SACASPRSMeeting

How SAC and ASPRS have helped.

ASPRS STUDENT ADVISORY COUNCIL

LAUREN MCKINNEY-WISE
COUNCIL CHAIR

OSCAR DURAN
DEPUTY COUNCIL CHAIR

CHUKWUMA JOHN OKOLIE
COMMUNICATIONS COUNCIL MEMBER

TBD
EDUCATION & PROFESSIONAL NETWORKING CHAIR

ALI ALRUZUQ
DEPUTY EDUCATION & PROFESSIONAL NETWORKING CHAIR

TESINI PRECIOUS DOMBO
COMMUNICATIONS COUNCIL MEMBER

RABIA MUNSAF KHAN
COMMUNICATIONS COUNCIL CHAIR

KENNETH EKPETERE
CHAPTERS COMMITTEE CHAIR

FREDA ELIKEM DORBU
COMMUNICATIONS COUNCIL MEMBER

Call for *PE&RS* Special Issue Submissions

Multimodal Remote Sensing Data Processing and Analysis for Earth Observation

Earth observation, by providing critical information on natural resources, hazardous areas, and climate change, among others, is a powerful tool in all aspects of life. The observations come primarily from space-based sensors such as satellites, but they highly depend on ground-based remote sensing devices. Multimodal remote sensing systems integrate optical and passive microwave radiometers to improve the quality of observations. The versatility of multimodal RS offers enormous potential to monitor diverse target phenomena in all climate system components with high spatial, temporal, or spectral resolution. It provides innovative methods for processing multispectral, hyperspectral, and polarimetric remote sensing data for different vegetation, geophysical, and atmospheric applications to understand the earth better. However, there are still challenges to achieving maximum exploitation of multimodal data. At the same time, the combination of multimodal remote sensing technologies is a powerful approach that can yield significant advantages compared to traditional single-modal sensors.

The techniques such as image processing is typically used to adjust and refine data derived from remote sensing. Its capabilities are also useful for merging data sources. Image processing techniques, such as filtering and feature extraction, are well suited for dealing with the high-dimensionality of spatially distributed systems. The input data may come from different sensors, each with a different spatial resolution and measurement scale ('multimodal'). It provides approaches for the extraction of relevant non-topographic information from remote sensing data, such as demographic indicators from satellite images of urban areas, which could assist in future spatial modelling of these areas. It helps to analyze shape, topography, and texture phenomena for soil and vegetation data and various methods for image fusion and analysis of the optical, radar, and gravity data. It covers a wide range of geospatial applications, including land and water resources management, urban planning, environmental monitoring, natural hazards and climate change, oceanography, engineering design, and national security and intelligence. It processes multispectral, thematic-mapping, thermal-infrared (TIR), hyperspectral data acquired from optical, SAR or lidar platforms with advanced techniques in the areas of scene characterization and feature extraction.

This special issue is intended for remote sensing scientists, engineers, and researchers involved in its application for earth observation. Innovative techniques dealing with climate monitoring; environmental monitoring, including pollution monitoring and deforestation detection; geographical information system (GIS) applications; maps generation, land cover classification and change detection; mineral exploration industries; hydrology and water resources management; based on multimodal remote sensing data are most invited for submission.

List of Topics (include, but not limited to the following):
- Deep learning and computer vision for earth observation and multimodal remote sensing
- Semantic and instance segmentation of the multimodal remote sensing data for earth observation and analysis
- Multimodal remote sensing data fusion, interpretation and analysis for earth observation
- Hyperspectral remote sensing and image processing for earth observation
- Light weight deep neural network algorithms for earth surveillance
- Earth object classification and recognition using multimodal remote sensing approaches
- Multi-resolution and multi-modal remote sensing for enhancing the earth observation processes
- Novel applications of multi-modal remote sensing in earth monitoring and surveillance processes
- Spatio-temporal data analysis for efficient earth observation
- Multimodal data reconstruction and restoration for efficient classification process
- Benchmarking multimodal datasets for earth observation
- New algorithms and frameworks for efficient analysis of multi-modal remote sensing data

Deadline for Manuscript Submission
August 1, 2022

Submit your Manuscript to
http://asprs-pers.edmgr.com

Guest Editors

Dr. Ahmed A. Abd El-Latif, alatif@science.menofia.edu.eg, Associate Professor, *Department of Mathematics and Computer Science, Faculty of Science, Menoufia University*, Egypt.

Dr. Edmond Shu-lim Ho, e.ho@northumbria.ac.uk, Senior Lecturer, *Department of Computer and Information Sciences, Northumbria University, Newcastle upon Tyne*, United Kingdom.

Dr. Jialiang Peng, jialiangpeng@hlju.edu.cn, Associate Professor, *School of Data Science and Technology, Heilongjiang University*, China.

ASPRSNEWS

ASPRS ANNOUNCES UPCOMING GEOBYTES!

A History of the Landsat Program
Presented by Ellie Leydsman McGinty, *AmericaView*
April 8th

Using Geospatial Data to Evaluate Climate Hazards and Inform Environmental Justice
Presented by Carolynne Hultquist and Cascade Tuholske, *Center for International Earth Science Information Network*
April 22nd

Deep Fake Geography? A Humanistic GIS Reflection upon Geospatial Artificial Intelligence
Presented by Dr. Bo Zhao, *University of Washington, Seattle*
May 27th

Allen Coral Atlas: A New Technology for Coral Reef Conservation
Presented by Brianna Bambic, N*ational Geographic Society and Arizona State University*
September 23rd

For complete details and to register, visit https://www.asprs.org/geobytes.html.

NEW ASPRS MEMBERS

ASPRS would like to welcome the following new members!

FOR MORE INFORMATION ON ASPRS MEMBERSHIP, VISIT
HTTP://WWW.ASPRS.ORG/JOIN-NOW

Modelling, Representation, and Visualization of the Remote Sensing Data for Forestry Management

Remote sensing data includes aerial photography, videography data, multispectral scanner (MSS), Radar, and laser to map and understand various forest cover types and features. An accurate digital model of a selected forest type is developed using forest inventory data in educational and experimental forestry and extensive databases. It includes the formalization and compilation of methods for integrating forest inventory databases and remote sensing data with three-dimensional models for a dynamic display of forest changes.

Big data technology employs vast amounts of forestry data for forestry applications that require real-time inquiry and calculation. The techniques and strategies of forestry data analysis are integrated into the big data forestry framework, enabling interfaces that other Programmes may call. Virtual Reality addresses constraints in forest management such as temporal dependence, irreversibility of decisions, spatial-quantitative change of characteristics, and numerous objectives. Virtual representations integrate various computer graphics systems with display and interface devices to create a spatial presence in an interactive 3 D environment. Visualization of plant species' growth patterns, changes in species and their composition, and other morphological properties of forests are enhanced using machine learning and regression analysis methods as part of a digital model. In modelling, deep learning (DL) replicates expert observations on hundreds or thousands of hectares of trees.

Remote sensing is being used to map the distribution of forest resources, global changes in flora with the seasonal variations, and the 3D structure of forests. Graphic Information System (GIS) based visualizations depict dynamics through animations and 3D geo model visualizations and allow advanced spatial analytics and modelling in geographical phenomena for forest management. Digital forest modelling includes integrating forest inventory data, forest inventory database formation, graphics objects of forest inventory allocations with a digital forest model, and technology for visualizing forest inventory data. It helps forecast changes and visualizes situational phenomena occurring in forests using data and models involving spatial-temporal linkages.

Standard aerial shots capture images that view unseen components to the naked eye, such as the Earth's surface's physical structure and chemical composition. The challenges in remote sensing models include insufficient Remote Sensing (RS), spatial, spectral, and temporal resolution to detect degradation accurately. High costs of RS, the gap between operational and scientific uses, and lack of information sharing are some of the challenges of RS for forest management. The list of topics of interest include but are not limited to the following:

- Advancement of forest surveillance through Geographical Information Systems
- State of the art and perspectives of modelling and visualization framework for Forest type mapping and assessment of distribution
- Futuristic Satellite data analysis for stock maps and forest inventory analysis
- Big data-enabled GIS framework for forest management information
- AI-based Space Remote Sensing For Forest Ecosystem Assessment
- Enhanced visualization through deep learning for forest management solutions
- Novel approaches of multi-temporal satellite data using digital image analysis for forest management
- Advance representation of discrete objects and continuous fields in virtual environments through VR framework
- Database framework for regional and plot-based forest allotment data for model representation and visualization
- Development of scalable models for area-based metrics from Light Detection and Ranging (lidar) devices and photographic structure-for-motion (SFM)

Deadline for Manuscript Submission—June 7, 2022

Submit your Manuscript to http://asprs-pers.edmgr.com

Guest Editors

Dr. Gai-Ge Wang, gai-gewang@outlook.com and wgg@ouc.edu.cn, *Department of Computer Science and Technology, Ocean University of China*, China

Dr. Xiao-Zhi Gao, xiao.z.gao@gmail.com and xiao-zhi.gao@uef.fi, *Machine Vision and Pattern Recognition Laboratory, School of Engineering Science, Lappeenranta University of Technology*, Finland.

Dr. Yan Pei, peiyan@u-aizu.ac.jp, *Computer Science Division, The University of Aizu*, Japan.

Research on Machine Intelligent Perception of Urban Geographic Location Based on High Resolution Remote Sensing Images

Jun Chen, Cunjian Yang, and Zhengyang Yu

Abstract

Machine intelligent perception (MIP) provides a novel way for human beings to recognize geographical locations automatically. MIP of geographical locations enables computers to describe locations automatically and quantitatively by extracting Earth's surface features and building relationships. The earth surface fingerprint is established here by mining the relationship between spatial objects with stable characteristics extracted from urban high-resolution remote sensing images, which realizes intelligent perception of geographical location innovatively. Mask Region-based Convolutional Neural Network is used to automatically extract the spatial objects such as playgrounds, crossroads, and bridges from the images. Then, the extracted spatial objects are encoded according to the landuse type, distance, and angle of 24 nearest objects to construct urban surface fingerprint database. The urban surface fingerprint database is used to match the geographical location of spatial objects in local images so that the matching algorithm can be used for machine recognition of the geographical location of specific objects in the target image. Taking the main cities in China as the experimental area, the success rate of location perception is 92%. We have made a useful exploration in the field of MIP of geographical location, hoping to promote the development of human cognition of geographical location.

Introduction

Human cognition of geographical location has gone through four stages. Before words appeared, people expressed geographical location by tying knots on ropes. After the invention of words, people began to record geographical location with words. Later, people learned to represent locations by drawing maps, and the appearance of maps is a great leap in human cognition of geographical location. With the advent of computers, geographical location is digitized, so the calculation and service based on geographical location can be provided by computers. Today, cutting-edge technologies such as high-performance computing and artificial intelligence constantly stimulate and give birth to new demands and new applications. The machine intelligent perception (MIP) of geographical locations is a new stage of human cognition of geographical locations and is an important frontier topic in geographic information science.

The key MIP of a geographical location is to establish a set of methods so that computers can describe the location automatically and quantitatively. At present, it mainly involves two areas of research: one is based on the image features, and the other is to establish the concept of geo-science mapping to understand geographic location. The former determines the features contained in the image through various transformations, and then realizes geographic location perception by using the feature matching algorithm (Jiang *et al.* 2021). The classical methods for automatically extracting features include Harris feature (Kovacs and Sziranyi 2013; Vishwakarma and Bhuyan 2020; Wang *et al.* 2008), scale-invariant feature transform (SIFT) feature (Yang *et al.* 2019; Yao *et al.* 2009; Zhou 2009) and speeded up robust features (SURF) feature (Bay *et al.* 2006; Su *et al.* 2010; Tong *et al.* 2021). With the improvement of algorithms, the accuracy and efficiency of feature extraction are getting higher and higher. For example, Rublee *et al.* proposed an improved ORB model, which is rotation invariant and resistant to noise (Rublee *et al.* 2011). Wu adopted a feature detection method based on image grayscale information-FAST operator to improve the speed of extracting image feature points (Wu 2019). However, due to the limitation of algorithms, a large number of feature points are often extracted from an image. So, it requires a complex algorithm to extract useful information that can distinguish specific geographical locations from a large number of feature points. Fan and Zhao proposed a matching process to cluster features from a group of reference images in order to enhance matching robustness (Fan and Zhao 2012). Liu *et al.* proposed a simple and robust feature point matching algorithm, called Restricted Spatial Order Constraints (RSOC), to remove outliers for registering aerial images with monotonous backgrounds, similar patterns, low overlapping areas, and large affine transformation (Liu *et al.* 2012). Chen *et al.* proposed a line-based matching method to overcome the low significant level of point feature and the shortage in the matching between weak texture images (Chen *et al.* 2013). Although some progress has been made in feature screening and matching optimization, for machine intelligent sensing location, it is necessary to analyze a wide range of remote sensing images and extract a small number of evenly distributed features to quickly indicate the location of any place in the region. The existing research rarely involves this field. Due to the complexity of algorithm and data organization, it is difficult to directly migrate to the field of MIP of geographical location.

Geo-science mapping is another prospective study in this field. Based on the theory of geo-science mapping, Luo proposed the spatial cognition theory coupled with remote sensing mapping and constructed a theoretical and methodological system in the way of "pixel-object-object-pattern" (Matsuoka and Midorikawa 1993). Based on the theory of geo-science mapping and geographic information systems (GIS) technology, Lu analyzed the land use "pattern map", "classification map", "transfer map", "change pattern map", and "fluctuation map" of land border areas of Guangxi Province from 2003 to 2013, and thus revealed the spatial-temporal evolution process of land use (Rucheng *et al.* 2009). Abrams (2017) constructed the geo-science mapping of the land surface. Hewson's project demonstrated, within the study areas of Wagga and Cobar, the usefulness of the National ASTER Geoscience Map products for identifying variations in the composition of surface materials (Hewson and Robson 2014). Moosavi proposed a generic

Jun Chen and Zhengyang Yu are with Chengdu University of Information Technology, Chengdu, China (494834920@qq.com).

Cunjian Yang is with 1. Key Laboratory of Land Resources Evaluation and Monitoring in Southwest, Ministry of Education, Sichuan Normal University; 2. Research Center of Remote Sensing and Geographic Information System Application,The College of Geography and Resource Sciences,Sichuan Normal University.

methodology for combining high-dimensional spatial data to identify and visualize the hidden spatial patterns in a single-layer geo-map (Moosavi 2017). At present, the study of geo-science mapping is still in its infancy, and different scholars describe geographical features in a different way, so it is difficult to establish a unified index to automatically construct regional geo-science mapping.

The realization of MIP of geographical location needs to be completed automatically by the computer. Given the current research results, there is still a long way to go. This paper, with cities as the research area, tries to introduce the concept of surface fingerprint, discusses how to make computers automatically extract objects from remote sensing images, and establishes surface fingerprints. By doing so, it realizes the preliminary MIP of geographical location.

The Concept of Machine Perception of Geographical Location

Surface Fingerprint

Fingerprint, also called handprint, is characterized by raised lines on the epidermis. Human fingerprint is the product of a combination of environmental and genetic factors. Everyone has unique fingerprints. Fingerprint lines are not smooth or continuous, and the interruptions, bifurcations, or turns, as feature points, are the basis of fingerprint identification.

The concept of surface fingerprint is proposed by generalizing the concept of human fingerprint to geographical space to identify the location of spatial objects. Surface fingerprint is the unique identification of a specific location on the earth. Similar to human fingerprint, it can be constructed with spatial feature points. If too many feature points are extracted from the image, the complexity of matching computation will greatly increase. In this paper, the spatial objects are used as the feature points and surface fingerprint can be constructed through the spatial relationship of these objects.

MIP of Geographical Location

"Machine intelligent perception of geographical location", also known as "machines automatically understanding the geographical location", means that the computer automatically obtains the feature points of the surface, constructs the surface fingerprint through a certain algorithm, and uses the surface fingerprint matching algorithm to automatically indicate the surface location. Obviously, the MIP of location is based on the concept of surface fingerprint. By constructing a large-scale surface fingerprint database, the machine can store the unique location identification at any location in the research area, so as to achieve the purpose of automatic and intelligent perception of location.

The Method of MIP of Urban Geographic Location

Automatic Extraction of Spatial Objects Based on Mask Region-Based Convolutional Neural Network (R-CNN)

Obviously, instance segmentation is the basis of machine perception of geographic location, which can effectively detect objects with relatively stable spatial morphological and spectral features. On high-resolution remote sensing images, playgrounds, crossroads, and bridges have stable spectral characteristics and morphology.

It is necessary to establish a training data set and test data set of instance segmentation model. For each picture in the data set, the position and shape of each object need to be marked in advance. For a playground, we directly mark the area enclosed by the runway edge. For a crossroad, we mark the area enclosed by the zebra crossing, and for a bridge, we mark the edge of the bridge area. Then it automatically calculates the bounding rectangle. Typical sample marks are shown in Figure 1. The yellow line in the figure is the outer boundary of the object of interest in the image.

There are 1200 images and 1330 labeled objects in the training sample data set, and 500 images and 589 labeled objects in the test data set. We selected three instance segmentation models, including TensorMask (Chen *et al.* 2019), CenterMask (Youngwan and Park 2020), and Mask Region-Based Convolutional Neural Network (R-CNN) to train the data sets, respectively. Stochastic gradient descent (SGD) is used to train these models. The test data set was used to extract and vectorize the spatial objects on each image, and the performance indexes of frames per second (FPS), mAP50, and mAP75 were counted, as shown in Table 1. It can be seen that Mask R-CNN has the best prediction accuracy in the three models. Therefore, we choose Mask R-CNN as the extraction model of spatial objects.

Table 1. Comparison of three models on test data set.

Model	Resolution	Backbone	FPS	mAP$_{50}$ (%)	mAP$_{75}$ (%)
TensorMask	512 × 512	ResNet-50-FPN	2.74	83.4	72.6
CenterMask	512 × 512	DLA_34	13.48	76.3	70.2
Mask R-CNN	512 × 512	ResNet-50-FPN	7.70	84.1	75.7

FPS = frames per second; R-CNN = Region-Based Convolutional Neural Network.

In order to improve the precision of the model and try to avoid the false detection, the category credibility thresholds of playground, crossroad, and bridge are set to 0.98, 0.98, and 0.97, respectively, with the higher overall precision and relatively high recall rate. The mask threshold is set to 0.5, the mask of spatial object extracted by Mask R-CNN is closest to the result of manual discrimination. Table 2 shows the training accuracy of test data set. The overall recall rate is 83.7% and the precision is 95.9%. Compared with the artificially marked mask, the average precision is 80.1%.

Figure 2 shows the extraction results of typical sample region. It can be seen from the figure that the extraction results of Mask R-CNN model are close to human interpretation, which meets the requirements of urban spatial object extraction.

However, although the model has relative high detection precision, under the influence of image blur, occlusion, and shadow, there are still some unrecognized objects. Figure 3 gives some undetected samples. Therefore, when the machine perceives the location, the error of automatic object extraction cannot be ignored, and its surface fingerprint construction and matching method must be fault-tolerant.

(a) (b) (c)

Figure 1. The typical spatial objects on high-resolution remote sensing images.

Table 2. The training accuracy of test data set with Mask R-CNN.

Object Type	Category Code	Number of Training Samples	Number of Test Samples	Category Credibility Threshold	Category Precision (%) Recall Rate	Category Precision (%) Precision	Mask Precision (%)
Playground	1	437	198	0.98	84.8	96.6	83.5
Crossroad	2	450	206	0.98	83.0	96.1	75.3
Bridge	3	443	185	0.97	83.2	95.1	81.5
Total	—	1330	589	—	83.7	95.9	80.1

R-CNN = Region-Based Convolutional Neural Network.

(a)   **(b)**
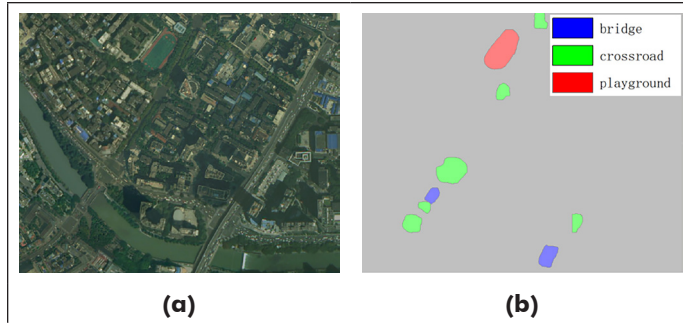
Figure 2. Typical result of object extraction from high-resolution remote sensing image.

(a)

(b)

(c)
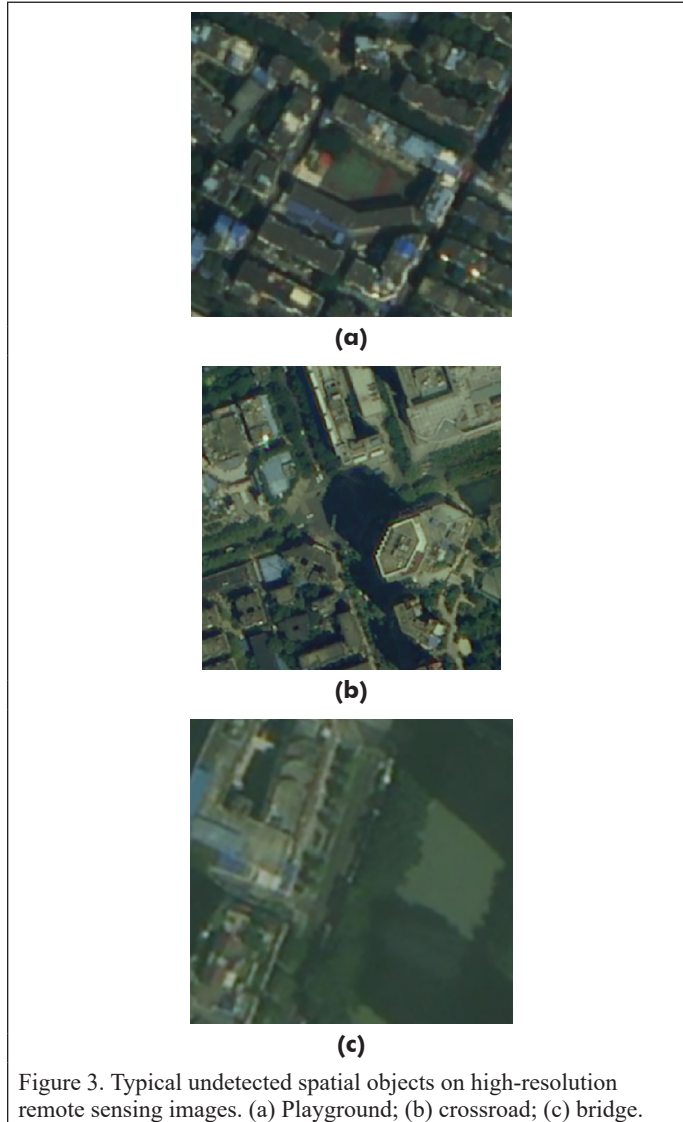
Figure 3. Typical undetected spatial objects on high-resolution remote sensing images. (a) Playground; (b) crossroad; (c) bridge.

Spatial Object Coding and Automatic Construction of Urban Surface Fingerprint Database

Features of Spacial Object

Spatial object features include attribute features, location features, morphological features, and spatial relationship features, which are the keys of spatial object coding.

(1) Attribute features:
Mask R-CNN can extract not only the distribution range of the spatial objects, but also their category with high precision. Therefore, the category of the spatial objects is used as the attribute code.

(2) Location features:
The center position of a spatial object is used to measure its position. There are: the center of minimum bounding rectangle (the center of MBR), the geometrical center, the center of gravity, and so on. Transform the mask of each spatial object extracted by Mask R-CNN into vector polygon and then calculate the center position of the spatial object by its edge nodes.

(3) Morphological features:
There are many indexes to measure the spatial morphological features. Among the edge nodes of one spatial object, the connection between the farthest two nodes is called the major axis, and the length is expressed as d, as shown in Figure 4. The maximum distance from the node to the major axis is called the semi-minor axis, which is expressed as s. The oblateness of the spatial objects e is:

$$e = \frac{0.5d - s}{0.5d}. \tag{1}$$
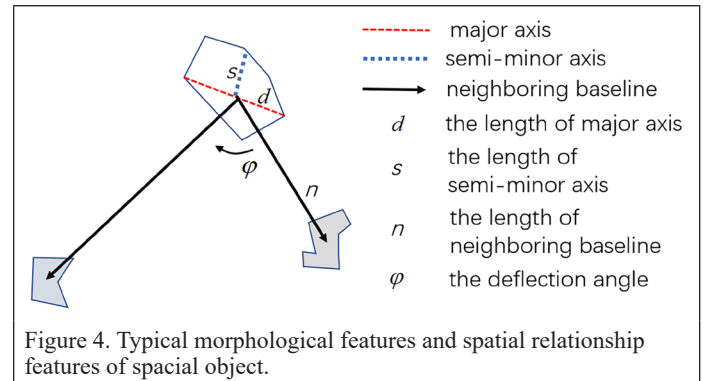
Figure 4. Typical morphological features and spatial relationship features of spacial object.

(4) Spatial relationship features:
The spatial relationship of spatial objects refers to the geometric relationship between each object and its neighboring objects, including the distance, orientation, and topology. Because the topological relationship is difficult to describe quantitatively, the relative distance and orientation between spatial objects are measured based on the neighboring baseline. Starting from the center of one spatial object, the ray connecting the center of its neighboring spatial object is called the neighboring baseline, and its rotation angle to the X axis is called the neighboring angle. The length of the line segment is called the neighboring distance, which is expressed as n. Figure 4 shows a schematic of the neighboring baseline and distance.

We take one of the neighboring objects as reference in order to measure other neighboring objects relatively. The angle difference between the neighboring baselines is called the deflection angle φ. The ratio of

their neighboring distances is called the neighboring distance coefficient ζ. Clearly, φ and ζ are all scale independent and rotation invariant.

Feature Selection for Spatial Object Coding
In order to ensure the availability and stability of surface fingerprint, it is necessary to select relatively stable spatial features that can be automatically extracted by computers for spatial object coding. In addition, the codes constructed by spatial features should be rotation invariant and scale independent so as to realize machine perception of geographical location.

(1) Data set preparation for feature selection:
In order to investigate the stability of different features, the city of Chengdu was chosen as the study area, and the playgrounds, crossroads, and bridges were extracted from the 18-level data of Google online satellite image and Tianditu online satellite image, respectively, to form their own object data set. There are 4329 objects and 4924 objects extracted from Google and Tianditu, respectively. We overlapped the two object data sets and marked the same two objects as an object pair with the same identifier. The number of object pairs is 2842, accounting for only 65.7% and 57.7% of their total number of objects, respectively.

(2) The best location measurement method of spatial object:
To select the best location measurement method, the object pairs with the following characteristics are selected, i.e., their nearest neighbor objects also belong to another object pair. These object pairs are used to calculate the neighboring distance and angle with different location measurement method. Table 3 shows the absolute errors of the two data sets. It can be seen from the table that with the location measurement method based on center of gravity, the average error of neighboring distance and neighboring angle is less than that of the other two methods. Therefore, the center of gravity is used to measure the location for each object.

Table 3. Neighboring distance and angle error of different location measurement methods.

Measurement Method	Neighboring Distance (m)		Neighboring Angle (°)	
	Average Error	Maximum Error	Average Error	Maximum Error
Center of MBR	4.53	39.5	1.2	22.6
Geometrical center	8.29	81.9	1.95	25.1
Center of gravity	4.06	39.8	1.14	22.4

MBR = minimum bounding rectangle.

(3) Comparison of stability between morphological characteristic parameters and spatial relationship characteristic parameters:
The major axis length, semi-minor axis length, and oblateness of each object pair are calculated, and then the parameter errors are compared with the nearest neighboring distance. Because the parameters have different units, the relative error s is used for the analysis:

$$\sigma = \frac{|\mu_1 - \mu_2|}{\mu_1}, \qquad (2)$$

where μ_1 and μ_2 are the parameter value of the spatial objects extracted from Google and Tianditu, respectively.

The relative errors of morphological characteristic parameters are shown in Table 4. It can be seen that the relative errors of the major axis length, semi-minor axis length, and oblateness of the objects extracted from different remote sensing images are all larger than those of the nearest neighboring distance. It means that the spatial objects extracted by Mask R-CNN have lower stability of morphological features

compared with the neighboring relationship. Spatial object coding should mainly consider the adjacency of the objects.

Table 4. Relative error of morphological characteristic parameters.

Oblateness		Semi-Minor Axis Length		Major Axis Length		Nearest Neighboring Distance	
Average Value	Peak Value	Average Value	Peak Value	Average Value	Peak Value	Average Value	Peak Value
3.186	8352	0.16	10	0.11	6.01	0.0032	0.72

Spatial Object Coding
Spatial object coding includes three parts: location coding, attribute coding, and spatial relationship coding.
(1) Location coding and attribute coding:
The coordinate of the gravity of the center of each object is regarded as its location code. Attribute coding uses landuse type code to represent the attributes of spatial objects. Table 2 gives the category codes of playgrounds, crossroads, and bridges.
(2) Spatial relationship coding:
A fixed-length string is used to store the spatial relationship codes. For each coded bit, the value range is limited to 0–35, 0–9 is coded as 0–9, and 10–35 are respectively coded with capital letters of A–Z.
For the central object to be coded, a certain number of nearest objects are searched. With one of the neighboring objects as reference, the other neighboring objects are coded according to the landuse type, distance, and angle in the order from near to far, forming a fixed length code, as shown in Figure 5.

In Figure 5, C_i is the neighboring object category code. D_0 and A_0 are distance code and angle code of the reference object. D_i and A_i ($i > 0$) are distance codes and angle codes of other neighboring objects. According to Figure 5, the length of the spatial relationship code is three times of N. D_0 and A_0 are coded with reference to major axis of the center object. To encode D_0, δ is calculated as follows:

$$\delta = \frac{n_0}{d}, \qquad (3)$$

where n_0 is the neighboring distance of the reference object. δ will be rounded and clamped to 0–35 to get the code D_0.

To encode A_0, the angle between the major axis of the central object and the neighboring baseline of the reference object is calculated, divided by 10.

Based on the neighboring baseline of the reference object, D_i and A_i of other neighboring objects are coded. In order to expand the range of distance code as much as possible and enhance the robustness, Equation 4 is used to calculate the stretching value of distance coefficient:

$$r_i = \log_{1.15}\zeta, \qquad (4)$$

where ζ is calculated as follows:

$$\zeta = \frac{n_i}{n_0} \quad (0 < i < N), \qquad (5)$$

where n_i is the neighboring distance of the ith other nearest object. Based on the same coding method, the r_i in Equation 4 will be rounded and clamped to 0–35 to get the code D_i. Angle code A_i directly calculates the deflection angle φ of the neighboring baseline relative to the reference object, and converts it to 0–360, which then will be divided by 10 and rounded to get A_i.

Spatial relationship code actually demarcates the grades of angle and distance. The similar coding values correspond to a certain angle
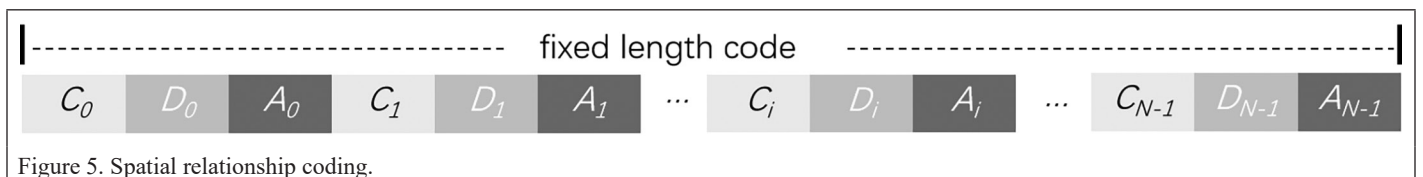
Figure 5. Spatial relationship coding.

or distance range, which ensures the robustness of machine perception algorithm of location to a certain extent.

(3) Selection of reference neighboring objects for spatial relationship coding:

For the same spatial object, choosing a different reference neighboring object will lead to different spatial relationship codes. Therefore, it is the premise of spatial object matching to select the same neighboring object for spatial relationship coding. In order to study the probability that different object data sets contain the same neighboring object, we still take the above-mentioned object pairs of Google and Tianditu as samples. For each pair, search m nearest objects in their own data set, and judge whether there is at least one same object. Count the number of object pairs which have the same neighbor under different *m* values, as shown in Figure 6.
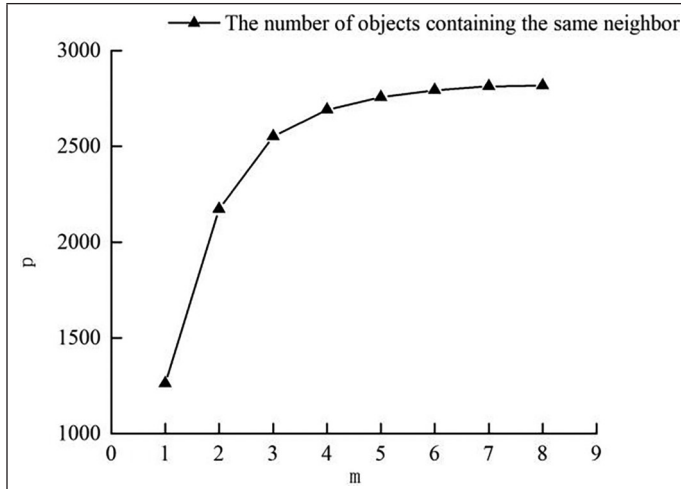
Figure 6. The number of objects with the same neighbor under different m values in the test area (*p* represents the number of object pairs which have the same neighbor, *m* represents the searched number of nearest neighbor objects).

It can be seen that when *m* takes 1, the number of object pairs which have the same nearest neighbor is 1261, only accounting for 25.6% and 29.1% of the total number of object pairs, respectively. When m takes 2, the value of *p* increases sharply, reaching 2173. Since then, the growth rate of *p* has been decreasing and the value of *p* approaching 2842.

Considering the matching rate and computational efficiency, the spatial relationship coding is constructed on the basis that m takes 2. For each spatial object, the nearest object and the next nearest object are used to construct its spatial relationship codes.

Establishment of Urban Surface Fingerprint Database
The spatial objects automatically extracted by computer are encoded and stored in the urban surface fingerprint database. For each of the spatial objects, the category code C, major axis d, projection coordinates, the spatial relationship code of the nearest object (FCode), and the next nearest object (SCode) are stored as a record, as shown in Table 5.

Table 5. Data table design of urban surface fingerprint database.

C	d	X	Y	FCode	SCode
1	91.22	11599...	3584...	2G021J23Q26627...	2DK20G22725N26...
...					

FCode = the spatial relationship code of the nearest object; SCode = the next nearest object.

MIP of Geographical Location

Technical Process of MIP of Geographic Location Based on Remote Sensing Image
Firstly, the spatial objects of regional remote sensing images are automatically detected by the Mask R-CNN model, and an urban surface fingerprint database is constructed. Then, the same Mask R-CNN model

is used to detect and encode the spatial objects contained in a local remote sensing image.

Finally, the fingerprint matching algorithm is used to calculate geographic location of the spatial objects in local remote sensing image based on the urban surface fingerprint database. The technical flowchart is shown in Figure 7.
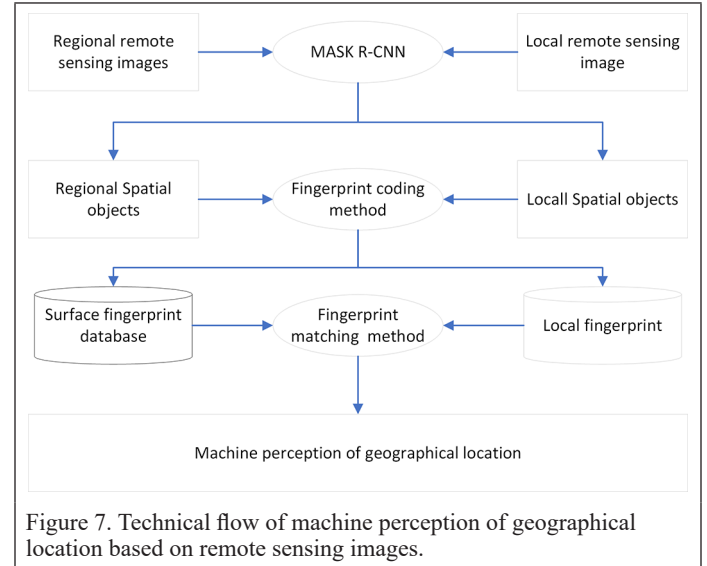
Figure 7. Technical flow of machine perception of geographical location based on remote sensing images.

Similarity Calculation of Spatial Object
(1) The similarity calculation algorithm:
It is assumed that a spatial object exists in both the fingerprint database and the local object set, and is represented as *S* and *L*, respectively. When using the spatial relationship codes to calculate the similarity between spatial objects *S* and *L*, their two codes match each other, and the maximum similarity among the four matches is taken as the similarity of *S* and *L*.

In each match in *S* and *L*, their codes are expressed as follows:

$$\begin{cases} F_S = \left\{ \left(C_i^S, D_i^S, A_i^S \right) \mid 0 \leq i < N \right\} \\ F_L = \left\{ \left(C_i^L, D_i^L, A_i^L \right) \mid 0 \leq i < N \right\} \end{cases}, \quad (6)$$

where F_S and F_L represent the code of S and L, and C_i, D_i, and A_i represent the category, distance, and angle codes of its neighboring objects, respectively. The equation for calculating the similarity of F_S and F_L is:

$$p_{SL} = \begin{cases} wp_1 & p_0 \geq a \\ 0 & p_0 < a \end{cases}, \quad (7)$$

where *w* is the matching coefficient, p_0 is the degree of the distance code matching of the reference object, p_1 is the average degree of code matching of other neighboring objects, and a is the similarity threshold. The equation to calculate p_0 is as follows:

$$p_0 = \begin{cases} 1 - \left(\left| D_0^S - D_0^L \right| \right)/20 & \left(C_0^S = C_0^L \right) \\ 0 & \left(C_0^S \neq C_0^L \right) \end{cases}. \quad (8)$$

w and p_1 both involve the matching of other neighboring objects. Take out one of other neighboring objects from *S* and *L*, respectively, and their similarity is:

$$p_{ij} = \begin{cases} \left(1 - \left|D_i^S - D_j^L\right|/5\right)\left(1 - \min\left(\left|A_i^S - A_j^L\right|, 36 - \left|A_i^S - A_j^L\right|\right)/5\right) & \left(C_i^S = C_i^L\right) \cap \left(\left|D_i^S - D_j^L\right| < 2\right) \\ 0 & \left(C_i^S \neq C_i^L\right) \cup \left(\left|D_i^S - D_j^L\right| \geq 2\right) \end{cases}, \quad (9)$$

where i and j represent the order number of each neighboring object of S and L, respectively.

A certain neighboring object in L traverses all other neighboring objects in S in turn, and the similarity is calculated according to Equation 9. If the maximum similarity is greater than or equal to α, it is considered that the neighboring object has found a match among the neighboring objects of S. Then, p_1 is calculated by Equation 10:

$$p_1 = \frac{1}{N_{SL}} \sum_{j=1}^{N_{SL}} p_{ij},\qquad(10)$$

where N_{SL} is the matching number of other neighboring objects. The matching coefficient w can be calculated by:

$$w = \begin{cases} 0.1\dfrac{N_{SL}-\beta}{N-\beta}+0.9 & N_{SL} >= \beta \\ 0 & N_{SL} < \beta \end{cases},\qquad(11)$$

where β is the minimum matching number of neighboring objects required for spatial object matching.

For each of objects in the local object set, traverses all objects in the fingerprint database to find the object with the maximum similarity. If the maximum similarity is greater than or equal to the similarity threshold α, take the object as the matching one.

(2) Determination of the number of nearest objects participating in coding: In order to obtain the best number of nearest objects participating in encoding, each object in Google data set and Tianditu data set is encoded. We set $\alpha = 0.75$ (which will be proved to be the best parameter later), increased β from 7 to 10, traversed the code of each object in the Tianditu data set, and searched for the matching object with the highest similarity from the Google data set. If they have the same identifier, the correct match is considered to be found. The number of correct matches is calculated, as shown in Table 6.

It can be seen from the table that when β is fixed, with the increase of N, the number of correct matches first increases and then remains stable or even decreases slightly. This means that in order to find the matched object from database, a certain number of nearest objects are required to construct a spatial relationship code. Because the objects extracted by Mask R-CNN are unreliable, too many nearest objects may have a negative impact on matching to a certain extent. Therefore, it is necessary to find a reasonable number of nearest objects participating in coding. As can be seen from the table, the peak value of N is related to β, which is about 2.4 to 2.7 times the value of β.

On the other hand, it is necessary to set a fixed length for spatial relationship code in the fingerprint database. Considering that in the actual matching, the larger the value of β, the higher the requirements for the number of objects extracted from the local remote sensing image, β is set to about 7–10, so N is set to 24 to encode spatial relationship with a length of 72. During the matching calculation, refer to Table 6 to obtain the best number of nearest objects from the spatial relationship code for calculation.

(3) Study on the optimal value of α and β: To get the optimal value of α and β, we also count the total matches P_t and correct matches P_r under different values of α and β, as shown in Figure 8.

As can be seen from the figure, when β is fixed, with the increase of a, P_t deceases and P_r increases first and then decreases, reaching a peak near 0.75. It shows that the optimal parameter of a is 0.75. Figure 8d shows the values of P_t and P_r under different conditions of β when $\alpha = 0.75$. It can be seen that with the increase of β, P_t is constantly decreasing while P_r increases first and then decreases, and reaches the optimum at 11.

Fingerprint Matching Algorithm
It can be seen from Figure 8, it is difficult to ensure that the object with maximum similarity is the correct one only considering the similarity of spatial relationship codes. Further filter is required. If there are two objects L_1 and S_1, L_1 is from the local object data set, S_1 is from the fingerprint database which matches L_1. The nearest N objects of L_1 and

Table 6. Correct matches with different number of nearest objects participating in coding.

	Correct Matches			
N	b = 7	b = 8	b = 9	b = 10
14	1579	1281	871	448
18	1783	1810	1723	1513
19	1795	1832	1825	1768
20	1767	1839	1846	1779
21	1745	1821	1866	1854
22	1730	1817	1886	1890
23	1726	1804	1866	1905
24	1715	1799	1854	1907
25	1703	1785	1847	1897
28	1702	1781	1830	1877
60	1679	1715	1751	1778

S_1 are searched respectively. If the number of neighboring objects is less than N, the actual number is used. Each of the neighboring objects of L_1 is represented as L_2. The best similar object of L_2, which is named as S_2, is searched from the neighboring objects of S_1. If S_2 is found, the rotation, skewing and scaling factors from the coordinate system of the local image to the coordinate system of the finger database are calculated by using the four objects, including L_1, L_2, S_1, and S_2. According to Equation 12, the factors are used to verify the matching effectiveness of spatial relationship code firstly.

$$|zd^L - d^S| \le \varepsilon,\qquad(12)$$

where z is the scaling factor, d^L and d^S are the major axis of the local object and the object in the fingerprint database, respectively, and ε is the distance threshold.

If the relationship between scaling factor and major axis satisfies Equation 12, the neighboring objects of L_1 are traversed and their real coordinates are calculated according to the rotation, skewing, and scaling factors. Within a distance of ε, the matched object for each of the neighboring objects of L_1 is searched from the neighboring objects of S_1 by their real coordinates. If the number of matches is equal to or bigger than 3, the fingerprint matching is considered successful.

Table 7 shows the accuracy of fingerprint matching under different values of ε when α is assigned to 0.75 and β is assigned to 7.

As can be seen from Table 7, ε is related to the spatial scale of the extracted object. With the increase of ε, both the number of total matches and the correct matches increase, but the correct rate decreases. If the correct rate is required to be at least 95%, the optimal value in the experimental data is about 50 m.

In order to study the improvement of the accuracy of fingerprint matching, α and ε are set to 0.75 and 50, respectively, and accuracy rate is compared to that of similarity matching of spatial relation code with different β values, as shown in Table 8. It can be seen from Table 8 that based on the similarity calculation of spatial relationship code, the matching results are further filtered by using fingerprint matching algorithm, and the filtered objects has more than 95% probability of being the correct matched object.

Fingerprint matching algorithm is the bedrock of machine perception for geographical location. In the local object set, as long as there is

Table 7. Matching accuracy of fingerprint matching under different values of ε.

ε (m)	Total Matches	Correct Matches	Correct Rate (%)
10	1413	1408	99.6
25	1619	1589	98.1
50	1746	1667	95.5
75	1867	1711	91.6
100	1976	1726	87.3
125	2099	1744	83.1
150	2443	1762	72.1
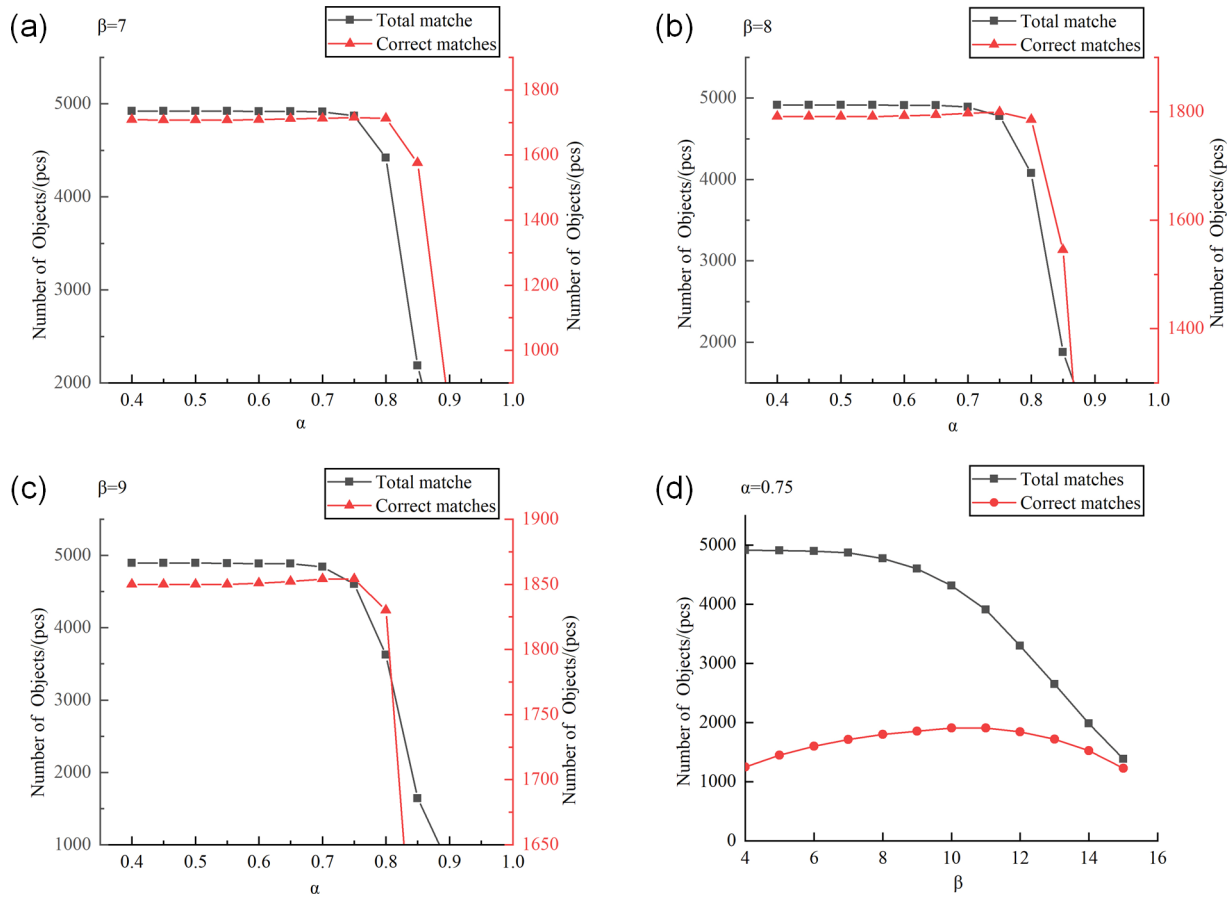
Figure 8. Parameter analysis of similarity calculation of spatial objects. (a) Total number of matches and correct number of matches when $\beta = 7$. (b) Total number of matches and correct number of matches when $\beta = 8$. (c) Total number of matches and correct number of matches when $\beta = 9$. (d) Total matching number and correct matching number when $\alpha = 0.75$. pcs = pieces.

one object whose matched object is founded from fingerprint database, we can use the matched object in the fingerprint database and its adjacent matched objects to automatically perceive the geographical location of the local remote sensing image.

Performance Evaluation of Fingerprint Matching Algorithm
In Table 8, we also calculated average matching time required for each object. The CPU of the experimental computer is an Intel® core (TIM) i7-7700. The matching time of a single local object is directly proportional to the number of records in the fingerprint database. The number of objects searched in the Google data set in the experiment is 4329, and the matching time is about 0.012s when β is equal to 7. According to this, when the number of spatial objects in the fingerprint database is less than about 360 000, the matching time of a single object will not exceed 1 s.

Experiments and Results

Establishment of Experimental Fingerprint Database in Major Cities of China
Taking major cities in China as examples, 18-level Google online satellite image were used to extract playgrounds, crossroads, and

bridges. Due to the irregularity of urban area, we only extracted spatial objects in the main urban area. For example, we only extracted the central area of Wuhan. As for Hangzhou, we only chose the urban area near Qiantang River. A total of 13 649 spatial objects were extracted, as shown in Table 9. The code of each spatial object was stored in the fingerprint database.

Table 9. Experimental fingerprint database of major cities in China.

City	Playground	Crossroad	Bridge	Total	Area (km²)	Density (per km²)
Fuzhou	276	1624	628	2528	710.41	3.55
Hangzhou	153	849	348	1350	306.33	4.41
Nanjing	606	1890	525	3021	740.21	4.08
Wuhan	475	1636	720	2831	776.86	3.64
Changsha	179	879	208	1266	270.58	4.68
Guangzhou	349	1299	1005	2653	679.33	3.91
Total	2038	8177	3434	13649	3483.72	3.92

Table 8. The accuracy rate and average matching time of each object of fingerprint matching compared to that of similarity matching of spatial relation code.

	Similarity Matching of Spatial Relation Code				Fingerprint Matching			
β	Total Matches	Correct Matches	Accuracy Rate (%)	Average Time (s)	Total Matches	Correct Matches	Accuracy Rate (%)	Average Time (s)
7	4661	1795	38.5	0.012	1746	1667	95.5	0.012
8	4449	1839	41.3	0.012	1765	1704	96.5	0.013
9	4359	1886	43.3	0.014	1803	1736	96.3	0.015
10	4316	1907	44.2	0.016	1829	1763	96.4	0.017

The Experiment of MIP of Urban Geographic Location

To prove the performance of the proposed method, we cut 200 local remote sensing images from Tianditu in different areas of the cities listed in Table 9.

We have ensured that the number of objects contained in each local image is greater than or equal to 7. In this experiment, the number of successful matches was 184 and the number of failures was 16, with a matching rate of 92%. Figure 9 shows two typical cases of MIP of geographical location. Figure 9a and 9d visualize two local areas of the urban surface fingerprint database. Figure 9b and 9e show local objects of two local areas extracted from local remote sensing images based on Tianditu online satellite images. Figure 9c and 9f show the fingerprint matching results in two cases. The first case shown in the first row contains all types of objects extracted, such as playground, crossroad, and bridge, of which 12 of the 17 objects are successfully matched. The second case shown in the second row contains only the extracted crossroads, of which eight of the nine objects are successfully matched.
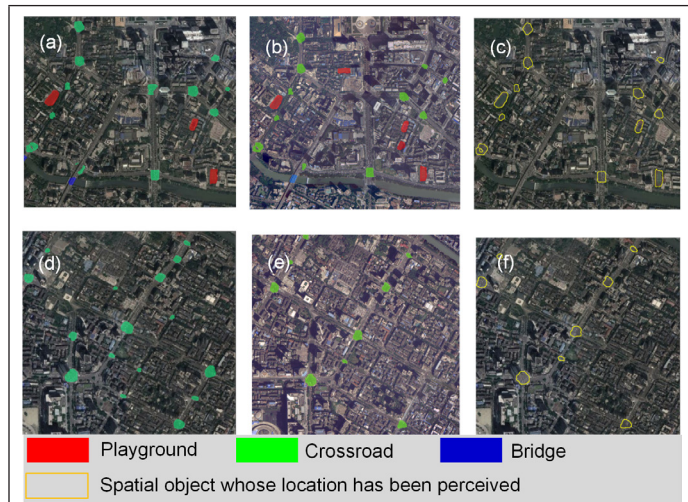
Figure 9. Two typical cases of MIP of geographical location. Local visualization (a) and (d) of urban surface fingerprint database for extracted objects from different areas of Google online satellite images. Local objects (b) and (e) extracted from the two areas of local remote sensing images (based on Tianditu online satellite images). Location perception results (c) and (f) of the two areas.

Method Adaptability Analysis

We tried to scale and distort local images to test the performance of machine geographical location perception under different conditions. In Figure 10a, we rotated the original local image by 12° and reduced the resolution from 0.597 m to 0.70 m. Figure 10b shows the location perception results. This proves the angle independence and scale independence of fingerprint matching.

In Figure 10c, we distorted the origin local image as shown in Figure 9b to a certain extent. Most of the perceived objects in Figure 10d are the same as those in Figure 9c. This proves that the fingerprint matching has a certain degree of robustness. Compared with Figure 9c, the imperceptible objects mainly come from areas where the degree of distortion exceeds the matching parameter ε of Equation 12, or the local deformation exceeds the recognition ability of the model.

Although the fingerprint matching algorithm is scale independent, the object extracted by Mask R-CNN is closely related to the spatial scale. In order to test the sensitivity of the image resolution, we resampled the local image shown in Figure 9b according to the multiples of 0.25, 0.5, 0.7, 1.2, 1.5, and 2.0, respectively. The objects extracted by Mask R-CNN are shown in Figure 11a– f.

It can be seen from the figure that the Mask R-CNN model has a most suitable resolution range. In this example, except for the resolution of 0.150 m and 1.194 m, the objects extracted from other images can be used to complete machine location perception successfully, which reflects that the spatial scale of this method has a certain degree of
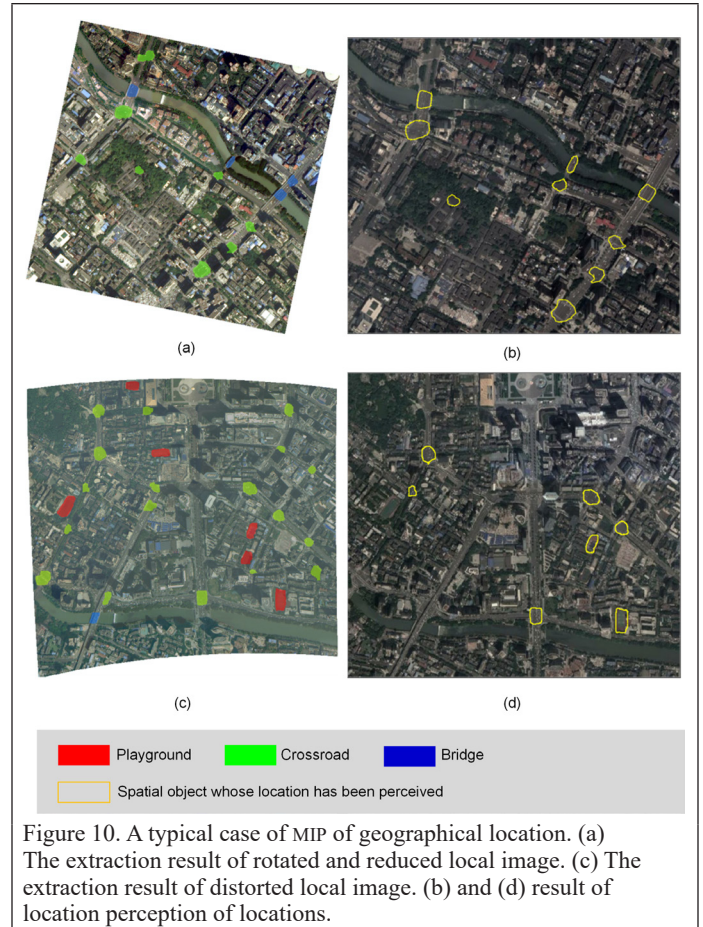
Figure 10. A typical case of MIP of geographical location. (a) The extraction result of rotated and reduced local image. (c) The extraction result of distorted local image. (b) and (d) result of location perception of locations.
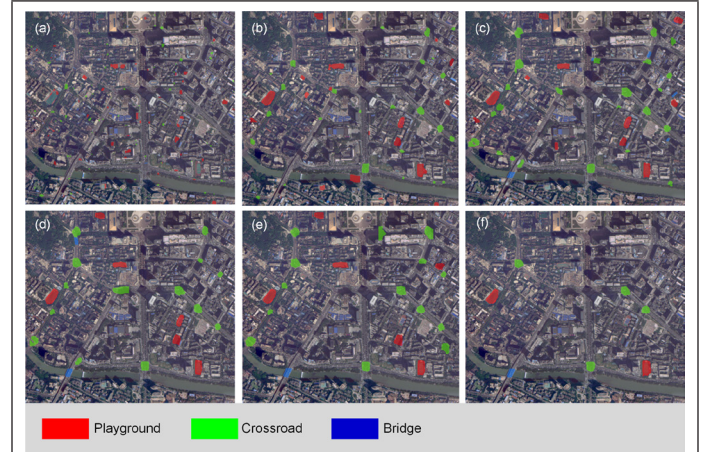
Figure 11. Object extraction result of the resampled local image with different resolutions.

robustness to a certain extent. However, if the resolution is too small or too large, such as 0.150 m and 1.194 m in this example, the spatial scale of the image exceeds the best suitable range of Mask R-CNN model, resulting in huge differences between the local fingerprint and the fingerprint database and unable to complete machine location perception.

Discussion

Through the above experiments, we find that the method of location intelligent perception has high accuracy for urban high-resolution images, and has angle independence, certain robustness, and spatial scale independence. Because this method is based on Mask R-CNN to extract spatial objects, the ability of machine location perception is limited by this model. In order to further improve the machine's ability to precept the location, there are several potential problems should be considered.

The first problem is the distribution density of extracted objects. As shown in Table 9, the density of extracted objects is greater than 3.5 per km^2, which means that if the coverage area of the local urban image is more than 2 km^2, the number of objects may exceed 7, and computers will be able to find the position automatically. However, there are some errors in the object extraction by Mask R-CNN, the minimum area requirement of local image for machine perception position may be greater than 2 km^2, which depends on the quality of the local image and the number of objects contained.

The second problem is the similarity of object distribution between the local image and fingerprint database. If there are great differences in imaging time and image quality between the local image and the image used in the establishment of fingerprint database, the number of effective spatial objects extracted from the remote sensing image will be insufficient to realize location perception. It is necessary to update the fingerprint database at any time.

The third challenge is the consistency between the spatial scale of local image and that of fingerprint database. Although Mask R-CNN has certain spatial scale robustness, it still has a suitable spatial scale range. To correctly perceive the location, the spatial scale of local image and fingerprint database must be similar.

It is noted that the key parameters are based on the data of the experimental area, which may deviate from the ideal parameters.

Conclusion

A preliminary study on MIP of geographical location based on high-resolution remote sensing images is carried out. First, the surface fingerprint is defined as the unique identification of the surface. In order to achieve MIP of geographical location, the instance segmentation model Mask-RCNN is introduced, and a relatively reliable model of extracting spatial object is automatically obtained through sample training. Then, the position, attribute, morphological, and spatial relationship features of the spatial objects are analyzed. It is found that the gravity center is superior to other location measurement, and the neighboring relationship features of the spatial object are more stable than the morphological features. Therefore, a location measurement method for spatial objects based on gravity center and a spatial relationship measurement method based on neighboring baseline are proposed. The surface fingerprint database is constructed by encoding the spatial relationship of 24 nearest objects for each of the spatial objects. Through the spatial object coding similarity algorithm and fingerprint matching algorithm, the technical route of MIP of geographic location based on remote sensing images is formed.

Finally, through the experiments of geographical location machine perception in major cities of China, the feasibility of this method is proved, which provides a new method for the in-depth study of geographical location MIP. In future work, we will enrich the diversity of spatial object categories, and build fingerprint databases with multiple spatial scales to further improve the accuracy of MIP.

Acknowledgment

References

Abrams, M. 2017. Global geoscience maps from ASTER data. Pages 4477–4478 in *Proceedings IEEE International Geoscience and Remote Sensing Symposium*. https://doi.org/10.1109/IGARSS.2017.8127994.

Bay, H., T. Tuytelaars and L. V. Gool. 2006. SURF: Speeded up robust features. Pages 404–417 in *Proceedings of the 9th European Conference on Computer Vision—Volume Part I*, held in Graz, Austria, 7–13 May 2006. Edited by A. Leonardis, H. Bischof and A. Pinz. Berlin: Springer-Verlag.

Chen, M., Z. Shao, C. Liu and J. Liu. 2013. Scale and rotation robust line-based matching for high resolution images. *Optik—International Journal for Light and Electron Optics* 124(22):5318–5322.

Chen, X., R. Girshick, K. He and P. Dollar. 2019. TensorMask: A foundation for dense object segmentation. Pages 2061–2069 in *Proceedings 2019 IEEE/CVF International Conference on Computer Vision (ICCV)*. https://doi.org/10.1109/ICCV.2019.00215.

Fan, Z. and Q. Zhao. 2012. A data-clustering based robust SIFT feature matching method. *Journal of Computer Research and Development* 49(5):1123–1129.

He, K., G. Gkioxari, P. Dollár and R. Girshick. 2017. Mask R-CNN. *IEEE Transactions on Pattern Analysis and Machine Intelligence* 42(2): 386–397.

Hewson, R. and D. Robson. 2014. Evaluating the information content of National ASTER geoscience maps in the Wagga Wagga and Cobar regions of New South Wales. *Preview*:45–49.

Jiang, X., J. Ma, G. Xiao, Z. Shao, X. Guo. 2021. A review of multimodal image matching: Methods and applications. *Information Fusion* 11(2021):22–71.

Kovacs, A. and T. Sziranyi. 2013. Improved Harris feature point set for orientation-sensitive urban-area detection in aerial images. *IEEE Geoscience and Remote Sensing Letters* 10(4):796–800.

Lee, Y. and Park, J. 2020. CenterMask: Real-time anchor-free instance segmentation. Pages 13903–13912 in *Proceedings 2020 IEEE/CVF Conference on Computer Vision and Pattern Recognition (CVPR)*, held in Seattle, Wash., 13–19 June 2020.

Liu, Z., J. An and J. Yu. 2012. A simple and robust feature point matching algorithm based on restricted spatial order constraints for aerial image registration. *IEEE Transactions on Geoscience and Remote Sensing* 50(2):514–527.

Matsuoka, M. and S. Midorikawa. 1993. Prediction of isoseismal map for large area using the digital national land information. *Journal of Structural and Construction Engineering* 447:51–56.

Moosavi, V. 2017. Contextual mapping: Visualization of high-dimensional spatial patterns in a single geo-map. *Computers, Environment and Urban Systems* 61(Part A):1–12.

Rublee, E., V. Rabaud, K. Konolige and G. Bradski. 2011. ORB: An efficient alternative to SIFT or SURF. Pages 2564–2571 in *Proceedings IEEE International Conference on Computer Vision*, held in Barcelona, Spain, 6–13 November 2011. https://doi.org/10.1109/ICCV.2011.6126544.

Rucheng, L. U., H. Xianjin, Z. Tianhui, X. Sisi, Z. Xingyu and Z. Xiaofeng. 2009. Construction of land use information Tupu in the rapidly developing regions: A case study of the surrounding regions of Taihu Lake in Jiangsu Province. *Resources Science*:49–57.

Su, J., Q. Xu and J. Zhu. 2010. A scene matching algorithm based on SURF feature. Pages 434–437 in *Proceedings IEEE International Conference on Image Analysis and Signal Processing*, held in Xiamen, China. https://doi.org/10.1109/IASP.2010.5476080.

Tong, J., J. Yu, C. Wu and G. Yu. 2021. Health information acquisition and position calculation of plug seedling in greenhouse seedling bed. *Computers and Electronics in Agriculture* 185(3):106146.

Vishwakarma, A. and M. K. Bhuyan. 2020. Image mosaicking using improved auto-sorting algorithm and local difference-based Harris features. *Multimedia Tools and Applications* 79(1):23599–23616.

Wang, X. G., F. C. Wu and Z. H. Wang. 2008. Harris feature vector descriptor (HFVD). Pages 1–4 in *Proceedings IEEE International Conference on Pattern Recognition*. https://doi.org/10.1109/ICPR.2008.4760977.

Wu, Y. 2019. Research on feature point extraction and matching machine learning method based on light field imaging. *Neural Computing and Applications*:8157–8169.

Yang, H., X. Li, L. Zhao and S. Chen. 2019. A novel coarse-to-fine scheme for remote sensing image registration based on SIFT and phase correlation. *Remote Sensing* 11(15):1833.

Yao, L., H. Feng, Y. Zhu, Z. Jiang, D. Zhao and W. Feng. 2009. An architecture of optimised SIFT feature detection for an FPGA implementation of an image matcher. Pages 30–37 in *Proceedings IEEE International Conference on Field-Programmable Technology*. https://doi.org/10.1109/FPT.2009.5377651.

Zhou, H., Y. Yuan and C. Shi. 2009. Object tracking using SIFT features and mean shift. *Computer Vision and Image Understanding* 113(3):345–352.

IN-PRESS ARTICLES

Gaofei Yin. Smartphone Digital Photography for Fractional Vegetation Cover Estimation.

Xuzhe Duan, Qingwu Hu, Pengcheng Zhao, and Shaohua Wang. A low-cost and portable indoor 3D mapping approach using biaxial line laser scanners and a one-dimension laser rangefinder integrated with MEMS.

Toshihiro Sakamoto, Daisuke Ogawa, Satoko Hiura, Nobusuke Iwasaki. Alternative procedure to improve the positioning accuracy of orthomosaic images acquired with Agisoft Metashape and DJI P4 Multispectral for crop growth observation

Guangyun Li, Senzhen Sun, Yangjun Gao, Li Wang. Robust Dynamic Indoor Visible Light Positioning Method Based on CMOS Image Sensor.

Zhenfeng Shao, Hongping Zhang, Wenfu Wu, Xiao Huang, Jisong Sun, Jinqi Zhao, Yewen Fan. Comparing the sensitivity of pixel-based and sub-watershed-based AHP to weighting criteria for flood hazard estimation.

Gang Qiao, Hongwei Li. Lake Water Footprint Determination Using Linear Clustering-based Algorithm and Lake Water Changes in the Tibetan Plateau from 2002 to 2020.

Jason Parent, Chandi Witharana, Michael Bradley. Classifying and georeferencing indoor point clouds with ARCGIS.

Paul Pope, Brandon Crawford, Anita Lavadie-Bulnes, Emily Schultz-Fellenz, Damien Milazzo, Kurt Solander, Carl Talsma. Towards Automated/Semi-Automated Extraction of Faults from Lidar Data

Li Tan, Guoming Li, Xin Liu, Aike Kan. Feature-based convolutional neural network for very-high-resolution urban imagery classification

Ravi Dwivedi, Syed Azeemuddin. Conjunctive use of Landsat-8 OLI and MODIS Data for Delineation of Burned Areas

Chih-Hung Hsu, Che-Hao Chang, Chih-Tsung Hsu, Shiang-Jen Wu, Po-Hsien Chung. Hydrological Topography Dataset (HTD) - the Dataset for High Resolution 2D Urban Flood Modeling.

Xiaojun Yang, Feilin Lai. Improving land cover classification over a large coastal city through stacked generalization with filtered training samples.

Xiaoyue Wang, Hongxin Zhang, Dailiang Peng. Evaluation of urban vegetation phenology using 250 m MODIS vegetation indices.

Zhihua Xu, Xingzheng Lu, Wenliang Wang, Ershuai Xu, Rongjun Qin, Yiru Niu, Xu Qiao, Feng Yang, Rui Yan. Monocular Video Frame Optimization through Feature-based Parallax Analysis for 3D Pipe Reconstruction.

Lin Ding, Hanchao Zhang, Deren Li, Monitoring and Analysis of Urban Sprawl based on Road Network Data and High-resolution Remote Sensing Imagery: A Case Study of China's Provincial Capitals.

Xueyan Li, Heqing Zhang, Zhenxin Wang, Junfeng Song. Transformer for the Building Segmentation of Urban Remote Sensing.

Identifying the Driving Factors of Urban Land Surface Temperature

Lifeng Liang, Benhua Tan, Sicheng Li, Zhiming Kang, Xiujuan Liu, and Lihua Wang

Abstract

Land surface temperature (LST) has a profound impact on urban climate and ecology, and is widely used to quantify surface urban heat islands. The spatial heterogeneity of LST is affected by natural and human factors, with seasonal differences. This study selected Dongguan, a rapidly urbanizing city in China, as an example to analyze the relationship between the spatial heterogeneity of LST in different seasons and influencing factors in six dimensions. Multi-source spatial data were combined, including Landsat images, meteorological data, digital elevation models, National Polar-Orbiting Partnership Visible Infrared Imaging Radiometer Suite nighttime light, and points of interest. The results show that spatial patterns of LST across different seasons were consistent, although there were local differences. Based on the GeoDetector model, the result indicated differences between separate effects and interactive effects, and identified the high temperature risk areas.

Introduction

Land surface temperature (LST) is a key parameter affecting the balance of land surface radiation, climate, and environmental changes (K. Wang and Liang 2009). During rapid urbanization, the extent to which human activities affect and transform the land surface increases. The natural land surface is replaced by an artificial surface, which causes the urban land surface temperature to be significantly higher than the suburban land surface temperature, and surface urban heat islands (SUHIs) have become a global urban environmental problem, with a profound impact on health, energy consumption, economic development, and biological phenology (Faroughi *et al.* 2020; Y. Li *et al.* 2020; Mirzaei *et al.* 2020; X. Li *et al.* 2021).

LST inversion is the premise underpinning the quantitative analysis of the spatial heterogeneity of LST; the commonly used methods are mainly divided into two categories. The first method uses meteorological data recorded by ground stations, combined with mathematical statistics, to analyze temperature differences between urban and suburban areas, then analyzes the characteristics of spatial differences in LST (Eludoyin *et al.* 2014). The second method is a quantitative inversion of the LST based on thermal infrared remote sensing data. Compared with observed data from traditional ground meteorological stations, the latter offer wide coverage and high resolution, providing support for research on LST in widespread areas (Liu *et al.* 2021). Currently, Moderate Resolution Imaging Spectroradiometer (MODIS), Landsat, and Advanced Very High Resolution Radiometer (AVHRR) satellite data are widely used to evaluate the spatial distribution of LST (Balling

and Brazel 1998; T. Liu *et al.* 2015; Zhao *et al.* 2021). The radiation transfer equation method proposed by Sobrino is based on the Landsat Thematic Mapper 5 with high accuracy (Sobrino *et al.* 2004; Y. Wang *et al.* 2021).

Research on the spatial heterogeneity of LST is essential for analyzing the formation and evolution of SUHIs, which can also can help improve the quality of life for residents, enhance the health of urban ecology, and provide pertinent information for the formulation of sustainable development strategies (Zhou *et al.* 2017). Analysis of the spatial heterogeneity of LST comprises two key decision points: the selection of driving factors and the selection of the analysis method. For the first decision, most researchers tend to select a single factor and ignore the influence of comprehensive factors such as meteorology, landscape pattern, and social development. Liu *et al.* (2021) analyzed the impact of land cover types on the spatial patterns of LST in Tokyo from 2001 to 2015; Baldinelli and Bonafoni (2015) suggested that albedo was the dominant factor affecting the spatial variability of LST in Florence, Italy; and Huang *et al.* (2016) compared MOD11A2 surface temperature data with Defense Meteorological Satellite Program Operational Linescan System nighttime light remote sensing data and analyzed the impact of socioeconomic activities on the spatial differentiation of LST. Hua *et al.* (2020) analyzed the relationship between SUHIs, impervious surface, and vegetation coverage in Xiamen, China, and concluded that the coverage of impervious surface is closely related to changes in SUHIs.

For the second decision, previous studies have mainly identified the dominant factors using traditional mathematical statistical methods, such as geographically weighted regression, ordinary least-squares regression analysis, or Pearson correlation analysis. However, these methods neglect the influence of interactions between different influencing factors on LST, which makes it difficult to carry out in-depth research on the spatial heterogeneity of LST or SUHIs (Chen *et al.* 2017). J. F. Wang and Hu (2012) proposed the GeoDetector model, which is a geospatial statistical method that can be used to analyze the spatial heterogeneity of geographical phenomena and reflects underpinning drivers. This method does not need to consider the collinearity of independent variables, and has been applied to quantify the impact of potential driving factors on geographic phenomena (Zhu *et al.* 2020).

Dongguan city was selected as the research area. Remote sensing data, digital elevation models, points of interest, and other spatial data served as the data sources, which were combined with the GeoDetector model to compensate for two shortcomings identified in the literature and designed to address two research questions:

(1) How do natural and human factors such as topography, meteorology, vegetation, water bodies, socioeconomics, surface reconstruction intensity, and landscape patterns affect the spatial heterogeneity of LST?
(2) How do the interactive effects of the driving factors influencing the spatial heterogeneity of LST differ from the separate effects?

Lifeng Liang, Sicheng Li, Zhiming Kang, and Xiujuan Liu are with the School of Geographical Sciences, Lingnan Normal University, Zhanjiang, 524048, China (Xiujuan Liu: 544022065@qq.com).

Benhua Tan is with the Department of Geography and Spatial Information Techniques, Ningbo University, Ningbo, 315211, China.

Lihua Wang is with the Department of Geography and Spatial Information Techniques, Collaborative Innovation Center for Land and Marine Spatial Utilization and Governance Research, Ningbo University, Ningbo, 315211, China (wanglihua1@nbu.edu.cn).

Methodology

Study Area

Dongguan city is located on the east coast of the Pearl River Estuary, south of the cities of Guangzhou and Huizhou and north of Shenzhen (an important node city in the Guangdong–Hong Kong–Macao Greater Bay Area; Figure 1). Dongguan comprises four subdistricts and 28 towns, and is one of the five prefecture-level cities in China without districts, spanning a total area of 2465 km[2]. The terrain in Dongguan city has a high elevation in the southeast but low in the northwest, and the city is composed of various geomorphic types, including alluvial plains, hills, and flat terraces. Dongguan city has a subtropical marine monsoon climate characterized by long summers, short winters, and a rainy season mainly concentrated in summer and autumn. The average rainfall in 2019 was 1912.3 mm. As the forefront of the reform and opening up of China, Dongguan is known as the "world's factory." Over the past 30 years (1990–2020), the area of cultivated land and forests in Dongguan has decreased from 472.4 and 609.87 km[2], respectively, to 359.2 and 332.53 km[2]; accordingly, built-up area has increased from 82.48 to 1139.83 km[2] over this time, and the size of the urban population increased from 60.04% in 2000 to 92.15% in 2020. With the expansion of urban land, changes in surface morphology, and rapid population growth, Dongguan exemplifies a city that has undergone rapid urbanization. This rapid change inevitably aggravated the local heat island effect, and has attracted attention from researchers in various fields.

Data Sets and Variables

The data sets used in this study span from June 2019 to February 2021, and mainly comprise remote sensing imagery, alongside meteorological, topographic, and socioeconomic data. The remote sensing images of Dongguan include Landsat-7 and Landsat-8 (path 122/row 44) and National Polar-Orbiting Partnership Visible Infrared Imaging Radiometer Suite nighttime light data for different months, provided by the US Geological Survey[1] and National Oceanic and Atmospheric Administration,[2] respectively. Landsat data were used to characterize LST for different seasons and to calculate vegetation coverage, albedo,

1. <http://earthexplorer.usgs.gov/>
2. <https://eogdata.mines.edu/download_dnb_composites.html>
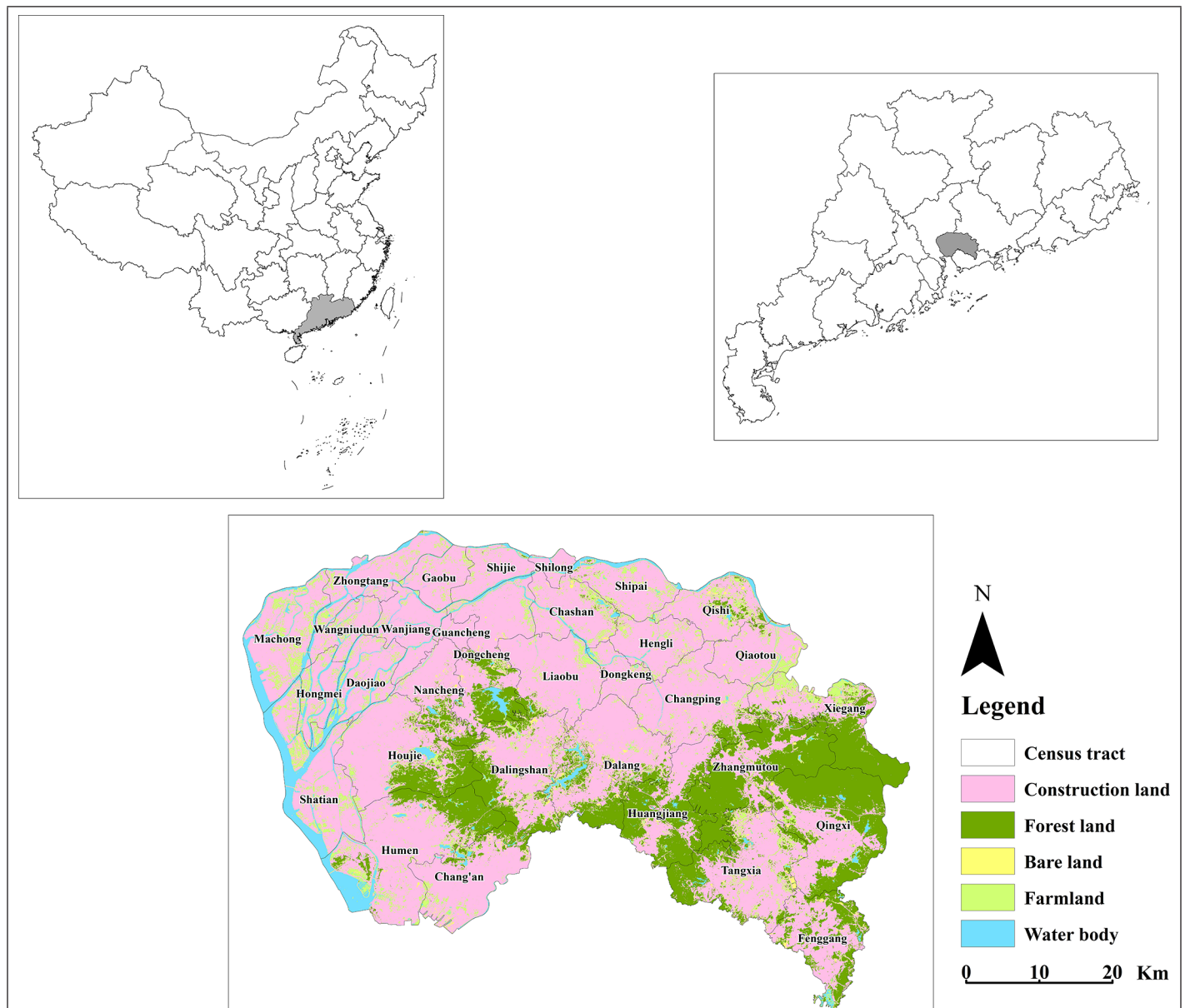
Figure 1. (a) Guangdong Province, located in the south of China. (b) Dongguan city, located on the east coast of the Pearl River Estuary, south of the cities of Guangzhou and Huizhou and north of Shenzhen. (c) Land cover/land use imagery in study area, acquired by *Landsat-8* through supervised classification of a random-forest model.

improved normalized difference water index (MNDWI), and normalized difference impervious surface index (NDISI; S. Liang 2001; Xu 2005, 2010; Yang *et al.* 2015). In addition, land use and land cover data were obtained from supervised classification of Landsat-8 Operational Land Imager/Thermal Infrared Sensor data through a random-forest model, which involved five categories: water bodies, architecture, forests, farmland, and bare land (Vander *et al.* 2015). The landscape pattern indexes CONTAG, the Shannon diversity index, DIVISION, and COHESION can be calculated from the land cover/land use data (Xiong and Zhang 2021). These constitute important factors of the LST. The National Polar-Orbiting Partnership Visible Infrared Imaging Radiometer Suite nighttime light data were used to reflect how the intensity of anthropogenic activity was spatially distributed. The meteorological data were provided by the National Earth System Science Data Center, at the National Science and Technology Institute of China.[3] This data set included four types of grid data, with a resolution of 1 km: monthly average temperature, rainfall, humidity, and wind speed. The topographic data included the Advanced Spaceborne Thermal Emission and Reflection Radiometer Global Digital Elevation Model and slope data sets. The former was provided by the Geospatial Data Cloud (China)[4], and the latter was extracted from the digital elevation model using the ArcGIS slope calculation tool (Environmental Systems Research Institute, Inc., Redlands, CA). Socioeconomic data were extracted from the points-of-interest data set sourced from Gaode Map (China) using an application programming interface, which contains locational and functional information such as latitude, longitude, and address. As the coordinate system and resolution of these data were inconsistent, it was necessary to preprocess them and unify their resolutions and coordinate systems to 1 km and UTM WGS-84, respectively. Finally, an influencing-factor system was constructed, with two first-level indicators, six second-level indicators, and 16 third-level indicators (Figure 2).

Inversion of LST in Different Seasons

Delineation of seasons is the prerequisite for analyzing the spatial heterogeneity of LST in different seasons. We referred to the method of season division in the adjacent area of Shenzhen city (Peng *et al.* 2018) and used Python to process monthly average temperature data sets from 2001 to 2020 and establish a violin plot (Figure 3), which can reflect the distribution and probability density of temperature. According to the information provided by the violin plot about the monthly maximum, minimum, and change of temperature in Dongguan in the past 20 years, the seasons in Dongguan city were divided into three: summer (June, July, August, and September), the transition season (April, May, October, and November), and winter (December, January, February, and March).

The calibration parameters of band 11 of the Landsat-8 Thermal Infrared Sensor contain errors, and there is a lack of a reasonable correction scheme. Therefore, the US Geological Survey recommends single-band inversion of LST. Based on the availability of calculation parameters, the radiation transfer equation method was used, with Equations 1 and 2 for LST inversion and Equation 3 to calculate the heat index:

$$L_T = [L - L^\uparrow - \tau(1 - \varepsilon)L_\downarrow]/(\varepsilon\tau) \tag{1}$$

$$T = K_2/\ln(K_1/L_T + 1) \tag{2}$$

$$\mathrm{HI} = (T - \overline{T})/\overline{T} \tag{3}$$
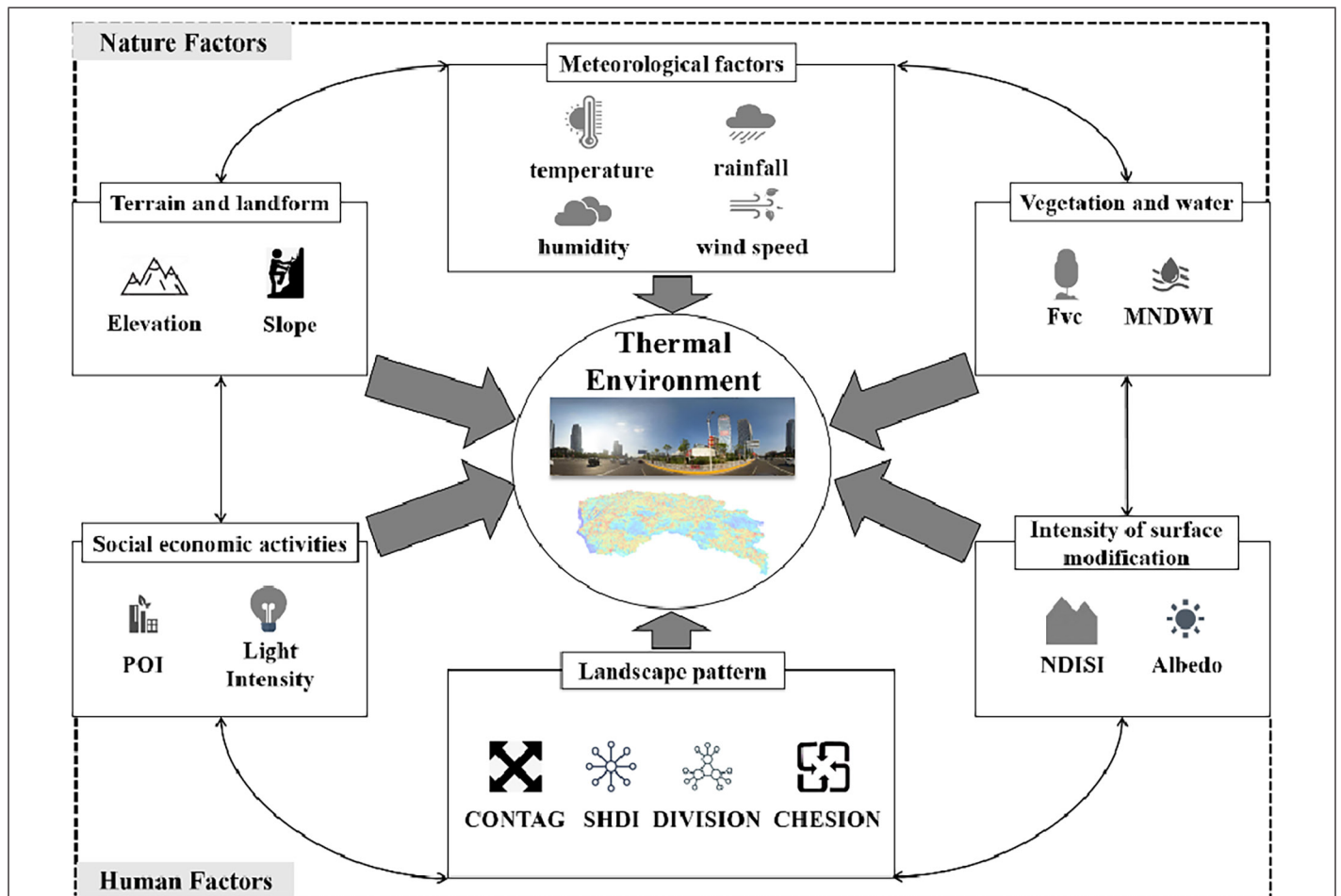
Figure 2. Natural and human geographic factors.
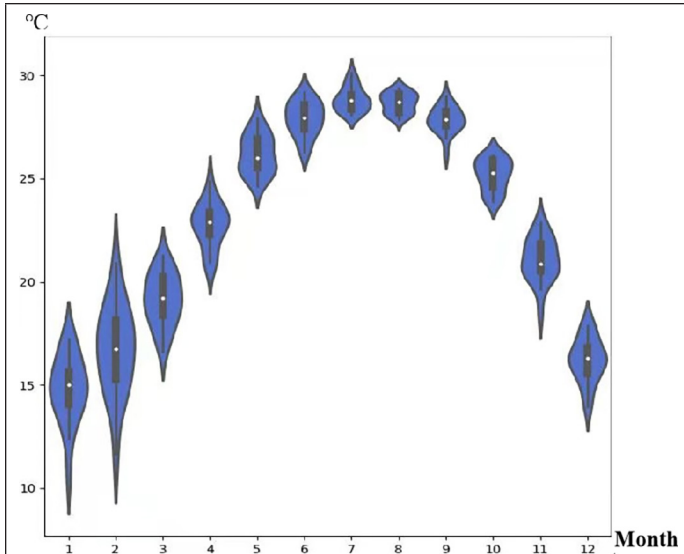
Figure 3. Violin plot of monthly average temperatures for 2001–2020.

where L represents the radiation brightness of the thermal infrared band; $L^{\uparrow}$ and $L_{\downarrow}$ are the upward and downward radiation brightness of the atmosphere; ε is the atmospheric transmittance in thermal infrared bands, obtained by inputting the location and imaging time through the National Aeronautics and Space Administration website[5]; τ represents surface emissivity, which was calculated using the mixed-pixel method; L_T, T, and $\overline{T}$ respectively represent the radiation brightness of the black body, LST, and average LST; and K_1 and K_2 represent the calibration parameters, which were obtained by querying the image header file.

The heat index can be calculated after obtaining the LST; we then divided it into seven ascending levels of heat-island intensity using the division method of mean and SD (Table 1): high cold island, relatively cold island, weak cold island, no heat island, weak heat island, relative heat island, and high heat island.

Table 1. Division method with mean and SD coefficient of variation for the thermal field.

HI Interval	Class
HI < u − 2.5SD	High cold island
u − 2.5SD ≤ HI < u − 1.5SD	Relatively cold island
u − 1.5SD ≤ HI < u − 0.5SD	Weak cold island
u − 0.5SD ≤ HI < u + 0.5SD	No heat island
u + 0.5SD ≤ HI < u + 1.5SD	Weak heat island
u + 1.5SD ≤ HI < u + 2.5SD	Relative heat island
HI ≥ u + 2.5SD	High heat island

HI = heat index; u = mean coefficient of variation for the thermal field.

GeoDetector Model

The GeoDetector model consists of four detectors: factor, interaction, risk, and ecological. The factor detector is the dominant parameter used to identify geographic phenomena. The interaction detector is used to analyze the explanatory power of the combined effect of two influencing factors on geographic phenomena. The risk detector is used to assess whether there are significant differences between two subregions. The ecological detector is used to compare the effects of two driving factors on geographic phenomena. The purpose of this study was to detect the effects of interactions between the dominant and driving factors underpinning the spatial heterogeneity of LST and to identify whether there are significant differences in LST between

5. <https://atmcorr.gsfc.nasa.gov/>
6. <http://data.cma.cn/>

different subregions. Therefore, the factor, interaction, and risk detectors were used to comprehensively analyze the underlying drivers of spatial heterogeneity of SUHIs.

Factor Detector
By calculating q according to Equation 4, it was possible to quantitatively evaluate the explanatory power of each driving factor in the spatial heterogeneity of LST. The range of q was [0,1]; the larger the value, the more significant the influence of the factor on LST heterogeneity.

$$q = 1 - \frac{\sum_{h=1}^{L} N_h \sigma_h^2}{N\sigma^2} = 1 - \frac{\text{SSW}}{\text{SST}} \tag{4}$$

$$\text{SSW} = \sum_{h=1}^{L} N_h \sigma_h^2, \quad \text{SST} = N\sigma^2 \tag{5}$$

In these equations, N_h denotes that the subregion is composed of h units; $h = 1, 2, \ldots, N$ is the total number of units in the study area; and SSW and SST are the sum of variance and total variance.

Interaction Detector
The interaction detector explores whether the LST intensity changes from the combination of different factors X_1 and X_2 by calculating q for two driving factors. The interactive relationships between two factors are of the following types:
1. Nonlinear–weaken: $q(X1 \cap X2) < \min(q(X1), q(X2))$
2. Uni-enhance/weaken: $\min(q(X1), q(X2)) < q(X1 \cap X2) < \max(q(X1), q(X2))$
3. Bi-enhance: $q(X1 \cap X2) > \max(q(X1), q(X2))$
4. Independent: $q(X1 \cap X2) = q(X1) + q(X2)$
5. Nonlinear–enhance: $q(X1 \cap X2) > q(X1) + q(X2)$

Risk Detector
The main function of the risk detector is to search for units with potential high temperature risk. The mean difference in the heat-island intensity of different units is tested using the value; the larger the value, the greater the high temperature risk of the unit, defined as the risk range of UHI:

$$t_{\overline{y}_{h=1} - \overline{y}_{h=2}} = \frac{\overline{Y}_{h=1} - \overline{Y}_{h=2}}{\left[\frac{\text{Var}\left(\overline{Y}_{h=1}\right)}{n_{h=1}} + \frac{\text{Var}\left(\overline{Y}_{h=2}\right)}{n_{h=2}}\right]^{1/2}} \tag{6}$$

where $\overline{Y}_h$ represents the mean value of the heat-island intensity in h units, n_h represents the number of samples, and Var represents the variance.

Results

Statistical Analysis
Based on temperature data for Dongguan recorded by the National Meteorological Science Data Center,[6] the temperature ranges on 15 June and 14 November 2019, and 8 February 2020 were 23.7°C to 34°C, 19.3°C to 26°C, and 8.6°C to 18°C, respectively. Based on the LST statistical results, 92.47% of the study area had temperatures between 23°C and 37°C on 15 June, 86.75% had temperatures between 18°C and 29°C on 14 November, and 92.41% had temperatures between 10°C and 21°C on February 18. The LST retrieval from Landsat series remote sensing data was highly consistent with temperature data recorded on the same day. This indicates that LST retrieval by the radiation transfer equation method is reliable.

Seasonal Changes in LST Spatial Patterns
Figure 4a–c shows that LST in Dongguan during different seasons has a similar spatial pattern and presents an irregular ring-shaped distribution of heat island, no heat island, and cold island. The low-temperature zone is distributed in forests, ecological parks, rivers, and lakes, such as the Tongsha Ecological Park (Figure 4a4), Foling Reservoir (Figure
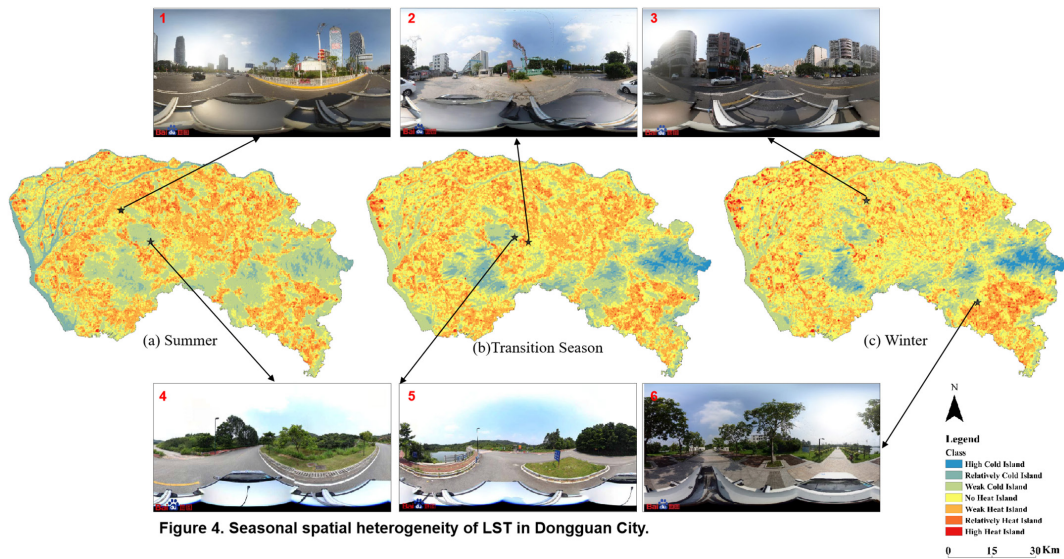
Figure 4. Seasonal spatial heterogeneity of land surface temperature in Dongguan.
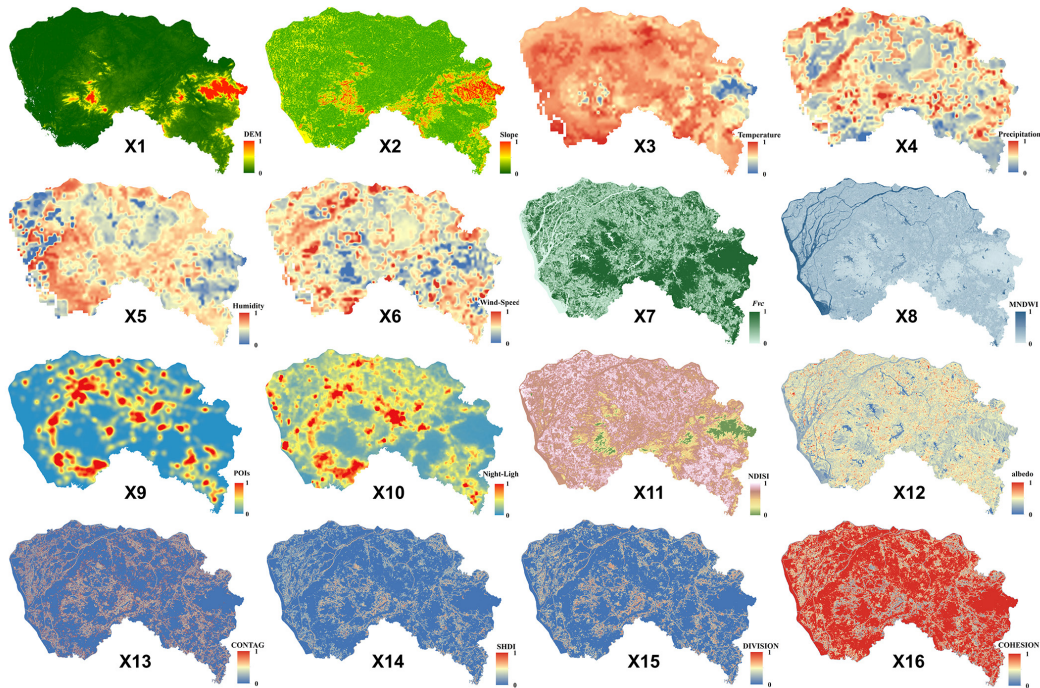
Figure 5. The results of normalization: (X1) DEM, (X2) slope, (X3), temperature, (X4) rainfall, (X5) humidity, (X6) wind speed, (X7) Fvc, (X8) MNDWI, (X9) POI, (X10) light intensity, (X11) NDISI, (X12) albedo, (X13) CONTAG, (X14) SHDI, (X15) DIVISION, (X16) COHESION. DEM = digital elevation model; MNDWI = improved normalized difference water index; NDISI = normalized difference impervious surface index; POI = points of interest; SHDI = Shannon diversity index.

4b5), and Dazhongling Reservoir (Figure 4c6). The transition zone is distributed around the cold island region and transitions to the heat island region, mainly near the urban greenbelt. High-temperature zones are largely concentrated in construction, population, and industrial-intensive areas, such as near the Dongguan City International Trade Center, the Global Economic and Trade Center (Figure 4a1), industrial parks (Figure 4b2), and high-density residential areas (Figure 4c3). From summer to the transition season and then to winter, the highest, lowest, and average LST decreased; in summer, the highest LST was 44.12°C, the lowest was 17.10°C, and the average was 32.56°C. The maximum and minimum LST during the transition season were not significantly different from those in summer; the maximum was 41°C, the minimum was 14.11°C, and the average decreased to 26.44°C. In winter, the highest LST was 32.13°C, the lowest was 11.07°C, and the

average was 18.6°C. In addition, the coverage of the high-temperature region also showed a downward trend from summer to winter; the proportion of the high-temperature area decreased from 35.17% to 29.25%, while the proportion of cold islands reached a maximum value of 36.5% in summer. On the contrary, the proportion of no heat island showed an upward trend.

Detection of the Spatial Heterogeneity of LST
The multi-source spatial data were processed in three steps before the GeoDetector model was used to analyze the driving factors of the spatial heterogeneity of LST. First, the influencing factors were normalized to [0,1] (Figure 5), then converted into type variables and discretized to levels 1–7. Second, the boundary of the study area was used to delineate a grid of 1×2 km, generating a total of 2887 grid points. It is noteworthy that q values differ as the classification method changes,

which raises the uncertainty of the results. Finally, several classification methods have been compared: natural break, quantile, and equal-interval. Among those, the natural break method is the optimal discretization method with the highest q values.

Impact of a Single Factor on LST Spatial Heterogeneity

The factor detector results are composed of p and q values (Table 2), which are used to measure, respectively, the significance and explanatory power of the influence of factors on LST. The p values of all factors in the summer and transition seasons were <0.004, whereas those of wind speed and landscape pattern index in winter exceeded 0.7, which indicates that the significant influence of wind speed and landscape pattern index on the spatial heterogeneity of LST decline in winter. The seasonal variation of the q value shows that the geographic factors in different seasons have varying effects on the spatial pattern of LST. In summer, the q values of NDISI, MNDWI, and Fvc exceeded 0.4, and the explanatory power for the spatial heterogeneity of LST was >40%; therefore, these three factors may be considered dominant factors. The explanatory power of socioeconomic activity and topography were second only to the dominant factors, and thus they were defined as secondary factors. In addition, the q value of wind speed was greater than those of other meteorological factors, and the q value of the COHESION index was higher than those of other landscape pattern factors. Compared with summer, the explanatory power of MNDWI during the transition season decreased, whereas that of nighttime light brightness, topography, and meteorology factors increased. In winter, the explanatory power of NDISI showed an upward trend, but other factors showed a downward trend. These results demonstrate that impervious surfaces are a key factor affecting the spatial differentiation of the thermal environment in Dongguan. We also found that compared with human-related factors, the explanatory power of natural factors on the spatial heterogeneity of LST was seasonally volatile. To better understand the explanatory power of natural and human factors on the spatial heterogeneity of LST, the q values of these factors in different seasons were added together. The total q values of natural factors in summer, the transition season, and winter were 1.606, 1.9891, and 1.282, respectively. The total q values of human-related factors were 1.8338, 1.7097, and 1.4966 in summer, the transition season, and winter, respectively. Therefore, the influence of human factors was greater

in summer and winter than that of natural factors, and weaker in the transition season.

Interaction of Factors on LST Spatial Heterogeneity

Based on the results of interaction detection (Tables 3–5), q values of the same interactive factors vary with time. Compared with the separate effects, the interactive effects of influencing factors had a more significant impact on spatial heterogeneity of LST, mainly of the Bi-enhance and Nonlinear–enhance types. Comparing the interaction detection results in different seasons, three main conclusions were drawn: First, the explanatory power of interactions between meteorological factors (X3–X6), landscape pattern factors (X13–X16), and other factors exceeded those of their separate effects. This shows that separate effects of meteorological and landscape pattern factors are not significant for LST. Instead, these two factors change the spatial heterogeneity of LST through interaction with other factors. Second, the explanatory power of interactions between NDISI (X11) and other natural factors for the spatial pattern of LST showed an increasing trend, reaching a maximum in winter. The q value of NDISI combined with those of vegetation and water bodies (X7, X8) and albedo (X12) exceeded those of interactions with other factors. Third, the q values of the interactions between topography (X1, X2), vegetation and water bodies (X7, X8), and human factors (X9–X16) were greater overall than those of interactions with other natural factors, indicating that these factors change the spatial pattern of LST by affecting the layout of human factors such as social production, population, and building density.

Detection of High LST Risk Areas

Few studies have considered the difference of LST in different intervals of the driving factors, which is important for identifying high temperature risk areas of the factors. In this study, the level of UHI was used to measure high temperature risk; these are positively correlated, and combine with the result of the risk detector to make three interesting points. First, the level of UHI decreased with increases in elevation (X1), slope (X2), CONTAG index (X13), Shannon diversity index (X14), and DIVISION index (X15). This means that the potential risks from high temperatures decrease, which means these can be defined as negative influencing factors, whereas increases in the point-of-interest density (X9), light brightness (X10), NDISI (X11), albedo (X12), and COHESION index (X16) elevate the high temperature risk, meaning

Table 2. Factor detector results.

Factor	Summer			Transition Season			Winter		
	p	q	q Order	p	q	q Order	p	q	q Order
DEM	0.000	0.1826	8	0.000	0.3372	6	0.000	0.318	2
Slope	0.000	0.2002	7	0.000	0.3540	5	0.000	0.2923	4
Temperature	0.000	0.0956	11	0.000	0.1233	9	0.000	0.1490	9
Rainfall	0.000	0.0321	16	0.000	0.0489	12	0.000	0.0183	11
Humidity	0.000	0.0476	15	0.000	0.0919	11	0.000	0.0472	10
Wind speed	0.000	0.1042	10	0.000	0.1041	10	0.727	0.0070	16
Fvc	0.000	0.4345	3	0.000	0.5614	2	0.000	0.2549	5
MNDWI	0.000	0.5092	2	0.000	0.3683	4	0.000	0.1953	7
POI	0.000	0.3727	4	0.000	0.3334	7	0.000	0.2188	6
Light intensity	0.000	0.3446	5	0.000	0.4201	3	0.000	0.3074	3
NDISI	0.000	0.5155	1	0.000	0.6280	1	0.000	0.7550	1
Albedo	0.000	0.2528	6	0.000	0.1961	8	0.000	0.1683	8
CONTAG	0.000	0.0692	14	0.002	0.0282	16	0.867	0.0116	14
SHDI	0.000	0.0867	12	0.003	0.0322	14	0.953	0.0118	13
DIVISION	0.000	0.0858	13	0.000	0.0316	15	0.938	0.0113	15
COHESION	0.000	0.1065	9	0.000	0.0401	13	0.712	0.0124	12

DEM = digital elevation model; MNDWI = improved normalized difference water index; NDISI = normalized different impervious surface index; POI = points of interest; SHDI = Shannon diversity index.

Table 3. Interaction detector results in summer (confidence level = 95%).

	X1	X2	X3	X4	X5	X6	X7	X8	X9	X10	X11	X12	X13	X14	X15	X16
X1	0.18															
X2	0.24[B]	0.20														
X3	0.22[B]	0.25[B]	0.10													
X4	0.22[N]	0.24[N]	0.13[N]	0.03												
X5	0.23[B]	0.26[N]	0.14[B]	0.07[B]	0.05											
X6	0.23[B]	0.26[B]	0.17[B]	0.12[B]	0.13[B]	0.10										
X7	0.47[B]	0.48[B]	0.49[B]	0.47[N]	0.49[N]	0.49[B]	0.43									
X8	0.54[B]	0.54[B]	0.53[B]	0.52[B]	0.52[B]	0.53[B]	0.70[B]	0.51								
X9	0.42[B]	0.43[B]	0.40[B]	0.39[B]	0.39[B]	0.40[B]	0.59[B]	0.60[B]	0.37							
X10	0.37[B]	0.38[B]	0.38[B]	0.38[B]	0.39[B]	0.38[B]	0.55[B]	0.59[B]	0.43[B]	0.34						
X11	0.54[B]	0.54[B]	0.55[B]	0.55[N]	0.56[B]	0.56[B]	0.68[B]	0.70[B]	0.62[B]	0.59[B]	0.52					
X12	0.37[B]	0.39[B]	0.32[B]	0.28[B]	0.29[B]	0.33[B]	0.68[B]	0.57[B]	0.53[B]	0.49[B]	0.64[B]	0.25				
X13	0.30[N]	0.32[N]	0.19[N]	0.11[N]	0.13[N]	0.20[N]	0.50[B]	0.59[N]	0.43[B]	0.42[N]	0.57[B]	0.31[B]	0.07			
X14	0.33[N]	0.35[N]	0.21[N]	0.13[N]	0.15[N]	0.22[N]	0.51[B]	0.61[N]	0.45[B]	0.44[N]	0.58[B]	0.33[B]	0.09[B]	0.09		
X15	0.33[N]	0.35[N]	0.21[N]	0.13[N]	0.15[N]	0.22[N]	0.51[B]	0.61[N]	0.45[B]	0.44[N]	0.58[B]	0.33[B]	0.09[B]	0.09[B]	0.09	
X16	0.37[N]	0.39[N]	0.24[N]	0.15[N]	0.18[N]	0.25[N]	0.54[B]	0.63[N]	0.46[B]	0.47[N]	0.59[B]	0.34[B]	0.11[B]	0.11[B]	0.11[B]	0.11

B = bi-enhance; N = nonlinear-enhance.

Table 4. Interaction detector results in transition season (confidence level = 95%).

	X1	X2	X3	X4	X5	X6	X7	X8	X9	X10	X11	X12	X13	X14	X15	X16
X1	0.35															
X2	0.40[B]	0.34														
X3	0.38[B]	0.37[B]	0.12													
X4	0.37[B]	0.36[B]	0.18[N]	0.05												
X5	0.39[B]	0.38[B]	0.23[N]	0.12[B]	0.09											
X6	0.37[B]	0.37[B]	0.23[N]	0.16[N]	0.18[B]	0.10										
X7	0.62[B]	0.61[B]	0.60[B]	0.58[B]	0.58[B]	0.59[B]	0.56									
X8	0.54[B]	0.52[B]	0.43[B]	0.40[B]	0.41[B]	0.42[B]	0.62[B]	0.37								
X9	0.50[B]	0.49[B]	0.40[B]	0.35[B]	0.36[B]	0.39[B]	0.61[B]	0.48[B]	0.33							
X10	0.50[B]	0.49[B]	0.46[B]	0.43[B]	0.44[B]	0.45[B]	0.63[B]	0.53[B]	0.46[B]	0.41						
X11	0.70[B]	0.70[B]	0.70[B]	0.69[B]	0.70[B]	0.70[B]	0.78[B]	0.76[B]	0.73[B]	0.73[B]	0.68					
X12	0.52[B]	0.49[B]	0.30[B]	0.25[B]	0.29[B]	0.30[B]	0.65[B]	0.51[B]	0.48[B]	0.54[B]	0.77[B]	0.20				
X13	0.43[N]	0.42[N]	0.17[N]	0.09[N]	0.13[N]	0.15[N]	0.63[N]	0.43[N]	0.38[N]	0.47[N]	0.71[N]	0.23[N]	0.03			
X14	0.44[N]	0.43[N]	0.17[N]	0.09[N]	0.14[N]	0.16[N]	0.64[N]	0.44[N]	0.38[N]	0.48[N]	0.71[B]	0.24[N]	0.04[B]	0.03		
X15	0.44[N]	0.43[N]	0.17[N]	0.09[N]	0.13[N]	0.16[N]	0.64[N]	0.44[N]	0.38[N]	0.48[N]	0.72[N]	0.24[N]	0.04[B]	0.03[B]	0.03	
X16	0.47[N]	0.47[N]	0.19[N]	0.10[N]	0.15[N]	0.18[N]	0.66[N]	0.47[N]	0.40[N]	0.51[N]	0.72[N]	0.25[N]	0.04[B]	0.04[B]	0.04[B]	0.04

B = bi-enhance; N = nonlinear–enhance.

Table 5. Interaction detector results in winter (confidence level = 95%).

	X1	X2	X3	X4	X5	X6	X7	X8	X9	X10	X11	X12	X13	X14	X15	X16
X1	0.32															
X2	0.35[B]	0.29														
X3	0.34[B]	0.33[B]	0.15													
X4	0.34[B]	0.32[N]	0.17[N]	0.02												
X5	0.34[B]	0.32[B]	0.21[N]	0.08[N]	0.05											
X6	0.34[N]	0.32[N]	0.20[N]	0.05[N]	0.07[N]	0.01										
X7	0.39[B]	0.36[B]	0.34[B]	0.29[N]	0.29[B]	0.28[N]	0.25									
X8	0.43[B]	0.40[B]	0.31[B]	0.23[N]	0.24[B]	0.22[N]	0.36[B]	0.20								
X9	0.40[B]	0.38[B]	0.32[B]	0.24[B]	0.24[B]	0.24[N]	0.36[B]	0.31[B]	0.22							
X10	0.40[B]	0.39[B]	0.37[B]	0.33[N]	0.34[B]	0.33[N]	0.38[B]	0.38[B]	0.35[B]	0.31						
X11	0.76[B]	0.76[B]	0.76[B]	0.77[B]	0.76[B]	0.76[N]	0.79[B]	0.80[B]	0.77[B]	0.76[B]	0.75					
X12	0.44[B]	0.41[B]	0.31[B]	0.20[N]	0.23[N]	0.19[N]	0.41[B]	0.31[B]	0.34[B]	0.41[B]	0.81[B]	0.17				
X13	0.36[N]	0.34[N]	0.18[N]	0.04[N]	0.07[N]	0.03[N]	0.33[N]	0.24[N]	0.25[N]	0.35[N]	0.77[N]	0.20[N]	0.01			
X14	0.37[N]	0.35[N]	0.19[N]	0.04[N]	0.07[N]	0.02[B]	0.34[N]	0.25[N]	0.25[N]	0.36[N]	0.77[N]	0.20[N]	0.02[B]	0.01		
X15	0.37[N]	0.35[N]	0.19[N]	0.04[N]	0.07[N]	0.02[N]	0.34[N]	0.26[N]	0.25[N]	0.36[N]	0.77[N]	0.20[N]	0.02[B]	0.01[B]	0.01	
X16	0.38[N]	0.37[N]	0.19[N]	0.04[N]	0.08[N]	0.03[N]	0.37[N]	0.28[N]	0.26[N]	0.37[N]	0.77[N]	0.21[N]	0.02[B]	0.02[B]	0.01[B]	0.01

B = bi-enhance; N = nonlinear–enhance.

these can be defined as positive influencing factors (Figure 6). Second, with increasing wind speed (X6), Fvc (X7), and MNDWI (X8), the risk of UHI increased and then decreased. For example, the level of FVC was in the second range when the highest temperature risk occurred, mainly located at the junction of suburbs and urban areas, which can be thus defined as potential high-temperature risk regions (Table 6). Third, there are seasonal differences in the relationship between meteorological factors (X3–X5) and heat island risk. In summer, with an

increase in rainfall, the level of UHI first increased, then decreased, then increased again, whereas it showed a positive correlation with temperature and humidity. During the transition season, with an increase in rainfall and humidity the level of UHI increased to a maximum in the first level. With an increase in temperature, the level of UHI increased and then decreased. In winter, the level of UHI first increased and then decreased with increasing rainfall and humidity, whereas it increased increasing temperature.
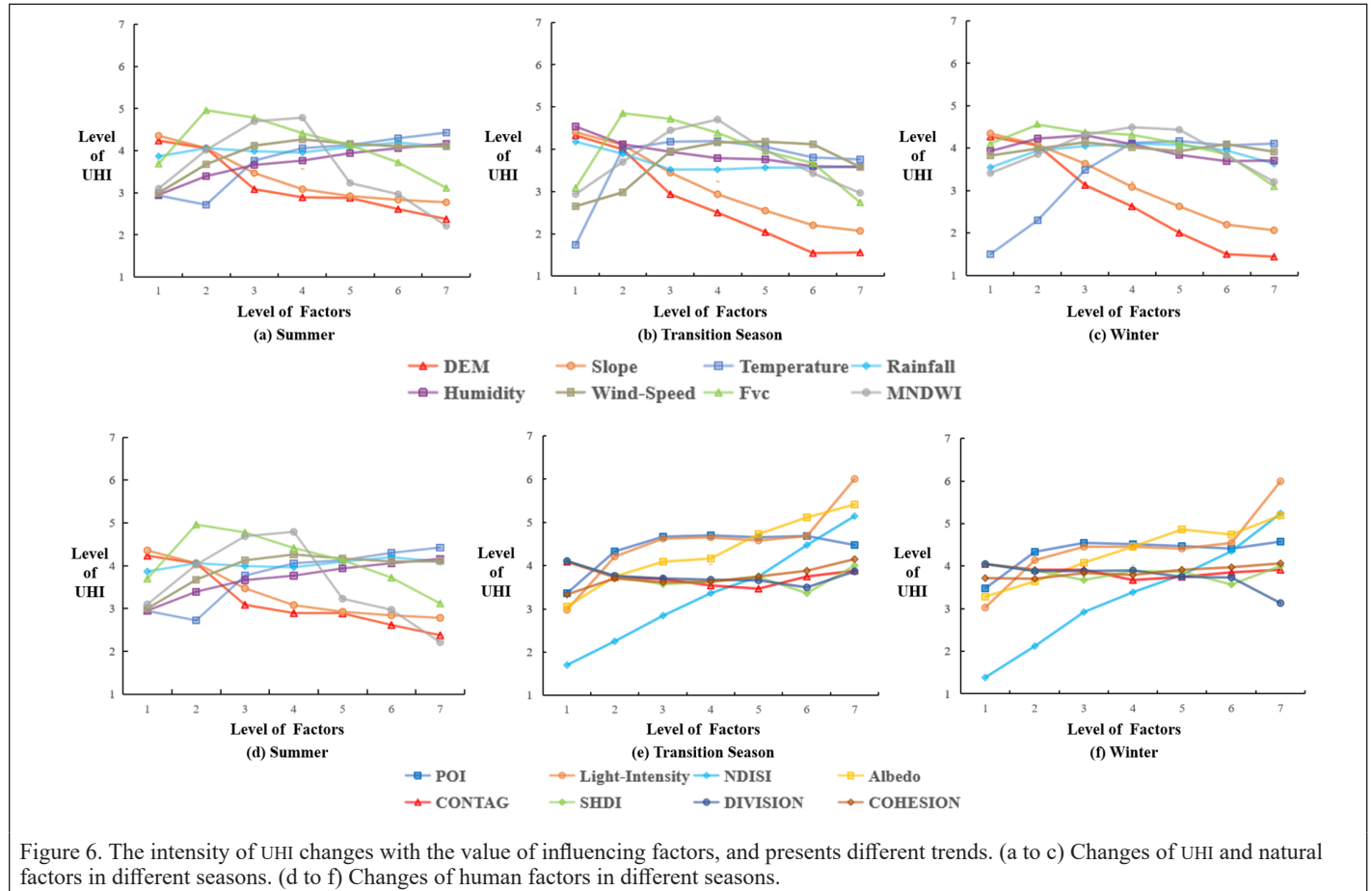
Figure 6. The intensity of UHI changes with the value of influencing factors, and presents different trends. (a to c) Changes of UHI and natural factors in different seasons. (d to f) Changes of human factors in different seasons.

Table 6. High temperature risk areas (confidence level = 95%).

Factors	Summer		Transition Season		Winter	
	Risk Areas	Average UHI	Risk Areas	Average UHI	Risk Areas	Average UHI
DEM (m)	0–56	4.23	0–56	4.33	0–56	4.27
Slope (°)	0–8.28	4.36	0–8.28	4.40	0–8.28	4.34
Temperature (°C)	29.19–31.64	4.42	20.89–21.59	4.19	17.66–19.15	4.11
Rainfall (mm)	431.33–519.88	4.20	0–22.27	4.19	31.31–39.03	4.11
Humidity (mm)	0.020–0.023	4.16	0.006–0.013	4.54	0.0074–0.0078	4.30
Wind speed (m/s)	4.80–5.60	4.26	4.94–5.62	4.19	4.30–4.89	4.14
Fvc (0–1)	0–0.66	4.96	0–0.76	4.85	0–0.79	4.56
MNDWI (−1 to 1)	−0.47 to 0.81	4.79	−0.51 to 0.58	4.70	−0.53 to 0.86	4.50
POI (number/km²)	749.93–1292.56	4.77	749.93–1292.56	4.48	749.93–1292.56	4.58
Light intensity (nW/cm²/sr)	113.51–189.14	5.50	147.07–244.69	6.00	110.35–211.07	6.00
NDISI (−1 to 1)	0.17–0.67	5.15	0.17–0.67	5.15	0.17–0.67	5.24
Albedo (0–1)	0.52–0.99	5.17	0.27–1.00	5.41	0.21–1.00	5.20
CONTAG (%)	0–55.30	4.15	0–55.30	4.09	0–55.30	4.05
SHDI (%)	0–1.58	4.18	0–1.58	4.11	0–1.58	4.05
DIVISION (%)	0–0.84	4.18	0–0.84	4.11	0–0.84	4.05
COHESION (%)	74.53–100	4.24	74.53–100	4.15	74.53–100	4.06

DEM = digital elevation model; MNDWI = improved normalized difference water index; NDISI = normalized difference impervious surface index; POI = points of interest; SHDI = Shannon diversity index.

Discussion

Impact of COVID-19 on LST

Due to the impact of COVID-19 on 18 February, Landsat-8 Operational Land Imager/Thermal Infrared Sensor images of non-COVID-19 (20 February 2021) were selected for LST inversion. The impact of COVID-19 on the spatial patterns of the LST in Dongguan was discussed by comparing the difference in LST between COVID-19 and non-COVID-19. At the global scale, the maximum, minimum, and average winter LST obtained during the non-COVID-19 period were 37.97°C, 14°C, and 23.72°C, respectively; generally, these values are higher than those for the LST during the COVID-19 winter. The urban heat island ratio index (URI) of COVID-19 (18 February 2020) and non-COVID-19 (20 February 2021) were selected to analyze the local differences; this statistic is used to quantitatively evaluate the difference of UHI effect in different years based on the ratio of UHI area to the total area of the city, so a greater URI means more intense UHIs (Xu *et al.* 2009). The influence of COVID-19 on the local LST in Dongguan was examined by calculating $\Delta URI_{2021-2020}$ during the COVID-19 and non-COVID-19 winters in each block. A $\Delta URI_{2021-2020} \leq 0$ means that the UHI during the COVID-19 period was more intense, whereas a $\Delta URI_{2021-2020} > 0$ means the UHI was weaker than during the non-COVID-19 period. Figure 7 shows $\Delta URI_{2021-2020} \leq 0$ in the towns of Gaobu, Shilong, Fenggang, Zhongtang, Qingxi, Tangxia, Machong, Shijie, Yingshi, Wangniudun, and Wanjiang. These towns are mostly located to the northwest, southwest, and northeast of Dongguan, bordering Guangzhou, Huizhou, and Shenzhen, where substantial population flow occurs. Due to the influence of COVID-19, some of the floating population returned to these areas, increasing the intensity of regional population activities and the high-temperature coverage area. Compared with winter values during COVID-19, the URI of the towns of Liaobu, Changping, Chashan, Dalang, Dalingshan, Humen, Changan, and Dongcheng increased by >0.05 during the non-COVID-19 period, alongside an expansion of the high-temperature coverage area. This may be related to the return to normal life and production following the pandemic, characterized by an increased intensity of human activity.
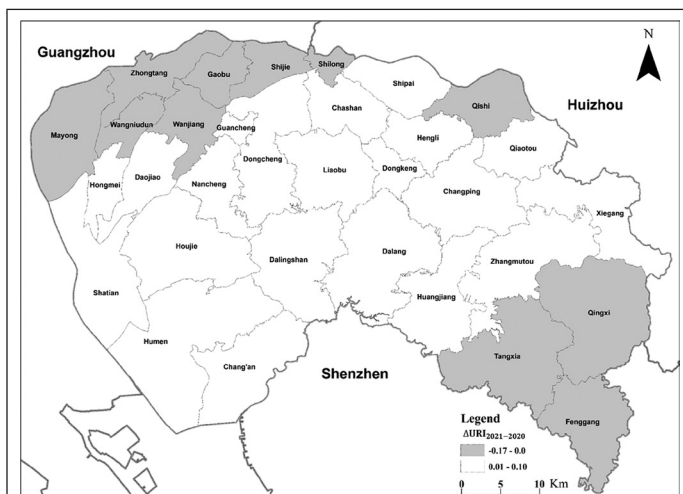
Figure 7. The map of winter URI for COVID-19 and non-COVID-19. The quantity $\Delta URI_{2021-2020}$ is the URI index difference between non-COVID-19 and COVID-19, which is used to explore the influence of COVID-19 on the local LST in Dongguan City. A $\Delta URI_{2021-2020} \leq 0$ means the UHI during COVID-19 was more intense than during the non-COVID-19 year; a $\Delta URI_{2021-2020} > 0$ means it was weaker. LST = land surface temperature; URI = urban heat island ratio index.

Influence of Dominant Factors on LST Spatial Heterogeneity

Shao *et al.* (2020), discussing the relationship between urbanization and the ecological environment in the Yangtze River Delta, observe that built-up and coastal areas with low vegetation coverage and intense human activities experience a significant UHI. There is therefore a need to determine the relationship between the spatial heterogeneity of LST and the spatial patterns of impervious surfaces and the *FVC*. This section primarily discusses this relationship based on the analysis results of the GeoDetector. First, the q value of the NDISI was >0.5 in different seasons, which means that the NDISI is a positive dominant factor of UHI. During urbanization, artificial surfaces replace natural surfaces, increasing the area of impervious surface. Ultimately, this alters the form of the underlying urban surface, affecting the urban thermal environment and increasing the ground temperature. Second, the q value of the Fvc initially increased then decreased from summer to winter; the highest (0.56) occurred during the transitional season, and the lowest (0.25) in winter. This is closely related to the climate type and biological phenology of Dongguan. The growth of vegetation branches and leaves peaks in summer and autumn, imposing a strong alleviation effect on the high-temperature phenomenon. Finally, these dominant factors do not affect the spatial heterogeneity of LST in isolation. By neglecting the interaction of these factors, it is easy to ignore the impact of minor factors with lower explanatory power on the spatial pattern of LST, such as meteorology and landscape patterns. Although these factors often do not directly affect the LST, they alter its distribution pattern by influencing socioeconomic activities, surface morphology, and other factors.

Conclusion

Dongguan represents a typical city experiencing rapid urbanization in China, and SUHIs have become a major problem. This study used the GeoDetector model to analyze the impact of the geographic environment on the spatial heterogeneity of LST based on 16 influencing factors in six dimensions, and the results highlighted three key findings and contributions: First, by comparing the differences in URI between COVID-19 and non-COVID-19 periods, it was possible to analyze the impact of the movement restriction policies during the pandemic on the UHI intensity in local areas of Dongguan. LST during the winter of COVID-19 was generally lower than during normal days (i.e., the non-COVID-19 period), although some areas with   were mainly distributed in the border areas of Guangzhou, Huizhou, and Shenzhen. Second, the results of the GeoDetector model showed that the interaction of driving factors had greater explanatory force as to the spatial heterogeneity of LST than did the individual effects of each factor. Third, this research demonstrates that the GeoDetector is suitable for related research on surface temperature. It was able to detect dominant factors affecting the spatial heterogeneity of LST, analyze the interaction effects of these factors, and identify areas at risk of high temperatures.

Although this research fulfilled a range of outcomes, it also has shortcomings. First, LST inversion was mainly derived from Landsat data; future research should attempt to combine multi-source surface temperature data and deep-learning methods to improve the accuracy of LST inversion. Second, this study did not consider the modifiable areal unit problem; future research should consider the impact of scale effects on the spatial heterogeneity of LST. This enables a comprehensive analysis of the formation and evolution mechanisms underpinning the spatial heterogeneity of urban surface temperatures.

References

Baldinelli, G. and S. Bonafoni. 2015. Analysis of albedo influence on surface urban heat island by spaceborne detection and airborne thermography. Pages 95–102 in *International Conference on Image Analysis and Processing*, held in Genoa, Italy, 7–8 September 2015. Edited by V. Murnio, E. Puppo, D. Sona, M. Cristani and C. Sansone. Lecture Notes in Computer Science vol. 9281. Cham, Switzerland: Springer.

Chen, W., Y. Zhang, C. Pengwang and W. Gao. 2017. Evaluation of urbanization dynamics and its impacts on surface heat islands: A case study of Beijing, China. *Remote Sensing* 9(5):453.

Deilami, K. and M. Kamruzzaman. 2017. Modelling the urban heat island effect of smart growth policy scenarios in Brisbane. *Land Use Policy* 64:38–55.

Eludoyin, O. M., I. O. Adelekan, R. Webster and A. O. Eludoyin. 2014. Air temperature, relative humidity, climate regionalization and thermal comfort of Nigeria. *International Journal of Climatology* 34(6):2000–2018.

Faroughi, M., M. Karimimoshaver, F. Aram, E. Solgi, A. Mosavi, N. Nabipour and K.-W. Chau. 2020. Computational modeling of land surface temperature using remote sensing data to investigate the spatial arrangement of buildings and energy consumption relationship. *Engineering Applications of Computational Fluid Mechanics* 14(1):254–270.

Hua, L., X. Zhang, Q. Nie, F. Sun and L. Tang. 2020. The impacts of the expansion of urban impervious surfaces on urban heat islands in a coastal city in China. *Sustainability* 12(2):475.

Huang, X., A. Schneider and M. A. Friedl. 2016. Mapping sub-pixel urban expansion in China using MODIS and DMSP/OLS nighttime lights. *Remote Sensing of Environment* 175:92–108.

Li, X., W. Guo, S. Li, J. Zhang and X. Ni. 2021. The different impacts of the daytime and nighttime land surface temperatures on the alpine grassland phenology. *Ecosphere* 12(6):e03578.

Li, Y., Y. Sun, J. Li and C. Gao. 2020. Socioeconomic drivers of urban heat island effect: Empirical evidence from major Chinese cities. *Sustainable Cities and Society* 63:102425.

Liang, S. 2001. Narrowband to broadband conversions of land surface albedo I: Algorithms. *Remote Sensing of Environment* 76(2):213–238.

Liang, X. and Y. Li. 2018. Spatio-temporal features of scaling farmland and its corresponding driving mechanism in Three Gorges Reservoir Area. *Acta Geographic Sinica* 73(9):1630–1646.

Liu, F., H. Hou and Y. Murayama. 2021. Spatial interconnections of land surface temperatures with land cover/use: A case study of Tokyo. *Remote Sensing* 13(4):610.

Liu, T., Z. Wang, X. Huang, L. Cao, M. Niu and Z. Tian. 2015. An effective Antarctic ice surface temperature retrieval method for MODIS. *Photogrammetric Engineering and Remote Sensing* 81(11):861–872.

Liu, Y., H. Li, P. Gao and C. Zhong. 2021. Monitoring the spatiotemporal dynamics of urban green space and its impacts on thermal environment in Shenzhen city from 1978 to 2018 with remote sensing data. *Photogrammetric Engineering and Remote Sensing* 87(2):81–89.

Mirzaei, M., J. Verrelst, M. Arbabi, Z. Shaklabadi and M. Lotfizadeh. 2020. Urban heat island monitoring and impacts on citizen's general health status in Isfahan metropolis: A remote sensing and field survey approach. *Remote Sensing* 12(8):1350.

Peng, J., J. Jia, Y. Liu, H. Li and J. Wu. 2018. Seasonal contrast of the dominant factors for spatial distribution of land surface temperature in urban areas. *Remote Sensing of Environment* 215:255–267.

Shao, Z., L. Ding, D. Li, O. Altan, M. E. Huq and C. Li. 2020. Exploring the relationship between urbanization and ecological environment using remote sensing images and statistical data: A case study in the Yangtze River Delta, China. *Sustainability* 12(14):5620.

Sobrino, J. A., J. C. Jiménez-Muñoz and L. Paolini. 2004. Land surface temperature retrieval from LANDSAT TM 5. *Remote Sensing of Environment* 90(4):434–440.

Van der Linden, S., A. Rabe, M. Held, B. Jakimow, P. J. Leitão, A. Okujeni, M. Schwieder, S. Suess and P. Hostert. 2015. The EnMAP-Box—A toolbox and application programming interface for EnMAP data processing. *Remote Sensing* 7(9):11249–11266.

Wang, J.-F. and Y. Hu. 2012. Environmental health risk detection with GeogDetector. *Environmental Modelling & Software* 33:114–115.

Wang, K. and S. Liang. 2009. Evaluation of ASTER and MODIS land surface temperature and emissivity products using long-term surface longwave radiation observations at SURFRAD sites. *Remote Sensing of Environment* 113(7):1556–1565.

Wang, Y., G. Yi, X. Zhou, T. Zhang, X. Bie, J. Li and B. Ji. 2021. Spatial distribution and influencing factors on urban land surface temperature of twelve megacities in China from 2000 to 2017. *Ecological Indicators* 125:107533.

Xiong, Y. and F. Zhang. 2021. Effect of human settlements on urban thermal environment and factor analysis based on multi-source data: A case study of Changsha city. *Journal of Geographical Sciences* 31(6):819–838.

Xu, H-Q. 2005. A study on information extraction of water body with the modified normalized difference water index (MNDWI). *Journal of Remote Sensing* 5:589–595.

Xu, H. 2010. Analysis of impervious surface and its impact on urban heat environment using the normalized difference impervious surface index (NDISI). *Photogrammetric Engineering and Remote Sensing* 76(5):557–565.

Xu, H., F. Ding and X. Wen. 2009. Urban expansion and heat island dynamics in the Quanzhou region, China. *IEEE Journal of Selected Topics in Applied Earth Observations and Remote Sensing* 2(2):74–79.

Yang, S.-W., B. Dong, L. Liu, L. Sun, S.-W. Sheng, Q. Wang, W. Peng, X. Wang, Z. Zhang and J. Zhao. 2015. Research on vegetation coverage change in Sheng Jin Lake wetland of Anhui Province. *Wetlands* 35(4):677–682.

Zhao, X., J. Liu and Y. Bu. 2021. Quantitative analysis of spatial heterogeneity and driving forces of the thermal environment in urban built-up areas: A case study in Xi'an, China. *Sustainability* 13(4):1870.

Zhou, W., J. Wang and M. L. Cadenasso. 2017. Effects of the spatial configuration of trees on urban heat mitigation: A comparative study. *Remote Sensing of Environment* 195:1–12.

Zhu, L., J. Meng and L. Zhu. 2020. Applying Geodetector to disentangle the contributions of natural and anthropogenic factors to NDVI variations in the middle reaches of the Heihe River Basin. *Ecological Indicators* 117:106545.

Urban Land Cover/Use Mapping and Change Detection Analysis Using Multi-Temporal Landsat OLI with Lidar-DEM and Derived TPI

Clement E. Akumu and Sam Dennis

Abstract

The mapping and change detection of land cover and land use are essential for urban management. The aim of this study was to map and monitor the spatial and temporal change in urban land cover and land use in Davidson County, Tennessee in the periods of 2013, 2016, and 2020. The urban land cover and land use categories were classified and mapped using Random Forest algorithm. A combination of Landsat Operational Land Imager (OLI) satellite data with Light Detection and Ranging (lidar)-Digital Elevation Model (DEM) and derived Topographic Position Index (TPI) were used in the classification and monitoring of urban land cover and land use change. The urban land cover and land use types were mapped with average overall accuracies of about 87% in 2020, 85% in 2016 and 2013. The overall accuracy increased by around 8%, 9%, and 6% in 2020, 2016, and 2013 classifications respectively when lidar-DEM and derived TPI were added to Landsat OLI satellite data in the classification relative to standalone Landsat OLI. Total change occurred in about 63% of Davidson County between 2016 and 2020 with significant net gains and losses among land cover and land use types. This information could support land use planning.

Introduction

Land cover change is defined in this study as any change in the land biophysical characteristics including but not limited to vegetation and soil properties, whereas land use change is associated with the alteration of land by humans. Urban land use change is generally driven by urban growth, and this can lead to loss of natural vegetation and open space, a decline in connectivity of wetlands and wildlife habitats, and a loss in biodiversity (Patel et al. 2019; Verma et al. 2020). The understanding of urban land cover and land use change can provide insights on the impacts of land management practices and feedback to the environment to better manage land resources. Furthermore, it helps to quantitatively project future change in urban land cover to support land use management and planning. A change in land cover and land use category alters land biophysical surface characteristics and this can lead to significant consequences including but not limited to land degradation, water pollution, expedition of climate change, and changes to ecosystem services (Foley et al. 2005; Homer et al. 2020; Pielke 2005).

The Davidson County constitutes the largest city of Nashville in Tennessee and has experienced significant growth in population over the years with a population of around 477 800 in 1980 to approximately 678 889 in 2015 (Mojica 2018; United States Census Bureau 2018). The population growth in Davidson County is expected to influence land cover and land use change. Therefore, there is a need to spatially and explicitly detect and monitor the land cover and land use change in Davidson County to support urban planning and management. The use of multi-source and temporal data such as Landsat Operational Land Imager

(OLI) in combination with Light Detection and Ranging (lidar)-Digital Elevation Model (DEM) and derived Topographic Position Index (TPI) could improve the detection, monitoring and change detection analysis of urban land cover and land use classification. This is because land cover and land use types respond to electromagnetic radiation differently and their spectral information is useful to map and monitor spatial and temporal change in land cover categories. A TPI is simply the difference between a cell elevation value and the average elevation of the neighborhood around that cell (Weiss 2001). The positive values of TPI mean the cell is higher than its surroundings, whereas negative values mean it is lower than its surroundings. TPI values near zero imply flat areas where the slope is near zero or mid-slope areas (Jenness 2013). The integration of topographic variables such as lidar-DEM and TPI could improve detection and change analysis because land cover and land use change generally occurs along topographic gradients (Birhane *et al.* 2019; Liu *et al.* 2020).

Several classification methods, including but not limited to deep learning and machine learning, have been recently used in land cover mapping and change detection analysis (Bai *et al.* 2021; Sefrin *et al.* 2021; Shao *et al.* 2014; Yao *et al.* 2021; Zhao *et al.* 2017; Zhong *et al.* 2021). For example, Sefrin *et al.* (2021) used fully convolutional neural network independently and combined with long short-term memory networks to distinguish land cover changes and misclassifications of deep learning approaches. They found that the multi-temporal sequential information used when fully convolutional neural network was combined with long short-term memory networks outperformed the mono-temporal fully convolutional neural network approach in landcover change detection mapping. Furthermore, Zhao *et al.* (2017) integrated object-based classification with deep learning to improve urban land cover classification. Shao *et al.* (2014) used a machine learning hierarchical semi-supervised support vector machine algorithm to classify landcover in hyperspectral images. They found improved accuracy in landcover detection using hierarchical semi supervised support vector machine technique relative to Kernel fuzzy C-means approach. In addition, Yao *et al.* (2021) explored continuous multi-angle remote sensing data relative to single angle in land cover and use classification. They found improved land cover classification accuracy using continuous multi-angle relative to single angle remote sensing data.

Recent study in Connecticut, United States examined land cover and land use change from 1985 and 2015 using Landsat-derived 30 m land cover maps (Arnold *et al.* 2020). They found a 4.7% increase in development related land covers and corresponding losses to forest and agricultural land. Furthermore, Homer *et al.* (2020) analyzed land cover change patterns from 2001 to 2016 in the Conterminous United States using Landsat series satellite data and ancillary data included but not limited to the National Land Cover Database, DEM, and derivatives such as slope and aspect. They found significant change in the Conterminous United States landscape with about 50% of forest loss. Agriculture areas increased slightly during the study period but there

---

Department of Agricultural and Environmental Sciences, College of Agriculture, Tennessee State University, Nashville, Tennessee (aclemen1@tnstate.edu).

was a substantial decline (≈8%) in pasture/hay. Furthermore, they found developed areas increased by about 6% with southern states exhibiting most of the developmental expansion. Although these studies captured important changes in land cover and land use in the United States, their analyses of recent changes were limited to years of 2015 and 2016. This study presents analyses of recent urban land cover and land use change in Davidson County, Tennessee, United States for the periods of 2020, 2016, and 2013 using a combination of Landsat OLI satellite data with lidar-DEM and derived TPI. It aims to map and monitor the spatial and temporal change in urban land cover and land use categories within these periods. This information could be useful to urban planners and policy makers to support land cover and land use planning and management.

Materials and Methods

Study Area

The study area of Davidson County consists of the city Nashville and surrounding suburbs. The area ranges from latitude 35°58'15" to 36°22'49" N and longitude 86°36'45" to 86°54'43"W (Figure 1). Davidson County is the second largest in Tennessee and among the rapid growing counties in the United States (Sellers 2018; United States Census Bureau 2018). The rapid growing urban population will likely cause significant change to the environment because of increased pressure on ecosystem services and resources.

Climate

The region experiences modest climate with cool winters and warm summers (Hodges *et al.* 2018). The mean annual temperature of Davidson County is approximately 78°F (26°C) in the summer and around 41°F (5°C) in the winter. The annual precipitation is about 51 inches (1300 mm) and generally distributed homogeneously throughout the seasons (Hodges *et al.* 2018). The month of May generally experiences the maximum monthly average precipitation of about 5.51 inches, whereas the month of October experiences the minimum monthly average rainfall of around 3.03 inches (United States Climate Data 2018).

Geology and Hydrology

The study area consists of a variety of gentle and highland terrains (Hodges *et al.* 2018). Alkaline soils are generally found around the central basin, whereas acidic soils occur on the highlands (Mitsch *et al.* 2009). The gentle and highland terrains are occasionally cut across by major rivers such as the Cumberland River that flows southwards in the county (Mitsch *et al.* 2009). Several reservoirs have been constructed around the Cumberland River to manage flooding during high periods of rainfall. Several streams in the area have also been re-directed to support agricultural activities (Meador 1996).

Methodology

The methodological approach mainly involved the temporal classification and mapping or urban land cover and land use categories in Davidson County, Tennessee using Landsat OLI satellite data acquired in the years 2020, 2016, and 2013 with lidar-DEM and derived TPI (Figure 2). The Landsat OLI and lidar-DEM data were preprocessed, integrated, and used in the classification and monitoring of urban land cover and land use classes (Figure 2). Classification accuracy assessments were conducted, and the generated urban land cover and land use maps were exported as raster files to Geographic Information System (GIS) for change detection analyses. The assessment of temporal and spatial change in urban land cover and land use classes was carried out using post-classification comparison technique. The detection of areas where change occurred and areas where no change occurred in Davidson County was performed using image differencing technique.

Landsat OLI satellite scenes acquired in the months of August 2020, June 2016, and September 2013 respectively were downloaded from the United States Geological Society (USGS) Science Data repository. The images were selected because they had zero percent of cloud cover. Five major remote sensing image processing phases', i.e., preprocessing, data integration, classification, accuracy assessments/validations, and change detection (Figure 2) were used to map and monitor
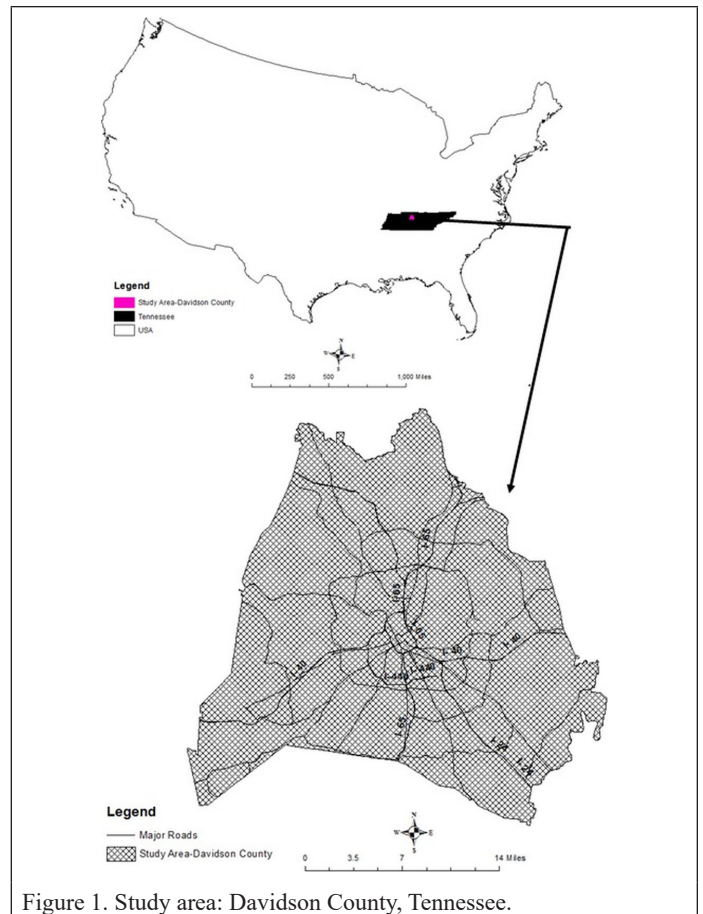

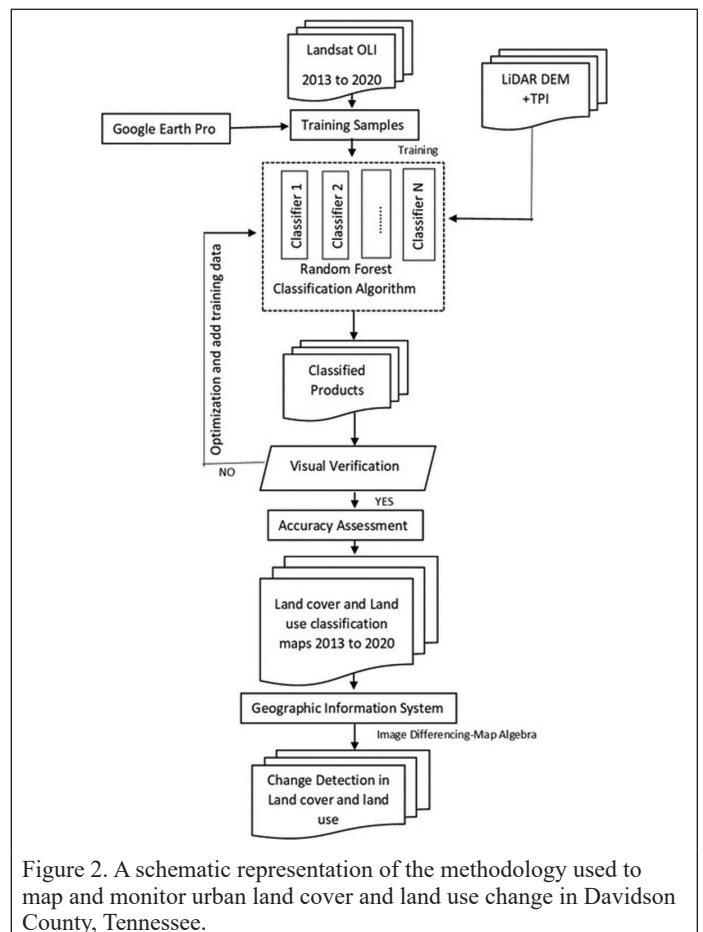Figure 1. Study area: Davidson County, Tennessee.

Figure 2. A schematic representation of the methodology used to map and monitor urban land cover and land use change in Davidson County, Tennessee.

the urban land cover and land use classes. The Landsat OLI satellite images were subsetted to the study area, georeferenced, co-registered, and calibrated radiometrically in the preprocessing stage. The geometric calibration was performed using greater than 50 ground control points and a root-mean-square (RMS) value of less than 1 pixel. The radiometric calibration involved the transformation of digital numbers (DN) to spectral reflectance.

The Landsat OLI scenes were converted from digital numbers to at-surface reflectance by using reflectance rescaling coefficients (Equation 1) derived from National Aeronautics and Space Administration (2018).

$$\rho\lambda' = MpQcal + Ap \quad (1)$$

where

$\rho\lambda'$ = top of atmosphere (TOA) planetary reflectance without correction for solar angle; Mp = band-specific multiplicative rescaling factor (Reflectance_Mult_Band_x, where x is the band number); Ap = band-specific additive rescaling factor (Reflectance_Add_Band_x where x is the band number); and Qcal = digital numbers.

The band-specific multiplicative rescaling factor (Reflectance_Mult_Band_x), and additive rescaling factor (Reflectance_Add_Band_x) were obtained in the header file of the imagery.

Furthermore, the correction of TOA planetary reflectance for sun angle was performed using Equation 2 (National Aeronautics and Space Administration 2018).

$$\rho\lambda = \rho\lambda' / \sin(\theta SE) \quad (2)$$

where $\rho\lambda$ = TOA planetary reflectance corrected for sun angle; $\rho\lambda'$ = TOA planetary reflectance without correction for solar angle; and θSE = local sun elevation angle in degrees provided in the metadata (Sun_Elevation).

The spectral reflectance Landsat OLI scenes were integrated with 30 m lidar-DEM and derived TPI images. The 30 m lidar-DEM was filled and used to generate TPI. The TPI was computed using Equation 3 (Weiss 2001).

TPI < scalefactor <= int (dem – focalmean(dem, annulus, irad, orad)) +0.5 (3)

where scalefactor = outer radius in map units; irad = inner radius of annulus in cells; and orad = outer radius of annulus in cells.

The TPI was derived using 500 m radius and 1000 m radius neighborhood window sizes. Both the TPI and lidar-DEM were added independently as separate bands with the reflectance Landsat OLI satellite data in the mapping and monitoring of urban land cover and land use classes.

Supervised classification was carried out using standalone Landsat OLI satellite data and in combination with lidar-DEM and derived TPI. The urban land cover and land use training classes were visually detected in Google Earth Pro version 7.3.3.7786 and polygons were digitized around the training classes. The polygons were later exported as Keyhole Markup Language files and converted to shape files in GIS environment. The urban land cover and land use polygons constituted the training data used to classify and map the urban land cover and land use categories. There were 320 polygons (training) data used in the classification and were randomly distributed throughout the study area. The training data for each land cover and land use class used in the supervised classification had at least 500 pixels. The classification was performed using a machine-learning Random Forest classification algorithm. The Random Forest classification algorithm is an ensemble classification algorithm that produces multiple decision trees using a randomly selected subset of training samples and variables (Belgiu and Dragut 2016). It is expressed using Equation 4 (Breiman 2001).

$$\{DT(x,\theta_k)_{k=1}^T \quad (4)$$

where x is the input vector, and θ_k represents a random vector, which is sampled independently but with the same distribution as the previous $\theta_k, \ldots, \theta_{k-1}$. T bootstrap samples are initially derived from the training data. A no-pruned classification and regression tree (CART) is drawn from each bootstrap sample β where only one of M randomly selected

feature is chosen for the split at each node of CART (Breiman 2001; Magidi *et al.* 2021).

Each of the decision tree casts a unit vote for the most popular class to classify an input vector (Breiman 1999).The number of features used at each node to generate a tree and the number of trees to be grown are two user-defined parameters that are required to generate a random forest classifier. The Random Forest classification model was controlled for overfitting by performing five-fold cross-validation repeated twice on the training data. In the cross-validation process, about 25% of the training data were kept aside as a test-data set, while the remaining 75% training data set was divided into five equal sets and used in the five-fold cross validation. The first set was kept as the hold out (testing) set and the remaining $k – 1$ sets were used to train the Random Forest classification prediction of urban land cover and land use classes. The five-fold cross-validation was performed with a changing hold out (testing) set. The mean accuracy of the land cover and land use classification generated from the five-fold cross-validation process was estimated. The training data was then used to classify the urban land cover and land use categories and the kept aside 25% test-data set was used to validate the classification. The test-data set and the training data set accuracies were then evaluated (Costa *et al.* 2018; Elmaz *et al.* 2020; Sharma *et al.* 2017). Furthermore, the number of trees and training samples in the Random Forest classification prediction model were selected through a resampling-based procedure to search for optimal tuning parameters. The optimal settings were selected based on the mean overall accuracy across five-fold cross validation, repeated twice (Costa *et al.* 2018; Sharma *et al.* 2017). The default number of training samples was set at 5000 and the number of trees was set at 10. The visible and infrared spectral reflectance bands in combination with lidar-DEM and derived TPI were used in the supervised classification. The urban land cover and land use maps generated for the years 2020, 2016, and 2013 were validated to examine how well the classified maps represented the various land cover and land use categories on the ground. The validation/accuracy assessment was conducted by randomly selecting about 1200 polygons from each classified land cover and land use map and comparing them to Google Earth Pro information representing land cover and land use classes on the ground. The validation data (1200 polygons) was distinct from the training data (320 polygons) used in the Random Forest classification of urban land cover and land use categories. The 1200 polygons were randomly distributed throughout the area of study. Furthermore, site visitations were also carried out to compare polygons on the classified maps to land cover information on the ground.

The overall classification accuracy was computed for each classified urban land cover and land use map by dividing the total correct (i.e., the sum of the major diagonal in the error matrix table) by the total number of pixels in the error matrix table (Mather and Koch 2011). The producer's accuracy was calculated by dividing the number of correctly identified in reference plots of a given class by the number actually in that reference class (Mather and Koch 2011). The user's accuracy was computed by dividing the number correctly identified of a given class by number claimed to be in that map class (Mather and Koch 2011).

The kappa coefficient was computed using Equation 5 (Mather and Koch 2011).

$$\frac{N\sum_{i=1}^{r} X_{ii} - \sum_{i=1}^{r}(X_{i+} \times X_{+i})}{N^2 - \sum_{i=1}^{r}(X_{i+} \times X_{+i})} \quad (5)$$

where r = number of rows, columns in the error matrix; N = number of observations (pixels) in the error matrix; X_{ii} = major diagonal element for class i; X_{i+} = total number of observations in row i (right margin); and X_{+i} = total number of observations in column i (bottom margin).

The urban land cover and land use classification maps were later exported into GIS for change detection analyses. Post classification comparison change detection approach was carried out between the generated urban land cover and land use categories. The detection of

areas where change occurred and areas where no change occurred was performed through image differencing in ArcGIS version 10.4.1. The image difference tool in Spatial Analyst was used to detect areas where change occurred and areas where no change occurred in the years 2020, 2016, and 2013. The image difference tool assigns the land cover and land use category values to the most recent image where change occurred and assigns a value of zero to the image where no change occurred (Environmental Systems Research Institute 2021). Furthermore, the classified maps were overlaid, and their attributes' tables were exported into Microsoft Excel to develop a transition matrix table of change progression among land cover and land use classes.

Results and Discussion

Urban Land Cover and Land Use Distribution

The classified urban land cover and land use classes included agriculture, bareland, developed/built-up, forest, grassland, shrubland, water, and wetland (Figures 3–5). The classes were distributed throughout Davidson County in the years 2020, 2016, and 2013. Developed/built-up areas occurred mostly in the central part of the county with the city Nashville. The major open water called the Cumberland River was found to cut across the county with agriculture areas distributed around the major river and streams. This is because agricultural activities require water for irrigation and farmers prefer close access to water for irrigation. The wetland, bareland, and grassland were sparsely distributed in the study area relative to agriculture, developed/built-up, forest, and shrubland in the years 2020, 2016, and 2013. The construction and expansion of wetlands in the study area will be valuable to provide habitats to a variety of species and regulate pollution and hydrological processes (Cohen *et al.* 2016). Although forest occupied a significant part of the study area, it was concentrated in the western portion of the region relative to the eastern section in the years 2020, 2016, and 2013 (Figures 3–5).
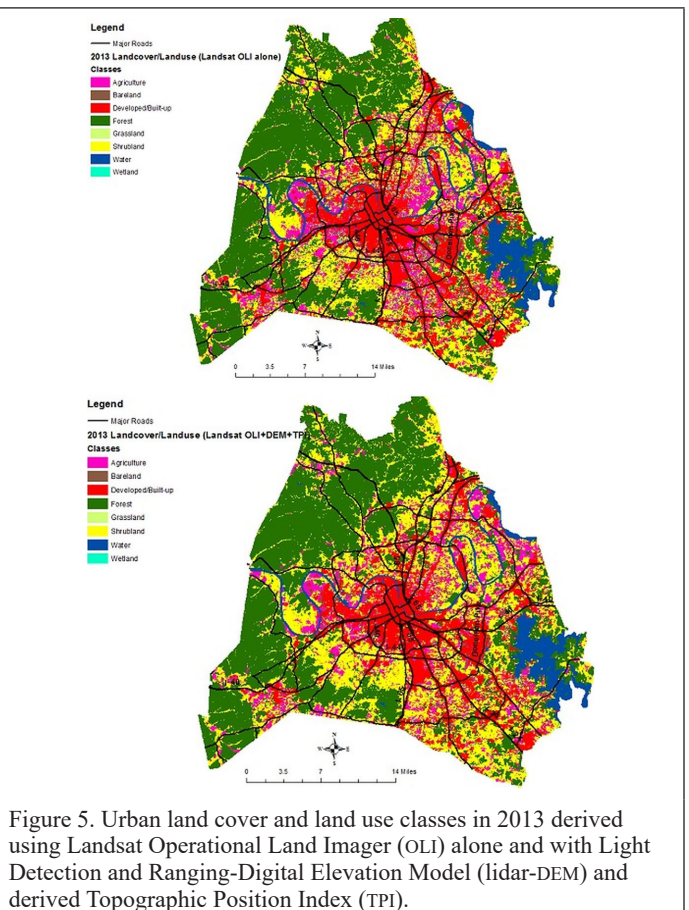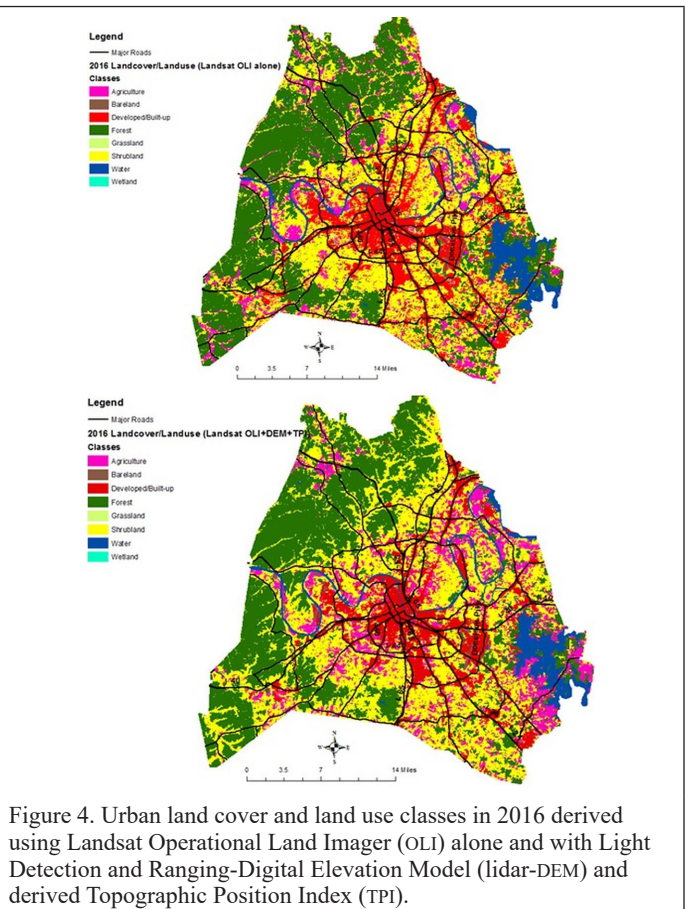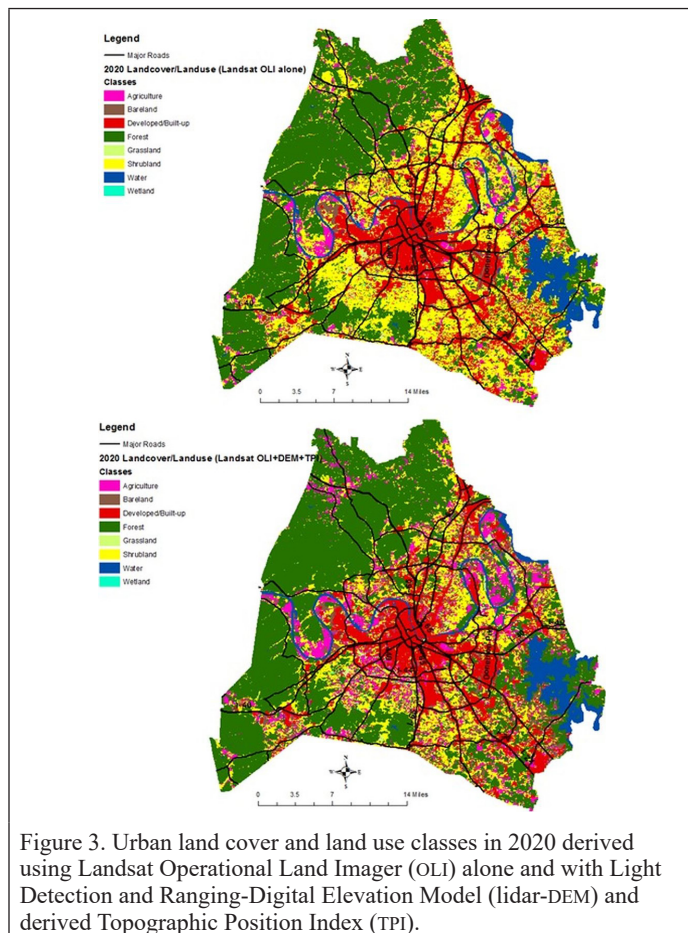
Figure 4. Urban land cover and land use classes in 2016 derived using Landsat Operational Land Imager (OLI) alone and with Light Detection and Ranging-Digital Elevation Model (lidar-DEM) and derived Topographic Position Index (TPI).

Figure 3. Urban land cover and land use classes in 2020 derived using Landsat Operational Land Imager (OLI) alone and with Light Detection and Ranging-Digital Elevation Model (lidar-DEM) and derived Topographic Position Index (TPI).

Figure 5. Urban land cover and land use classes in 2013 derived using Landsat Operational Land Imager (OLI) alone and with Light Detection and Ranging-Digital Elevation Model (lidar-DEM) and derived Topographic Position Index (TPI).

The area covered by forest and wetland was about 40 003 ha and 545 ha, respectively, in 2013 when standalone Landsat OLI satellite data was used to classify and map the urban land cover and land use types (Table 1). The area covered by forest and wetland increased to around 41 480 ha and 817 ha, respectively, in 2013 when Landsat OLI satellite data was integrated with lidar-DEM and derived TPI in the classification (Table 1). Similarly, in the year 2016 the area covered by forest and wetland was approximately 36 818 ha and 196 ha, respectively, when Landsat OLI satellite data was used alone to classify and map the urban land cover and land use categories. The area covered by forest and wetland increased to about 37 689 ha and 592 ha, respectively, in 2016 when Landsat OLI satellite data was combined with lidar-DEM and derived TPI in the classification (Table 1). Likewise, in the year 2020, the area covered by forest and wetland was around 39 491 ha and 605 ha, respectively, when standalone Landsat OLI satellite data was used to classify and map urban land cover and land use types. The area covered by forest and wetland increased to about 40 389 ha and 804 ha, respectively, in 2020 when Landsat OLI satellite data was integrated with lidar-DEM and derived TPI in the classification (Table 1). This implies elevation and topographic position are likely contributing factors in the detection of wetland and forest areas in urban environments.

The percent cover of land cover and land use types varied among classes, classification methods and years of satellite data acquisition (Figure 6). For example, when Landsat OLI satellite data alone was used in the classification of urban land cover and land use types, forest had the highest percent cover (29%), whereas wetland had the lowest percent cover (0.4%) in the year 2013. Similarly, when Landsat OLI satellite data was integrated with lidar-DEM and derived TPI in the classification, forest had the maximum percent cover of about 31%,

whereas wetland had the minimum percent cover of about 0.6% in 2013 (Figure 6). In the year 2016, shrubland had the most percent cover of around 31%, whereas wetland had the least percent cover of about 0.1% when standalone Landsat OLI satellite data was used in the classification. Likewise, in the year 2016, shrubland had the maximum percent cover of approximately 30%, whereas wetland had the minimum percent cover of about 0.4% when lidar-DEM and derived TPI were added to Landsat OLI satellite data in the classification (Figure 6). The percent cover was also highest for shrubland (29%) and lowest for wetland (0.4%) in the year 2020 when standalone Landsat OLI satellite data was used in the classification of urban land cover and land use types. However, when Landsat OLI satellite data was combined with lidar-DEM and derived TPI, the percent cover was maximum for forest (30%) and minimum for wetland (0.6%) in the year 2020 (Figure 6). The high amount of forest cover detected in the study area will contribute to climate change mitigation through carbon sequestration (Bellassen and Luyssaert 2014; Buotte *et al.* 2019; Favero *et al.* 2020).

Accuracy Assessments of Urban Land Cover and Land Use Classifications

The urban land cover and land use classifications were successfully performed with average overall accuracies of about 87% in 2020, and 85% in 2016 and 2013 (Tables 2–4). When Landsat OLI was integrated with lidar-DEM and derived TPI in the 2020 classification, the overall accuracy increased by around 8% relative to Landsat OLI satellite data alone. Similarly, when lidar-DEM and derived TPI were added to Landsat OLI in the 2016 and 2013 classifications, the overall accuracies increased by approximately 9% and 6%, respectively, relative to Landsat OLI alone. This implies topographic attributes such as DEM and TPI were likely important variables in improving the urban land cover and land use classification.

Table 1. Urban land cover and land use areas (in hectares) in the years 2020, 2016, and 2013 derived using Landsat Operational Land Imager (OLI) alone and in combination with Light Detection and Ranging-Digital Elevation Model (lidar-DEM) and derived Topographic Position Index (TPI).

Urban Land Cover and Land Use Classes	2013 Landsat OLI with DEM and TPI	2013 Landsat OLI Alone	2016 Landsat OLI with DEM and TPI	2016 Landsat OLI Alone	2020 Landsat OLI with DEM and TPI	2020 Landsat OLI Alone
Agriculture	23 599	25 607	26 380	27 786	21 866	20 629
Bareland	4585	4864	2841	3383	5678	5821
Developed/Built-up	18 655	17 729	18 670	17 974	19 090	19 571
Forest	41 480	40 003	37 689	36 818	40 389	39 491
Grassland	1365	1346	2102	1944	3090	3225
Shrubland	39 531	39 853	41 280	42 062	38 825	39 749
Water	5976	6061	6454	5845	6266	6917
Wetland	817	545	592	196	804	605
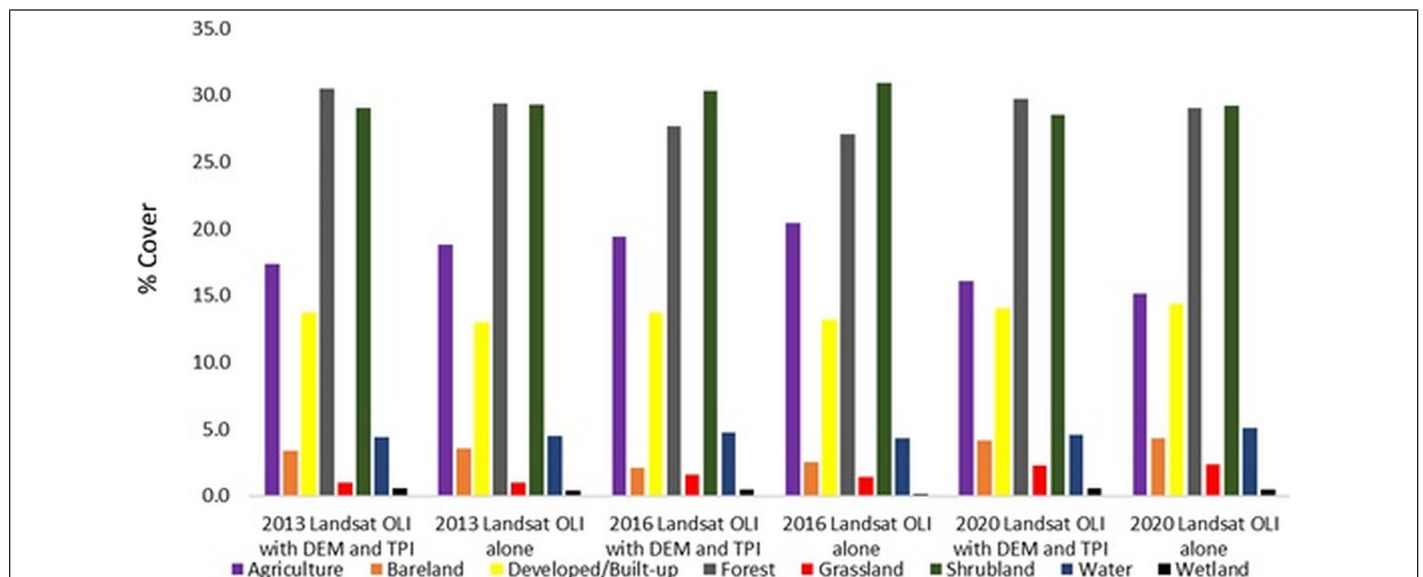
Figure 6. Percent cover of land cover and land use classes in Davidson County in the years 2020, 2016, and 2013 derived using Landsat Operational Land Imager (OLI) alone, with Light Detection and Ranging-Digital Elevation Model (lidar-DEM) and derived Topographic Position Index (TPI).

In the 2020 urban land cover and land use classification, the producer's accuracy that represented the ability of the Random Forest classification algorithm to generate land cover and land use categories was highest (100%) for water and lowest (81.7%) for wetlands when Landsat OLI was integrated with lidar-DEM and TPI in the classification (Table 2). Likewise, water and wetlands had the most (100%) and least (66.4%) producer's accuracies, respectively, when standalone Landsat OLI was used in the 2020 classification (Table 2). This implies the Random Forest classification algorithm likely detected water easily relative to wetland in the 2020 classification. In contrast, the user's accuracy that demonstrated how well the classified urban land cover and land use categories on the map represented land cover and land use on the ground was maximum (98%) for water and minimum (71%) for grassland when Landsat OLI was used alone in the 2020 classification. Similarly, water and wetland classes had the most user's accuracy (98%) and grassland had the least user's accuracy (84%) when lidar-DEM and TPI were added to Landsat OLI in the 2020 classification (Table 2). Furthermore, when Landsat OLI was combined with lidar-DEM and derived TPI in the 2020 urban land cover and land use classification, wetland had the most gain in both producer's and user's accuracies, whereas water had the least gain in accuracy. The average user's and producer's accuracies in the 2020 urban land cover and land use classification were about 87% and 86%, respectively. The kappa

value that indicated the correlation between the classified urban land cover and land use classes to the reference data (Google Earth data) increased from 0.8 to 0.89 when lidar-DEM and derived TPI were added to Landsat OLI in the 2020 classification relative standalone Landsat OLI.

In the 2016 urban land cover and land use classification, the producer's accuracy was maximum (100%) for water and minimum (76.3%) for grassland when Landsat OLI was integrated with lidar-DEM and derived TPI (Table3). However, when Landsat OLI was used alone in the classification, the producer's accuracy was highest (100%) for water and lowest (66.4%) for wetland (Table 3). In contrast, water had the most user's accuracy (98%) and grassland had the least user's accuracy (74%) in the 2016 classification when Landsat OLI was combined with lidar-DEM and derived TPI (Table 3). Likewise, the user's accuracy was maximum for water (98%) and minimum for grassland (69%) when standalone Landsat OLI was used in the 2016 classification. Furthermore, when Landsat OLI was integrated with lidar-DEM and derived TPI in the 2016 classification, shrubland had the most gain in both producer's and user's accuracies, whereas water had the least gain in accuracy. The mean user's and producer's accuracies in the 2016 urban land cover and land use classification increased by around 7% and 9%, respectively when lidar-DEM and TPI were added to Landsat OLI in the 2016 classification relative to standalone Landsat OLI satellite data. Similarly, the Kappa value increased from 0.78 to 0.86 when lidar-DEM

Table 2. Accuracy assessment of urban land cover and land use classification of 2020.

Land Cover and Land Use Classes	User's Accuracy (%) Year 2020			Producer's Accuracy (%) Year 2020		
	Landsat OLI Alone	Landsat OLI with DEM and TPI	Change in Accuracy	Landsat OLI Alone	Landsat OLI with DEM and TPI	Change in Accuracy
Agriculture	88.5	91.0	2.5	85.5	92.4	6.9
Bare land	81.0	87.0	6.0	86.2	91.6	5.4
Developed/Built-up	95.0	95.0	0.0	96.0	97.4	1.5
Forest	74.0	87.0	13.0	85.1	91.1	6.0
Grassland	71.0	84.0	13.0	76.3	82.4	6.0
Shrubland	74.5	85.0	10.5	70.6	84.2	13.5
Water	98.0	98.0	0.0	100.0	100.0	0.0
Wetland	83.0	98.0	15.0	66.4	81.7	15.3

Overall Accuracy (%) Year 2020			Kappa Value Year 2020		
Landsat OLI Alone	Landsat OLI with DEM and TPI	Change in Accuracy	Landsat OLI Alone	Landsat OLI with DEM and TPI	Change in Kappa Value
83.00	90.00	7.00	0.80	0.89	0.09

Landsat OLI = Landsat Operational Land Imager (OLI); Light Detection and Ranging-Digital Elevation Model = lidar-DEM; Topographic Position Index = TPI.

Table 3. Accuracy assessment of urban land cover and land use classification of 2016.

Land Cover and Land Use Classes	User's Accuracy (%) Year 2016			Producer's Accuracy (%) Year 2016		
	Landsat OLI Alone	Landsat OLI with DEM and TPI	Change in Accuracy	Landsat OLI Alone	Landsat OLI with DEM and TPI	Change in Accuracy
Agriculture	87.0	88.5	1.5	83.3	86.3	3
Bare land	81.0	84.0	3.0	86.2	91.3	5.1
Developed/Built-up	92.5	95.0	2.5	95.9	97.4	1.5
Forest	74.0	87.0	13.0	79.1	86.6	7.5
Grassland	69.0	74.0	5.0	71.9	76.3	4.4
Shrubland	68.0	81.0	13.0	68.7	83.5	14.8
Water	98.0	98.0	0.0	100	100	0
Wetland	83.0	94.0	11.0	66.4	79.7	13.3

Overall Accuracy (%) Year 2016			Kappa Value Year 2016		
Landsat OLI Alone	Landsat OLI with DEM and TPI	Change in Accuracy	Landsat OLI Alone	Landsat OLI with DEM and TPI	Change in Kappa Value
81.00	88.00	7.00	0.78	0.86	0.08

Landsat OLI = Landsat Operational Land Imager (OLI); Light Detection and Ranging-Digital Elevation Model = lidar-DEM; Topographic Position Index = TPI.

and derived TPI were integrated with Landsat OLI in the classification relative Landsat OLI alone.

In the 2013 urban land cover and land use classification, the producer's accuracy was highest (100%) for water and lowest (74%) for grassland when Landsat OLI was combined with lidar-DEM and derived TPI (Table 4). However, when Landsat OLI was used alone in the classification, water had the most producer's accuracy of about 100% and wetland had the least producer's accuracy of approximately 66.4% (Table 4). In contrast, the user's accuracy was maximum (98%) for water and minimum (71.5%) for shrubland when Landsat OLI was used alone in the 2013 classification. Nonetheless, when lidar-DEM and TPI were added to Landsat OLI in the classification, water had the most user's accuracy of about 98% and grassland had the least user's accuracy of around 74% (Table 4). In addition, when Landsat OLI was integrated with lidar-DEM and TPI in the 2013 classification, wetland had the most gain in both producer's and user's accuracies, whereas water and agriculture had the least gain in accuracies. Both the user's and producer's accuracies in the 2013 urban land cover and land use classification increased on average by around 5% when lidar-DEM and TPI were added to Landsat OLI in the classification relative to stand-alone Landsat OLI. Likewise, the Kappa value increased from 0.8 to 0.85 when lidar-DEM and derived TPI were combined with Landsat OLI in the 2013 classification relative Landsat OLI alone (Table 4).

The lowest user's accuracy of grassland was consistent in the 2020, 2016, and 2013 urban land cover and land use classifications. The lowest user's accuracy of grassland indicated greater confusion between grassland and other urban land cover and land use types such as agriculture and wetland. This is possibly because wetland and agriculture environments consist of a significant amount of grasses. Furthermore, the range in kappa values (0.78–0.89) in the 2020, 2016, and 2013 urban land cover and land use classifications indicated a very good correlation between the classified land cover and land use categories to the reference data assuming the data are randomly sampled from a multinomial distribution with a large sample size (Montserud and Leamans 1992).

Urban Land Cover and Land Use Change Analysis

This study found a significant change in urban land cover and land use classes in Davidson County, Tennessee in the periods of 2013, 2016, and 2020 (Table 5). On average, the area covered by agriculture increased by about 10% between 2013 and 2016 and decreased by about 22% between 2016 and 2020 (Table 5). The net gain in agriculture between 2013 and 2016 was about 2700 ha and was predominantly due to the conversion of bareland and shrubland to agricultural land (Tables 6 and 7). The net loss in agriculture between 2016 and 2020 was about 4500 ha and was primarily due to the conversion of agriculture to bareland and shrubland (Tables 8 and 9). The conversion of agriculture to bareland and shrubland and vice versa is likely due to normal crop cycling (Li *et al.* 2019; Rondhi *et al.* 2018).

The bareland cover decreased by about 34% between 2013 and 2016 and increased by about 85% between 2016 and 2020 (Table 5). The net loss in bareland between 2013 and 2016 was about 1500 ha and was mostly due to the conversion of bareland to agriculture (Tables 6 and 7). In contrast, the net gain in bareland between 2016 and 2020 was around 2600 ha and was mainly as a result of the conversion of agriculture to bareland (Tables 8 and 9). Other environmental factors including but not limited to the clearing of grasses, shrubs and forests for residential development also contributed to increase in bareland. Furthermore, the tornado event that occurred in Davidson County in March of 2020 (National Weather Service 2020) a few months before the Landsat OLI satellite data was acquired likely also contributed to the gains in bareland between 2016 and 2020 relative to 2013 and 2016. In addition, the fluctuation in rivers and lakes' shorelines likely also contributed to the gains and losses in bareland.

On average, the area covered by developed/built-up areas increased by about 1% between 2013 and 2016. Furthermore, it increased by approximately 6% between the periods of 2016 and 2020 (Table 5). The

Table 4. Accuracy assessment of urban land cover and land use classification of 2013.

Land Cover and Land Use Classes	User's Accuracy (%) Year 2013			Producer's Accuracy (%) Year 2013		
	Landsat OLI Alone	Landsat OLI with DEM and TPI	Change in Accuracy	Landsat OLI Alone	Landsat OLI with DEM and TPI	Change in Accuracy
Agriculture	87	87	0	86.1	86.1	0.0
Bare land	81	84	3	86.2	91.3	5.1
Developed/Built-up	92.5	95	2.5	95.9	97.4	1.6
Forest	74	87	13	82.2	84.9	2.7
Grassland	76	74	-2	73.8	74.0	0.2
Shrubland	71.5	79	7.5	69.8	83.2	13.4
Water	98	98	0	100.0	100.0	0.0
Wetland	83	94	11	66.4	79.7	13.3
	Overall Accuracy (%) Year 2013			Kappa Value Year 2013		
	Landsat OLI Alone	Landsat OLI with DEM and TPI	Change in Accuracy	Landsat OLI Alone	Landsat OLI with DEM and TPI	Change in Kappa Value
	82.00	87.00	5.00	0.80	0.85	0.05

Landsat OLI = Landsat Operational Land Imager (OLI); Light Detection and Ranging-Digital Elevation Model = lidar-DEM; Topographic Position Index = TPI.

Table 5. Change in urban land cover and land use classes in Davidson County, Tennessee.

Urban Land Cover and Land Use Classes	Mean Area (ha) Cover 2013	Mean Area (ha) Cover 2016	Mean Area (ha) Cover 2020	% Change 2013 & 2016	% Change 2013 & 2020	% Change 2016 & 2020
Agriculture	24 603	27 083	21 247.5	10.1	−13.6	−21.5
Bareland	4724.5	3112	5749.5	−34.1	21.7	84.8
Developed/Built-up	18 192	18 322	19 330.5	0.7	6.3	5.5
Forest	40 741.5	37 253.5	39 940	−8.6	−2.0	7.2
Grassland	1355.5	2023	3157.5	49.2	132.9	56.1
Shrubland	39 692	41 671	39 287	5.0	−1.0	−5.7
Water	6018.5	6149.5	6591.5	2.2	9.5	7.2
Wetland	681	394	704.5	−42.1	3.5	78.8

Table 6. Area (ha) transition matrix for the period 2013–2016, Davidson County (land cover and land use map derived using Landsat Operational Land Imager (OLI) with Digital Elevation Model (DEM) and Topographic Position Index (TPI).

Land Cover and Land Use Classes in 2013	Land Cover and Land Use Classes in 2016									
	Agriculture	Bareland	Developed	Forest	Grassland	Shrubland	Water	Wetland	Total 2013	Losses
Agriculture	13 102	894	1186	646	216	7378	177	0	23 599	10 497
Bareland	1564	974	876	130	61	952	28	0	4585	3611
Developed	742	303	14 411	53	40	2693	413	0	18 655	4244
Forest	1204	599	930	31 289	9	6940	447	62	41 480	10 191
Grassland	63	10	16	1	1077	197	2	0	1365	288
Shrubland	9453	0	841	5453	694	22 687	241	162	39 531	16 844
Water	203	29	316	66	2	433	4928	0	5976	1048
Wetland	49	32	95	52	3	0	218	368	817	449
Total 2016	26 380	2841	18 670	37 689	2102	41 280	6454	592	136 008	
Gains	13 278	1867	4259	6400	1025	18 593	1526	224		

Table 7. Area (ha) transition matrix for the period 2013–2016, Davidson County (land cover and land use map derived using standalone Landsat Operational Land Imager (OLI)).

Land Cover and Land Use Classes in 2013	Land Cover and Land Use Classes in 2016									
	Agriculture	Bareland	Developed	Forest	Grassland	Shrubland	Water	Wetland	Total 2013	Losses
Agriculture	13 750	2191	1603	254	359	7368	82	0	25 607	11 857
Bareland	1691	529	827	403	139	1249	27	0	4864	4335
Developed	500	311	14 084	41	54	2623	116	0	17 729	3645
Forest	800	265	600	31374	42	6620	302	0	40 003	8629
Grassland	146	26	20	1	1052	100	1	0	1346	294
Shrubland	10 745	26	540	4652	269	23 471	150	0	39 853	16 382
Water	154	10	203	40	30	481	5138	5	6061	923
Wetland	0	25	96	53	0	150	30	191	545	354
Total 2016	27 786	3383	17 973	36 818	1944	42 062	5845	196	136 008	
Gains	14 036	2854	3889	5444	892	18 591	707	5		

Table 8. Area (ha) transition matrix for the period 2016–2020, Davidson County (land cover and land use map derived using Landsat Operational Land Imager (OLI) with Digital Elevation Model (DEM) and Topographic Position Index (TPI).

Land Cover and Land Use Classes in 2016	Land Cover and Land Use Classes in 2020									
	Agriculture	Bareland	Developed	Forest	Grassland	Shrubland	Water	Wetland	Total 2016	Losses
Agriculture	12 334	3552	1679	3910	464	4306	0	135	26 380	14 046
Bareland	839	800	725	78	54	325	10	10	2841	2041
Developed	770	399	14 542	158	76	2233	391	101	18 670	4128
Forest	590	338	279	32 485	19	3909	69	0	37 689	5204
Grassland	161	40	41	26	1740	90	1	1	2102	362
Shrubland	7061	500	1675	3251	730	27 421	300	342	41 280	13 859
Water	47	9	70	397	2	459	5436	34	6454	1018
Wetland	63	40	80	83	4	82	59	181	592	411
Total 2020	21 866	5678	19 090	40 389	3090	38 825	6266	804	136 008	
Gains	9532	4878	4548	7904	1350	11 404	830	623		

Table 9. Area (ha) transition matrix for the period 2016–2020, Davidson County (land cover and land use map derived using standalone Landsat Operational Land Imager (OLI)).

Land Cover and Land Use Classes in 2016	Land Cover and Land Use Classes in 2020									
	Agriculture	Bareland	Developed	Forest	Grassland	Shrubland	Water	Wetland	Total 2016	Losses
Agriculture	13 510	2551	1682	2542	856	6420	100	125	27 786	14 276
Bareland	820	924	705	424	39	350	69	52	3383	2459
Developed	476	598	14 259	98	82	2014	349	98	17 974	3715
Forest	474	229	225	31 131	22	4480	93	164	36 818	5687
Grassland	206	47	40	51	1499	93	4	4	1944	445
Shrubland	5094	1454	2650	5114	718	26 290	742	0	42 062	15 772
Water	49	18	10	93	5	102	5508	60	5845	337
Wetland	0	0	0	38	4	0	52	102	196	94
Total 2020	20 629	5821	19 571	39 491	3225	39 749	6917	605	136 008	
Gains	7119	4897	5312	8360	1726	13 459	1409	503		

net gain in developed/built-up area between 2013 and 2016 was about 130 ha, whereas the net gain between 2016 and 2020 was approximately 1000 ha. The net gain in developed/built-up area was mostly from the conversion of agriculture and shrubland to built-up area (Tables 6–9). The net gain in developed/built-up areas was to accommodate the rise in population in Davidson County. The increasing trend in developed/built-up areas is consistent with the findings of Homer *et al.* (2020) where they found a net gain in developed areas especially in the southern United States.

The forest area decreased by about 9% between 2013 and 2016 and in the periods of 2016 and 2020, forest increased by about 7% on average (Table 5). The net loss in forest cover between 2013 and 2016 was about 3500 ha and was mostly due to the conversion of forest to agriculture, developed/built-up, and shrubland (Tables 6 and 7). In contrast, the net gain in forest between 2016 and 2020 was around 2700 ha and was primarily due to the conversion of shrubland to forest (Tables 8 and 9). Furthermore, the losses and gains in forest cover are likely due to forest harvest and regrowth that is common in the southeastern United States.

Grassland was found to increase by about 49% and 56% in the periods between 2013 and 2016, and between 2016 and 2020, respectively (Table 5). The net gain in grassland between 2013 and 2016 was around 700 ha, whereas the net gain between 2016 and 2020 was about 1200 ha. The net gain in grassland was mostly from the conversion of agriculture and shrubland to grassland (Tables 6–9). The net gain in grassland from 2013 to 2020 is also likely due to urbanization. This is because newly constructed residential buildings are usually designed with grassland lawns for aesthetic and recreational purposes. Furthermore, the increase in grassland can also be attributed to shrubland and forest losses (Homer *et al.* 2020).

In the years 2013 and 2016, shrubland increased by about 5% and decreased by around 6% between 2016 and 2020 on average (Table 5). The net gain in shrubland between 2013 and 2016 was about 2000 ha and was typically due to the conversion of agriculture and forest to shrubland (Tables 6 and 7). In contrast, the net loss in shrubland between 2016 and 2020 was around 2400 ha and was primarily due to the conversion of shrubland to forest and agriculture (Tables 8 and 9). The fluctuation in shrubland is heavily influenced by forest cutting and regeneration.

On average, the area covered by open water increased by about 2% between 2013 and 2016 and increased by approximately 7% between 2016 and 2020 (Table 5). The net gain in open water between 2013 and 2016 was around 130 ha, whereas the net gain between 2016 and 2020 was about 400 ha (Tables 6–9). In contrast, the area covered by wetland decreased by about 42% between 2013 and 2016 and increased by around 79% between 2016 and 2020 (Table 5). The net loss in wetland between 2013 and 2016 was about 285 ha and was mostly due to the conversion of wetland to open water (Tables 6 and 7). In contrast, the net gain in wetland between 2016 and 2020 was around 300 ha and was primarily due to the conversion of shrubland to wetland (Tables 8 and 9). Furthermore, the fluctuation in wetland and open water can also be attributed to weather and climate conditions such as precipitation, land use intensity, and other external disturbances. For example, the total precipitation in the month of August 2020 in Nashville was about 5.9 inches, whereas the total precipitation in the months of June 2016 and September 2013 was approximately 4.5 inches (National Oceanic and Atmospheric Administration 2021). The high precipitation in August of 2020 likely contributed to the net gain in water and wetlands between 2016 and 2020, relative to 2013 and 2016.

In the years of 2013 and 2016, the losses in urban land cover and land use change occurred in all land cover and land use types with significant losses in agriculture and shrubland especially in the central and eastern parts of the study area (Figure 7).

Similarly, urban land cover, and land use gains also occurred in all land cover and land use types with significant gains in agriculture and shrubland especially in the central and eastern portions of the study area (Figure 7).

In the years of 2016 and 2020, losses occurred all urban land cover and land use types with significant losses in agriculture and shrubland especially in the central and eastern parts of the study area (Figure 8). Likewise, gains occurred in all urban land cover and land use types

Figure 7. The gains (below) and losses (above) of specific land cover and land use types in Davidson County from 2013–2016 derived from Landsat Operational Land Imager (OLI) with Topographic Position Index (TPI) and Light Detection and Ranging-Digital Elevation Model (lidar-DEM); and standalone Landsat OLI classification maps.

with significant gains in agriculture and shrubland especially in the central and eastern parts of the study area (Figure 8).

In the years 2013 and 2016, total change in urban land cover and land use was detected in about 94 344 ha of the study area when Landsat OLI was integrated with lidar-DEM and derived TPI in the classification. However, total change was detected in around 92 838 ha of the study area when Landsat OLI was used alone in the classification. On average, total urban land cover and land use change occurred in about 70% of the study area between 2013 and 2016. The urban land cover and land use change occurred predominantly in the central, eastern, and southern parts of Davidson County (Figure 9).

In the periods of 2016 and 2020, total change in urban land cover and land use was detected in about 82 138 ha of the study area when Landsat OLI was combined with lidar-DEM and derived TPI in the classification. In contrast, when Landsat OLI was used alone in the classification, total urban land cover and land use change was detected in approximately 85 570 ha of the study area. On average, total urban land cover and land use change occurred in about 63% of the study area between 2016 and 2020. The urban land cover and land use change occurred largely in the central, eastern, and southern portions of Davidson County in the periods of 2016 and 2020 (Figure 10).

No change in urban land cover and land use in Davidson County occurred mostly in the western parts of the study area between 2013–2016 and 2016–2020. The no change areas consisted of all land cover and land use types. However, forest covered most of the area with no change detection relative to agriculture. The large undisturbed forest is therefore contributing to climate change mitigation (Buotte *et al.* 2019; Woodbury *et al.* 2007).

Conclusion

This study has classified, mapped, and monitored urban land cover and land use categories in Davidson County, Tennessee for the years of 2013, 2016, and 2020. Landsat OLI was integrated with lidar-DEM and derived TPI to classify urban land cover and land use classes. The
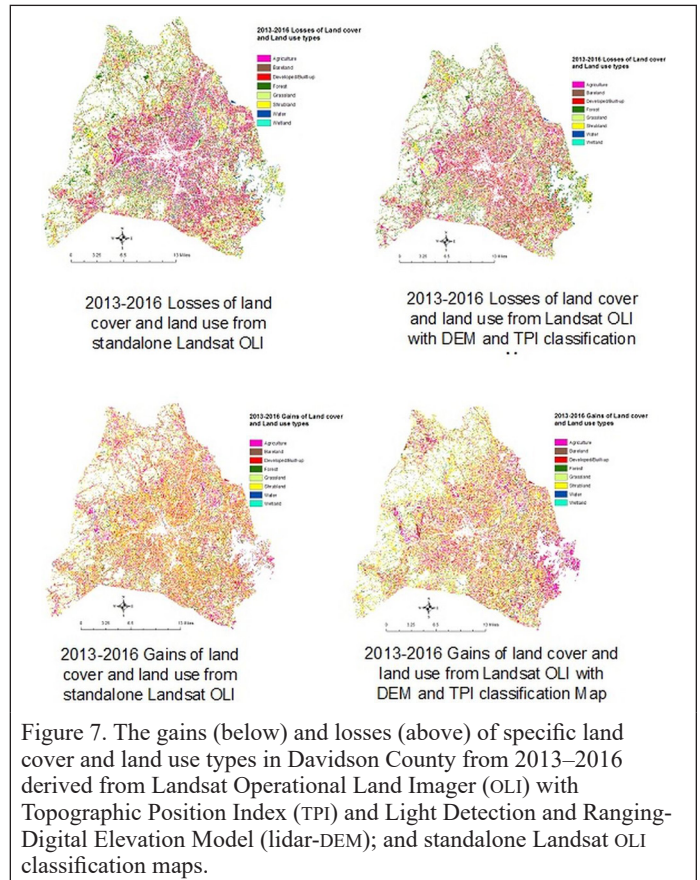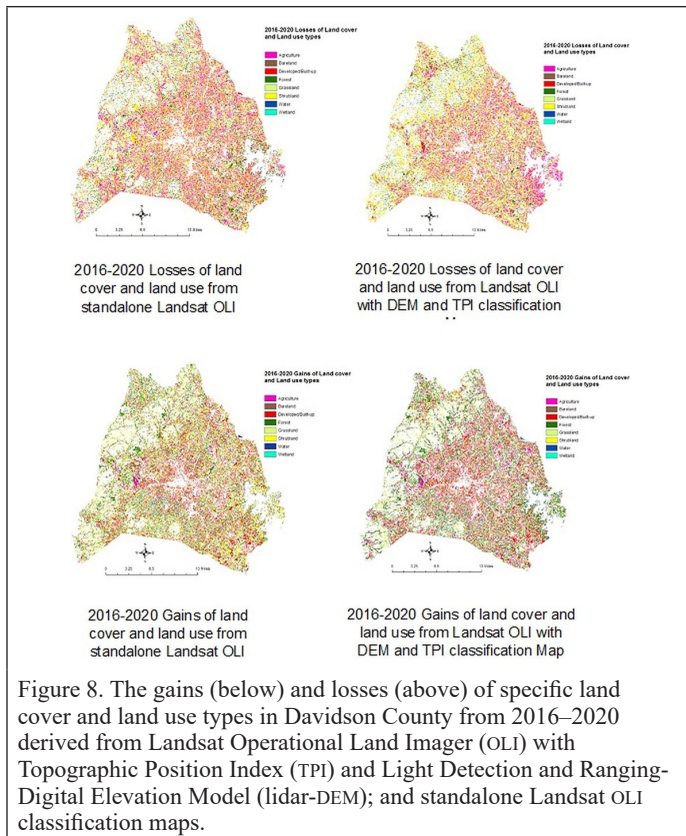
Figure 8. The gains (below) and losses (above) of specific land cover and land use types in Davidson County from 2016–2020 derived from Landsat Operational Land Imager (OLI) with Topographic Position Index (TPI) and Light Detection and Ranging-Digital Elevation Model (lidar-DEM); and standalone Landsat OLI classification maps.
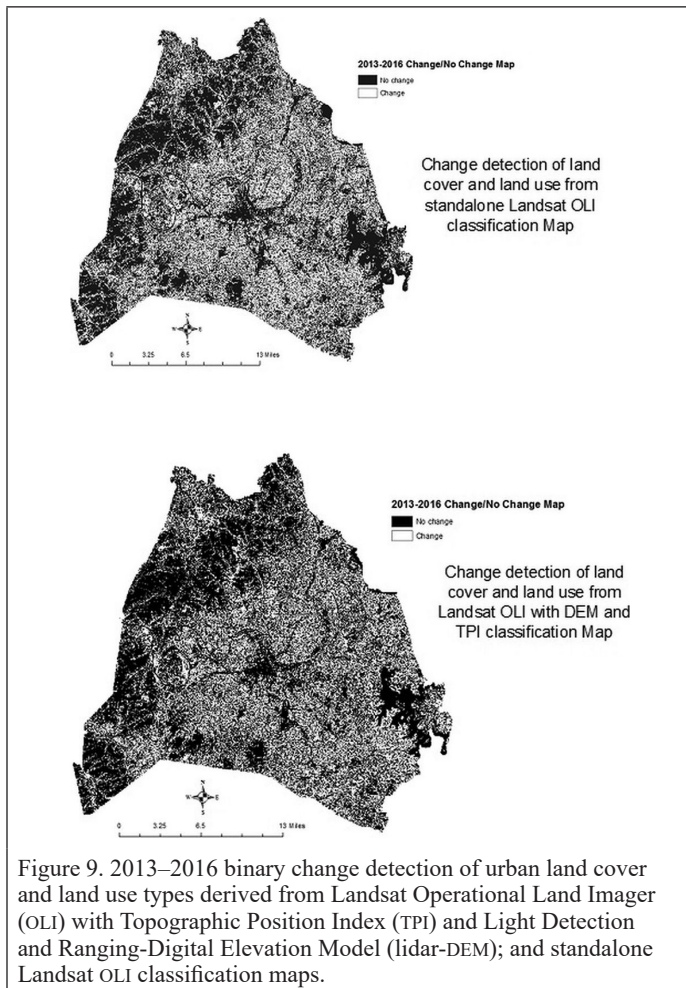
Figure 9. 2013–2016 binary change detection of urban land cover and land use types derived from Landsat Operational Land Imager (OLI) with Topographic Position Index (TPI) and Light Detection and Ranging-Digital Elevation Model (lidar-DEM); and standalone Landsat OLI classification maps.
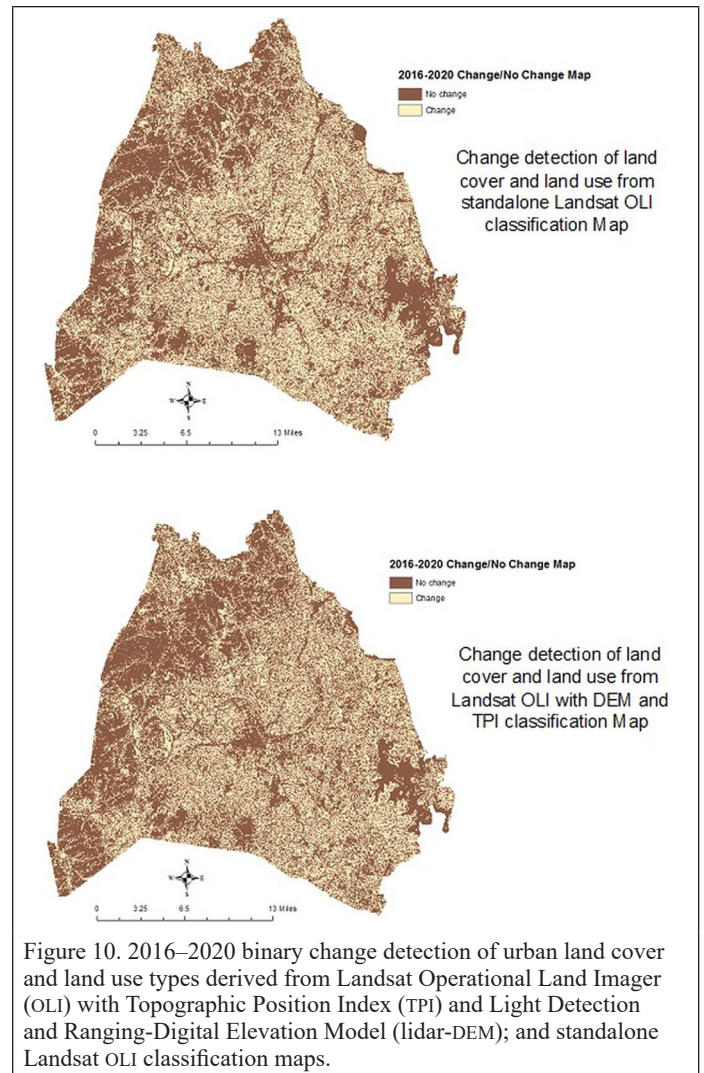
Figure 10. 2016–2020 binary change detection of urban land cover and land use types derived from Landsat Operational Land Imager (OLI) with Topographic Position Index (TPI) and Light Detection and Ranging-Digital Elevation Model (lidar-DEM); and standalone Landsat OLI classification maps.

addition of lidar-DEM and derived TPI to Landsat OLI satellite data improved the overall accuracy of the 2020 classification from 83% to 90% relative to Landsat OLI alone. Furthermore, the overall accuracy of the 2016 classification also increased from 81% to 88% and the 2013 classification improved from 82% to 87% when lidar-DEM and derived TPI were added to Landsat OLI in the classifications. Wetland and shrubland had the most gain in both producer's and user's accuracies, whereas water had the least gain in accuracies when Landsat OLI was integrated with lidar-DEM and derived TPI in the classifications. This study found a very good correlation between the classified urban land cover and land use categories and the reference data with kappa values in the range of 0.78 to 0.89.

Furthermore, this study found a significant change in urban land cover and land use classes in Davidson County in the years of 2013, 2016, and 2020. On average between 2013 and 2016, total urban land cover and land use change occurred in about 70% of the study area, whereas between 2016 and 2020, total change occurred in about 63% of Davidson County. In the years 2013 and 2016, agriculture had the highest net gain, whereas developed /built-up had the lowest net gain. In contrast, forest had the maximum net loss while wetland had the minimum net lost. In the periods between 2016 and 2020, forest had the maximum net gain, whereas wetland had the minimum net gain. Furthermore, agriculture was the land cover type that had the most net loss and shrubland had the least net loss between 2016 and 2020.

The gains and losses in urban land cover and land use are due to several factors included but not limited to urbanization, forest harvest and regrowth, conversion of shrubland to forest, weather, and climatic conditions such as precipitation and tornado. This study improves our understanding of the recent urban land cover and land use change in

Davidson County, Tennessee, United States. Furthermore, it quantitatively classified, mapped, and monitored urban land cover and land use change relevant for urban development and planning.

Acknowledgments

References

Arnold, C., E. Wilson, J. Hurd and D. Civco. 2020. 30 years of land cover change in Connecticut, USA: A case study of long-term research, dissemination of results, and their use in land use planning and natural resource conservation. *Land* 9(8):255.

Bai, T., K. Sun, W. Li, D. Li, Y. Chen and H. Sui. 2021. A novel class-specific object-based method for urban change detection using high-resolution remote sensing imagery. *Photogrammetric Engineering and Remote Sensing* 87(4):249–262.

Belgiu, M. and L. Dragut. 2016. Random forest in remote sensing: A review of applications and future directions. *ISPRS Journal of Photogrammetry and Remote Sensing* 114:24–31.

Bellassen, V. and S. C. Luyssaert. 2014. Arbon sequestration: Managing forests in uncertain times. *Nature* 506:153–155.

Birhane, E., H. Ashfare, A. A. Fenta, H. Hishe, M. A. Gebremedhin, H. G. Wahed and N. Solomon. 2019. Land use land cover changes along topographic gradients in Hugumburda national forest priority area, Northern Ethiopia. *Remote Sensing Applications: Society and Environment* 13:61–68.

Breiman, L. 1999. *Random Forests—Random Features. Technical Report 567.* Berkeley, CA: Statistics Department, University of California. <ftp://ftp.stat.berkeley.edu/pub/users/breiman>.

Breiman, L. 2001. Random forests. *Machine Learning* 45:5–32.

Buotte, P. C., B. E. Law, W. J. Ripple and L. T. Berner. 2019. Carbon sequestration and biodiversity co-benefits of preserving forests in the western United States. *Ecological Applications* 30(2):e02039.

Cohen, M. J., F. Irena, I. F. Creed, L. Alexander, N. B. Basu, A.J.K. Calhoun, C. Craft, E. D'amico, E. Dekeyser and L. Fowler. 2016. Do geographically isolated wetlands influence landscape functions? *Proceedings of National Academy of Science USA* 113:1978–1986.

Costa, H., D. Almeida, F. Vala, F. Marcelino and M. Caetano. 2018. Land cover mapping from remotely sensed and auxiliary data for harmonized official statistics. *International Journal of Geo-Information* 7(157). https://doi.org/10.3390/ijgi7040157.

Elmaz, F., B. Buyukcakir, O. Yucel and A. Y. Mutlu. 2020. Classification of solid fuels with machine learning. *Fuel* 266(117066). https://doi.org/10.1016/j.fuel.2020.117066.

Environmental Systems Research Institute. 2021. *Difference Tool.* Redlands, CA: Environmental Systems Research Institute (ESRI).

Favero, A., A. Daigneault and B. Sohngen. 2020. Forests: Carbon sequestration, biomass energy, or both? *Science Advances* 6(13):eaay6792.

Foley, J. A., R. DeFries, G. P. Asner, C. Barfor, G. Bonan, S. R. Carpenter, F. S. Chapin, M. T. Coe, G. C. Daily, H. K. Gibbs, J. K. Helkowski, T. Holloway, E. A. Howard, C. H. Kucharik, C. Monfreda, J. A. Patz, I. C. Prentice, N. Ramankutty and P. K. Snyder. 2005. Global consequences of land use. *Science* 205:570–574.

Hodges, J. A., R. J. Norrell and M. H. Sarah. 2018. *Tennessee.* Chicago, IL: Encyclopedia Britannica, Inc.

Homer, C., J. Dewitz, S. Jin, G. Xian, C. Costello, P. Danielson, L. Gass, M. Funk, J. Wickham, S. Stehman, R. Auch and K. Riitters. 2020. Conterminous United States land cover change patterns 2001–2016 from the 2016 National Land Cover Database. *ISPRS Journal of Photogrammetry and Remote Sensing* 162 184–199.

Jenness, J., B. Brost and P. Beier. 2013. *Land Facet Corridor Designer.* Fort Collins, CO: USDA Forest Service Rocky Mountain Research Station, McIntire-Stennis Cooperative Forestry Program, Arizona Board of Forest Research.

Li, S., D. Nadolnyak and V. Hartarska. 2019. Agricultural land conversion: Impacts of economic and natural risk factors in a coastal area. *Land Use Policy* 80:380–390.

Liu, C., W. Li, H. Zhou, H. Yan and P. Xue. 2020. Land use/land cover changes and their driving factors in the northeastern Tibetan plateau based on geographical detectors and Google Earth engine: A case study in Gannan prefecture. *Remote Sensing* 12:3139.

Magidi, J., L. Nhamo, S. Mpandeli and T. Mabhaudhi. 2021. Application of the random forest classifier to map irrigated areas using Google Earth engine. *Remote Sensing* 13:876. https://doi.org/10.3390/rs13050876.

Mather, P. M. and M. Koch. 2011. *Computer Processing of Remotely-Sensed Images: An Introduction.* Chichester, England: John Wiley and Sons.

Meador, M. R. 1996. Tennessee wetland resources. In *National Water Summary on Wetland Resources*, Paper 2425, edited by J. D. Fretwell, J. S. Williams, P. J. Redman and comps., 357–361. Denver, CO: U.S. Geological Survey Water-Supply.

Mitsch, W. J., J. G. Gosselink, L. Zhang and C. J. Anderson. 2009. *Wetland Ecosystems.* Hoboken, NJ: Wiley.

Mojica, A. 2018. *Population Boom: Middle Tennessee Counties Among Fastest Growing in State.* Fox 17 News Nashville Web. <https://fox17.com/news/local/population-boom-middle-tennessee-counties-among-fastest-growing-in-state>.

Montserud, R. A. and R. Leamans. 1992. Comparing global vegetation maps with kappa statistics. *Ecological Modeling* 62:275–293.

National Aeronautics and Space Administration. 2018. *Landsat 8 Science Data Users Handbook.* Washington, DC: National Aeronautics and Space Administration, United States Geological Society.

National Oceanic and Atmospheric Administration. 2021. *Nashville, TN.* National Oceanic and Atmospheric Administration, National Weather Service Forecast Office. <https://w2.weather.gov/climate/index.php?wfo=ohx>.

National Weather Service. 2020. *March 2–3, 2020 Tornadoes and Severe Weather.* National Oceanic and Atmospheric Administration. <https://www.weather.gov/ohx/20200303>.

Patel, S. K., P. Verma and G. Shankar Singh. 2019. Agricultural growth and land use land cover change in peri-urban India. *Environmental Monitoring and Assessment* 191(600).

Pielke, R. A. 2005. Land use and climate change. *Science* 310(5754): 1625–1626.

Rondhi, M., P. A. Pratiwi, V. T. Handini, A. F. Sunartomo and S. A. Budiman. 2018. Agricultural land conversion, land economic value, and sustainable agriculture: A case study in East Java, Indonesia. *Land* 7:148.

Sefrin, O., F. M. Riese and S. Keller. 2021. Deep learning for land cover change detection. *Remote Sensing* 13(78). https://doi.org/10.3390/rs13010078.

Sellers, J. B. 2018. *Nashville Is One of the Fastest Growing U.S. Cities.* Crossville, Tennessee: Crossville Chronicle.

Shao, Z., L. Zhang, X. Zhou and L. Ding. 2014. A novel hierarchical semisupervised SVM for classification of hyperspectral images. *IEEE Geoscience And Remote Sensing Letters* 11(9):1609–1613.

Sharma, R. C., K. Hara and H. Hirayama. 2017. A machine learning and cross-validation approach for the discrimination of vegetation physiognomic types using satellite based multispectral and multitemporal data. *Hindawi Scientifica.* https://doi.org/10.1155/2017/9806479.

United States Census Bureau. 2018. *Davidson County Tennessee.* Washington, DC: U.S. Department of Commerce.

United States Climate Data. 2018. *Climate Nashville—Tennessee.* Your Weather Service-World Climate.

Verma, P., R. Singh, P. Singh and A. S. Raghubanshi. 2020. Urban ecology—Current state of research and concepts. In *Urban Ecology-Current State of Research and Concepts*, edited by P. Verma, P. Singh, P. Singh and A. S. Raghubanshi, 3–16. Amsterdam: Elsevier.

Weiss, A. 2001. Topographic position and landforms analysis. *Proceedings ESRI User Conference*, held in San Diego, CA. <http://www.jennessent.com/arcview/TPI_Weiss_poster.htm>.

Woodbury, P. B., J. E. Smith and L. S. Heath. 2007. Carbon sequestration in the U.S. forest sector from 1990 to 2010. *Forest Ecology and Management* 241(1–3):14–27.

Yao, Y., Y. Leung, T. Fung, Z. Shao, J. Lu, D. Meng, H. Ying and Y. Zhou. 2021. Continuous multi-angle remote sensing and its application in urban land cover classification. *Remote Sensing* 13(413). https://doi.org/10.3390/rs13030413.

Zhao, W., S. Du and W. J. Emery. 2017. Object-based convolutional neural network for high-resolution imagery classification. *IEEE Journal of Selected Topics in Applied Earth Observations and Remote Sensing.* https://doi.org/10.1109/JSTARS.2017.2680324.

Zhong, B., A. Yang, K. Jue and J. Wu. 2021. Long time series high-quality and high-consistency land cover mapping based on machine learning method at Heihe River Basin. *Remote Sensing* 13(1596). https://doi.org/10.3390/rs13081596.

Monitoring Earth Hazard with Remote Sensing Techniques

Natural and human disasters are increasingly affecting global communities worldwide in recent decades. With the increasing human population and urbanization, the earth is inevitably more susceptible to manmade hazards. Global warming and its associated environmental instability increase the frequency and severity of the disaster. Rapid Climate change is linked with meteorological events with a high degree of risk probability causing flood disasters. Implementation of proper hazard management such as disaster prevention, disaster preparedness, and adequate disaster relief would reduce the impact of natural disasters. Usage of the convectional earth observation model helps hazard management with a reliable solution but cannot provide early prediction of disaster occurrence, saving people's lives. However, using remote sensing techniques would enable warning systems by building futuristic codes that predict the hazards and warn people on time with greater accuracy. Remote sensing imagery provides a quick method for assessing the variation of hazard impacts, coastal inundation, erosion, and majority affected flood plains using intelligent, visionary technology. The data gathered from sensors provide valuable insights about the spatial phenomena that aid scientists in making accurate decisions about the forecast patterns. Above all satellites, remote sensing is used to detect global environmental problems, explore resources, and monitor disasters by capturing the earth's surface during altered weather conditions. This helps in the early detection of disaster patterns with futuristic mitigation procedures.

The sensors technology captures images of fires, flooding, and volcanic eruption can create a visual impact during the response phase that aids in readiness actions when people are viable to disaster risk. Earth observation systems and GIS helps professionals to make effective project planning with a more accurate analysis. The utilization of various spectral bands such as Visible, infrared, thermal infrared, and synthetic aperture radar provides adequate coverage of environmental patterns and allows technology enhancement to analyze data. Meteorological satellites use High-resolution transmission sensors for cyclone monitoring, intensity assessment, and storm surges. Geo-stationary satellites use global coverage sensors for flood and drought management by collections of multi-date imaginary data for rainfall and river stages. Using its unique spectral signature, it identifies the water standing areas, the sand casting of agricultural lands, and marooned villages to enable hazard recovery plans. SAR sensing system is used to detect forest fires and forest monitoring using microwave techniques to acquire sensory images. There are some challenges about using sensors for hazard prediction where research prospects are needed. As smart sensors use advanced technologies and complex data for prediction, data breaches would lead to misinterpretation of results, increasing the risk to human lives. An adequate skilled workforce is required to analyze the collected sensor data. In the future, integrating IoT and artificial intelligence would create autonomous drones that aid in inspecting the geographical patterns in multi-dimensional views to accelerate high definitions imagery for efficient prediction of results. This special issue enumerates the role of remote sensors for earth hazard predictions and future advancements. We welcome scholars and practitioners of this platform to emphasize this topic and present submissions that fall within the scope of remote sensing techniques for the accurate prediction of environmental hazards.

The topics of interest include:
- Role of Artificial intelligence in generating patterns in sensor data
- Disaster management cycle and it's important in hazard mitigation
- Advantages of geometrics in disaster risk management
- Usage and applications o GIS in flood forecasting
- Advanced Earth observation system tools for project planning
- RadarSat and use cases in detecting oil seeps
- Big data and its uses for accurate data collection in sensors
- Role of climate change in creating environmental risk
- Advancement in satellite sensors for earth's behavioral prediction
- Role of autonomous drones in capturing multispectral images

Deadline for Manuscript Submission
June 5, 2022

Submit your Manuscript to
http://asprs-pers.edmgr.com

Guest Editors
Dr. Priyan Malarvizhi Kumar, mkpriyan@khu.ac.kr and p.malarvizhikumar@ieee.org, *Department of Computer Science and Engineering, Kyung Hee University*, South Korea.

Dr. Fatemeh Afghah, fatemeh.afghah@nau.edu, S*chool of Informatics, Computing and Cyber Systems, Northern Arizona University.*

Dr. Manimuthu Arunmozhi, arunmozhi.m@ntu.edu.sg, *Cybersecurity Research Center (CYSREN), Nanyang Technological University*, Singapore.

Use of Commercial Satellite Imagery to Monitor Changing Arctic Polygonal Tundra

Amit Hasan, Mahendra Udawalpola, Anna Liljedahl, and Chandi Witharana

Abstract

Commercial satellite sensors offer the luxury of mapping of individual permafrost features and their change over time. Deep learning convolutional neural nets (CNNs) demonstrate a remarkable success in automated image analysis. Inferential strengths of CNN models are driven primarily by the quality and volume of hand-labeled training samples. Production of hand-annotated samples is a daunting task. This is particularly true for regional-scale mapping applications, such as permafrost feature detection across the Arctic. Image augmentation is a strategic "data-space" solution to synthetically inflate the size and quality of training samples by transforming the color space or geometric shape or by injecting noise. In this study, we systematically investigate the effectiveness of a spectrum of augmentation methods when applied to CNN algorithms to recognize ice-wedge polygons from commercial satellite imagery. Our findings suggest that a list of augmentation methods (such as hue, saturation, and salt and pepper noise) can increase the model performance.

Introduction

A network of polygonal patterns appears in the tundra due to the cracking and subsequent development of ice wedges. Ice-wedge polygons (IWPs) are one of the most common landforms across the Arctic tundra lowlands. Early studies (Leffingwell 1919) described two major types of IWPs: (1) polygons with elevated blocks or high-centered polygons and (2) polygons with depressed blocks or low-centered polygons. The microtopography associated with IWP controls a multitude of functions of the Arctic ecosystem (Kutzbach *et al.* 2004), such as permafrost and hydrologic dynamics from local to regional scales, due to the linkages between microtopography and the flow and storage of water (Liljedahl *et al.* 2016), vegetation succession (Magnússon *et al.* 2020), and permafrost dynamics (Lara *et al.* 2020). Widespread ice-wedge degradation is transforming low-centered polygons into high-centered polygons in a rapid phase (Steedman *et al.* 2016).

The entire Arctic has been imaged by high-spatial-resolution commercial satellite sensors, producing sheer volumes of data. Imagery archives are quickly morphing to petabyte scale. While studies have been conducted on vegetation dynamics (Verdonen *et al.* 2020), phenology (Zheng *et al.* 2020), vegetation classification (Davidson *et al.* 2016), and spectral and seasonal variation of leaf area index (Juutinen *et al.* 2017), imagery-derived products lag behind. We are in the process of translating these big imagery resources to Arctic science–ready products. Our ongoing research investigates the automated detection of IWPs from commercial satellite imagery.

The successful implementation of deep learning (DL) convolutional neural nets (CNNs) in computer vision applications has received a great deal of interest from the remote sensing community (Ma *et al.* 2019). There has been an upsurge of recent research that exhibits DLCNN applications in a multitude of remote sensing classification problems, such as land use and land cover types of detection (Paoletti *et al.* 2019; Zhang *et al.* 2019), agricultural crop mapping (Zhong *et al.*

2019), feature extraction from remote sensing images (Romero *et al.* 2016), object localization (Long *et al.* 2017), cloud detection (Xie *et al.* 2017), and disaster recognition (Liu & Wu 2016). DLCNNs perform well in terms of object detection (Zhao *et al.* 2019), image segmentation (Rizwan I Haque and Neubert 2020), and semantic object instance segmentation (Lateef and Ruichek 2019). An array of DLCNN architectures have been developed, trained, and tested with different types of imagery. Each of these architectures has its own advantages and disadvantages with respect to computation time and resources. Among many others, Mask R-CNN, U-Net, and Deeplab V3+ stand out as superior methods in semantic object instance segmentation. Researchers used Deeplab V3+ with the Pascal VOC data set and achieved 89% intersection over union (IoU). In a separate biological image segmentation data set, the U-Net model achieved a total of 85.5% IoU (Karimov *et al.* 2019). There is an increasing interest in the application of the Mask R-CNN model for Earth science applications (Su *et al.* 2019; Bhuiyan *et al.* 2020; Carvalho *et al.* 2021; Mahmoud *et al.* 2020; Zabawa *et al.* 2020; Zuo *et al.* 2020). Previous studies have shown promising results found by the implementation of DLCNN with commercial satellite imagery (Zhang *et al.* 2018; Bhuiyan *et al.* 2020; Witharana *et al.* 2020). By design, inferential strengths of CNN models are fueled largely by the quality and volume of hand-labeled training data. Production of hand-annotated samples is a daunting task. This is particularly true for regional-scale mapping applications, such as permafrost feature detection across the Arctic, where landscape complexity would spontaneously inflate the semantic complexity of submeter-resolution imagery. Additionally, image dimensions, multispectral channels, imaging conditions, and seasonality, coupled with multi-scale organization of geo-objects, pose extra challenges on the generalizability of DLCNN models. Image augmentation is a strategic "data-space" solution to synthetically inflate the size and quality of training samples without additional investments on hand annotations. A plethora of augmentation methods have been proposed under the auspices of two general categories: data warping and oversampling (Shorten and Khoshgoftaar 2019). The performance of image augmentation methods depends largely on the image recognition problem on hand and the characteristics of the underlying data. Researchers have used color augmentation techniques for skin lesion segmentation and classification (Galdran *et al.* 2017), geometric transformation with chest X-ray for the screening of COVID-19 (Elgendi *et al.* 2021), and noise injection techniques for plant leaf disease detection (Arun Pandian *et al.* 2019).

In this study, we have investigated the efficacy of 17 augmentation methods in relation to IWP detection. We relied on the Mask R-CNN algorithm as the base model in the training and the prediction of IWPs. The Mask R-CNN model itself has a lot of room to modify and tweak the default parameters (He *et al.* 2017). The backbone of the model is a convolutional neural network. This can be changed to different types of CNN models; we used the ResNet-50 structure (He *et al.* 2015) as the backbone. To initialize the model, we have practiced the transfer learning approach. In this approach, the model is already trained based on another hand-labeled data set. Our backbone was pretrained based on

Amit Hasan, Mahendra Udawalpola, and Chandi Witharana are with the University of Connecticut, Storrs, CT 06269 (amit.hasan@uconn.edu).

Anna Liljedahl is with the Woodwell Climate Research Center, Falmouth, MA 02540.

the ImageNet data set. We retrained the Mask R-CNN model with different augmentation methods using our data set so that the model could be used for the detection and segmentation of the IWPs. One of the major weaknesses of the DLCNNs is that spectral and spatial variations in the training data set affect the model performance (Grm *et al.* 2018). In our data, the spectral, spatial, and textural characteristics of IWPs vary based on the tundra vegetation types (Stow *et al.* 1993; Sturtevant *et al.* 2013; Mikola *et al.* 2018). Thus, separate Mask R-CNN models are trained for different tundra types.

The main goal of this study is to explore the potential of augmentation methods on top of a state-of-the-art DLCNN method (Mask R-CNN) to characterize the tundra IWP landscape as well as to assess the change in the model performance when trained with separate tundra types. We conducted a multi-step quantitative assessment to assess the precision, recall, F1 score, and overall accuracy of the prediction results from each of the augmentation scenarios.

Methods

Study Area

We extracted a total of 696 image tiles of varying dimensions (such as 292 × 292, 345 × 345, 507 × 507, and 199 × 199 pixels) out of seven satellite imagery scenes from the Norths Slope of Alaska, Prince Patrick Island, Banks Island, Inuvik in Canada, and Nizhnekolymskiy Ulus in Russia (Figure 1). These areas are covered mostly by tussock and non–tussock sedge tundra, sedge/grass, moss wetland, and other types of tundra. We hand annotated a total of 25,509 polygons (15,989 low-centered and 9520 high-centered polygons) from the satellite image scenes.

We prepared three sets of images out of all annotated patches as the training (487 images), test (106 images), and validation (103 images) data sets. The training data set was used for training the model, and the validation data set was used to check model performance while training the model. The test data set was used to calculate the performance of the trained model.

Model Architecture

Our experimental design was centered on the Mask R-CNN model architecture (He *et al.* 2017) (Figure 2). This model is specialized in object detection as well as instance segmentation at the same time.

We built the work flow based on an open-source package, built on Keras and TensorFlow developed by the Mask R-CNN team, that is available on Github (Waleed Abdulla 2017). The Mask R-CNN model consists of a CNN backbone, a region proposal network, and neural networks for predicting classes, bounding boxes, and masks (Figure 2). We used ResNet-50 (He *et al.* 2016) pretrained with the ImageNet data set as the backbone of the Mask R-CNN network. The final outputs of the model consist of the polygons detected inside the bounding boxes as well as in the form of masks and the class names (high-centered or low-centered polygons) corresponding to each of those detected polygons.
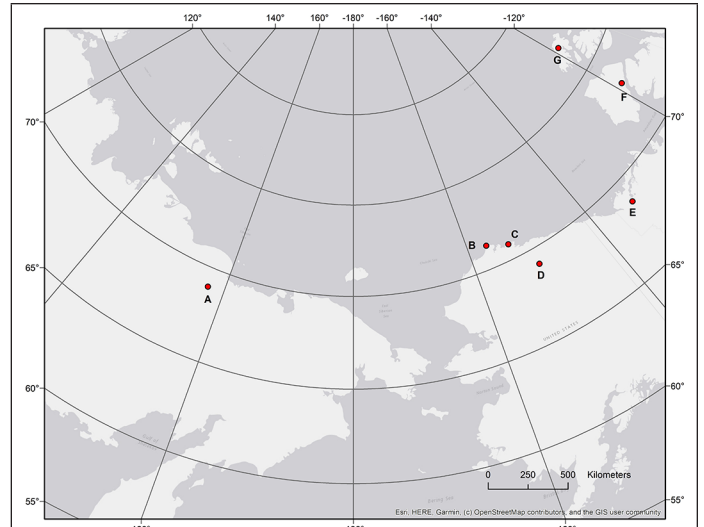

Figure 1. Geographical distribution of study sites: (A) Nizhnekolymskiy Ulus, Russia. (B) Barrow, Alaska, USA. (C) Atqasuk, Alaska, USA. (D) Prudhoe Bay, Alaska, USA. € Inuvik, Canada. (F) Banks Island, Canada. (G) Prince Patrick Island, Canada.

Augmentation Methods

Image augmentation is a process that modifies training images in a variety of ways and acts like additional training images to the model. Image augmentation, thus, can boost the performance of DL models by introducing additional training data. In the Mask R-CNN model, it is possible to implement augmentation methods. Table 1 exhibits the augmentation methods that we used in our study.

Some augmentation methods (e.g., flipping) do not change the spectral distribution of the input images, whereas other methods (e.g., Gaussian noise) change the spectral distribution of the input images. Also, all the augmentation methods do not essentially improve the model performance, as we will see in the "Results" section.

Other than the single augmented methods, we have implemented combined augmented methods. For example, we have combined the salt and pepper noise and hue augmentation, saturation augmentation, and hue-saturation augmentation methods into a single pipeline and named it spectral augmentation to get the benefits of all the individual augmentation methods. We also used a sequential combination of the salt and pepper noise augmentation and the FlipLR augmentation method. The last augmentation method, named top 7, includes seven augmentation methods that appeared at the top when ranked by their performance. The performance assessment process is discussed in the section "Accuracy Assessment." Figure 3 lists some of the sample images, showing the effects of augmentation methods with respect to the original image.
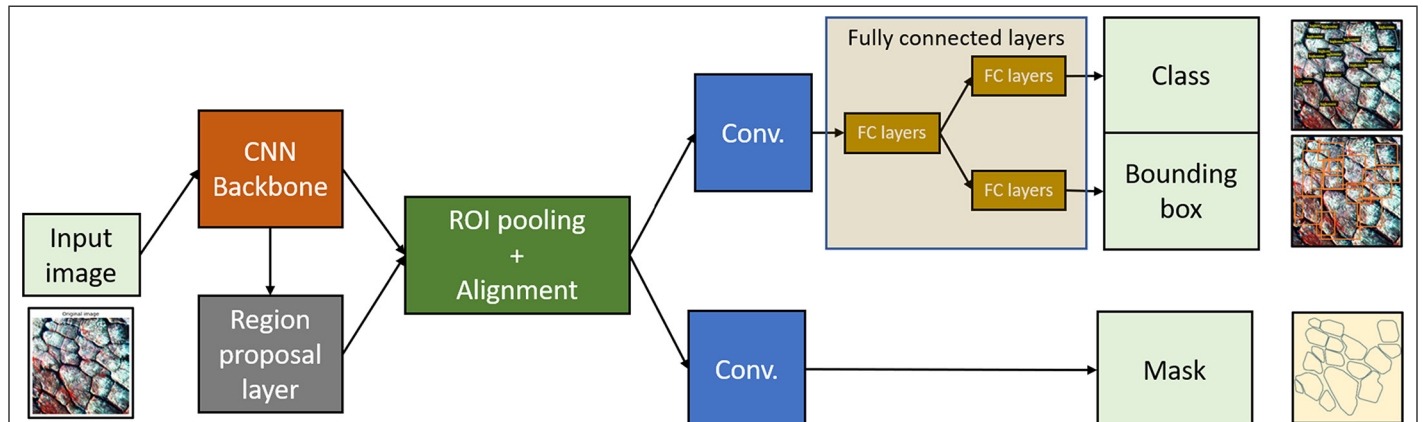

Figure 2. Simplified block diagram of the Mask R-CNN model.

Table 1. Augmentation methods used in this study.

Augmentation Type	Augmentation Methods	Description
Color space transformation	Hue	Multiplies the hue of images by random values
	Saturation	Multiplies the saturation of images by random values
	Hue saturation	Multiplies the hue and saturation of images by random values
	Invert	Subtracts all pixel values from 255
Geometric transformation	Crop	Generates smaller subimages from given full-sized input images
	Flip left to right (FlipLR)	Flips the image horizontally
	Flip up and down (FlipUD)	Flips the image vertically
	Flip left to right and up and down (FlipLRUD)	Combination of FlipLR and FlipUD
	Rotation (*x*)	Apply affine rotation of *x* degrees on the *y*-axis to input data
Noise injection	Gaussian noise	Adds noise sampled from Gaussian distributions
	Salt and pepper noise	Adds salt and pepper noise (noisy white-ish and black-ish pixels) to rectangular areas within the image
Mixed	Salt and pepper and FlipLR	A combination of salt and pepper noise and FlipLR method
	Spectral	A sequential combination of salt and pepper noise, hue, saturation, and hue-saturation augmentation methods
	Top 7 augmentations	A sequential combination of the top 7 augmentation methods based on their mean average precision score on the test data set (Figure 7d), including FlipLR, FlipUD, FlipLRUD, hue saturation, hue, saturation, and salt and pepper noise.

Model Dependency

Different tundra vegetation types exhibit distinct spectral, spatial, textural characteristics, which in turn decide the semantics of overlying IWPs (Liu *et al.* 2017). Landscape complexity translates to the image complexity, affecting DL model performances. Our idea was to implement separate models for separate tundra types and to study the model performance. To achieve this, we selected the best augmentation methods based on their performance and then trained separate models with separate training data sets, each of which will contain only one type of tundra. When the distribution of tundra types in our annotated data is compared to the entire Arctic, we see that our data have different distributions than the original Arctic (Figure 4). However, three of the major tundra types cover more than 70% of our sampled data set. Thus, we have prepared four tundra types named non–tussock sedge (G3), tussock sedge (G4), sedge/grass (W1), and other tundra types (Others).

Model Training

We used transfer learning approach to retrain the Mask R-CNN model. While doing so, we have taken the ResNet-50 as the CNN backbone of the model. The model was initially trained with the ImageNet data set. The training process was completed in a local machine with an Intel Core i9 CPU with NVIDIA GeForce RTX 2070 SUPER with 8 GB of GPU memory. The training time was not measured, as multiple training processes were run on the local machine at the same time, and based on the GPU load, the training time was varied.

After deciding the augmentation methods and the tundra types, we trained the Mask R-CNN model with minibatches (we changed the step size and batch size based on the memory available in the GPU),
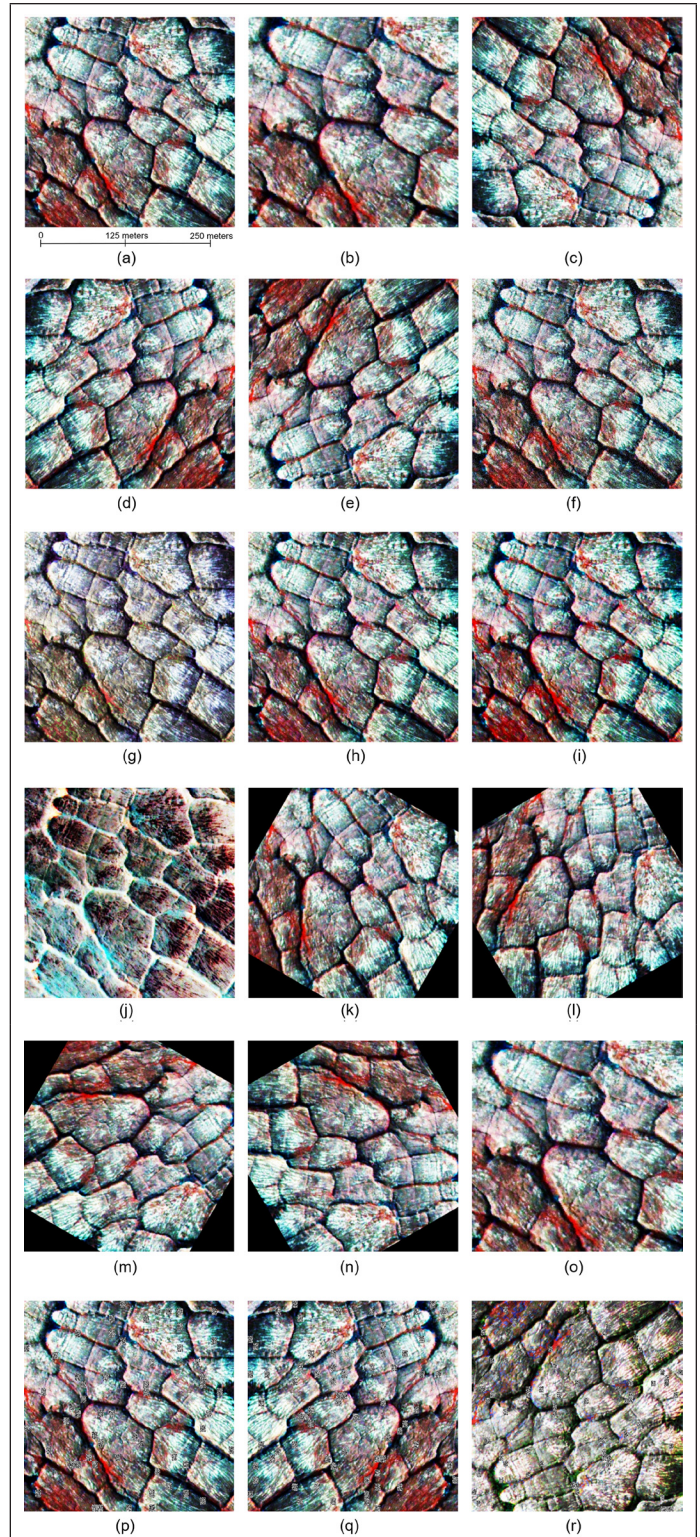
Figure 3. Zoomed-in views of an example original image and corresponding augmented images. (a) Original image. (b) Crop. (c) FlipLRUD (flip left to right and up and down). (d) FlipLR flip left to right. (e) FlipUD (flip up and down). (f) Gaussian noise. (g) Hue saturation. (h) Hue. (i) Saturation. (j) Invert. (k) Rotation (30). (l) Rotation (60). (m) Rotation (120). (n) Rotation (150). (o) Spectral. (p) Salt and pepper noise. (q) Salt and pepper and FlipLR. (r) Top 7 augmentations.
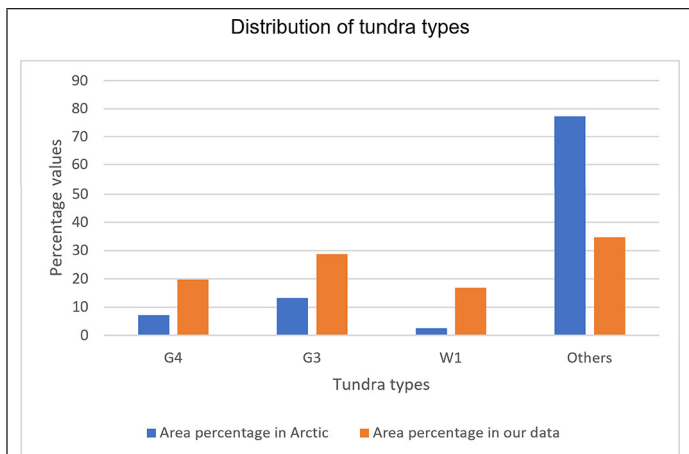
Figure 4. Percent distribution of tundra types, such as tussock sedge (G4), non–tussock sedge (G3), sedge/grass (W1), and other tundra types (Others) on the ground and in the training data. Percent distribution of tundra types on the ground was based on the Circumpolar Arctic Vegetation Map (Raynolds et al. 2019).

learning rate of 0.001, learning momentum of 0.9, and weight decay of 0.0001. We had a total of 487 training image tiles (11,151 low-centered polygons and 6404 high-centered polygons), 103 validation image tiles (2108 low-centered polygons and 1584 high-centered polygons), and 106 test image tiles (2108 low-centered polygons and 1584 high-centered polygons).

To optimize the model, we calculated different losses, such as (1) L1 loss (this defines box regression on object detection systems, which is less sensitive to outliers than other regression loss), (2) Mask R-CNN bounding box loss (this loss indicates the difference between predicted bounding box correction and true bounding box), (3) Mask R-CNN classifier loss (this loss estimates the difference of class labels between prediction and ground truth), (4) mask binary cross-entropy loss (this loss measures the performance of a classification model by observing predicted class and actual class), (5) RPN bounding box loss (this loss identifies the regression loss of bounding boxes only when there is object), and (6) RPN anchor classifier loss (this loss indicates the difference between the predicted RPN and actual closest ground-truth box to the anchor box). The total loss consists of the summation of all these loss values. We prepared the training and validation loss graphs for each of the augmentation methods (Figure 5, see next page) and for each of the tundra types (Figure 6). Based on these graphs, we have selected the best models for each of the augmentation methods or tundra types. In Figure 5, all the models converge at a point, but in Figure 6, the G3 tundra type seems to converge when trained for 200 epochs.
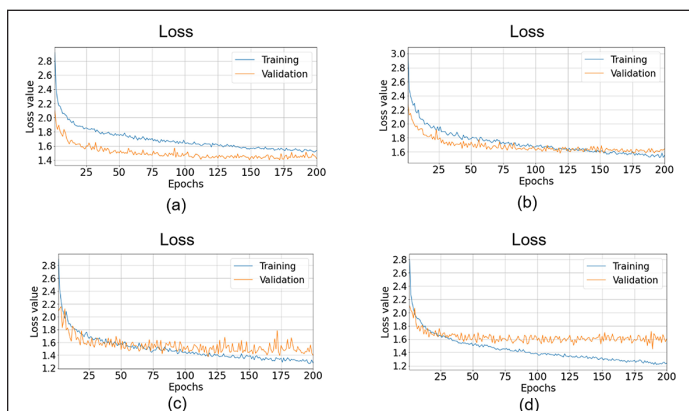

Figure 6. Loss plots for different tundra types: (a) Non–tussock sedge or G3. (b) Tussock sedge or G4. (c) Sedge/grass or W1. (d) Other tundra types.

Accuracy Assessment

We conducted a multistep accuracy assessment for the outputs. The outputs are in the form of class names and binary masks. We calculated the IoU for each of the polygons in the outputs that matched with the polygon classes in the test data set. We set a threshold of the IoU values as 0.5 and considered the polygons above this threshold as correctly classified.

We calculated precision, recall, and F1 score for each of the classes and for each of the images based on Equations 1–3:

$$\text{Precision} = \frac{\text{true positive}}{\text{true positive} + \text{false positive}} \quad (1)$$

$$\text{Recall} = \frac{\text{true positive}}{\text{true positive} + \text{false negative}} \quad (2)$$

$$F1 \text{ score} = \frac{2 \times \text{precision} \times \text{recall}}{\text{precision} + \text{recall}} \quad (3)$$

We then calculated the average precision, recall, and F1 score for low-centered and high-centered polygons. Finally, we calculated mean average precision and overall accuracy for each of the models based on Equations 4 and 5. Here, N is the number of total classes:

$$\text{Mean average precision} = \frac{1}{N} \sum_{K=1}^{N} \text{average precision for class } K \quad (4)$$

$$\text{Overall accuracy} = \frac{\text{true positive} + \text{true negative}}{\text{total predicted}} \quad (5)$$

Results and Discussion

Models with Different Augmentation Methods

After the model training step was completed, we calculated assessment values for each of the models (Figure 7). Some augmentation methods outperformed the model without any augmentation. However, some augmentation methods did not perform well, as expected. Choosing the best seven methods, we trained another model named the top 7 model and then calculated the assessment values for that model. Figure 7 shows that the top 7 model outperformed the individual models with a 79.6% mAP and 79.3% overall accuracy.

The rotation augmentation methods and the crop method did not perform well compared to other augmentation methods. When the images are cropped, the corners of the images are filled with zero values to match the input image size, and thus the image distribution is very much changed. This could be a reason why rotation methods did not improve the performance. Figure 8 depicts sample outputs from different augmentation methods. Detected polygons are marked in different colors. As we observed in the accuracy plots, certain augmentation methods outperformed in detecting the polygon boundaries.

Among the single augmentation methods, the FlipLR method performed the best; this method does not change the distribution of the input images. However, the salt and pepper noise method also performed well. Salt and pepper noise adds some black and white pixels randomly in the data. The amount of these pixels is not enough to change the distribution widely but is able to mimic digital noise in the image and makes the model robust against noise. As seen on the probability density function and the cumulative distribution function plots (Figure 9), the contributions of the salt and pepper noise in the higher and the lower ends of the possible pixel values are evident.

Models with Separate Tundra Types

We used our trained models on different tundra types and predicted for different tundra types. Table 2 shows the mean average precision for models trained on and predicted for different tundra types. These models performed better when trained and tested on the same tundra types. However, for the model trained on non–tussock sedge (G3) actually performed better on the sedge/grass (W1) tundra type. The reason
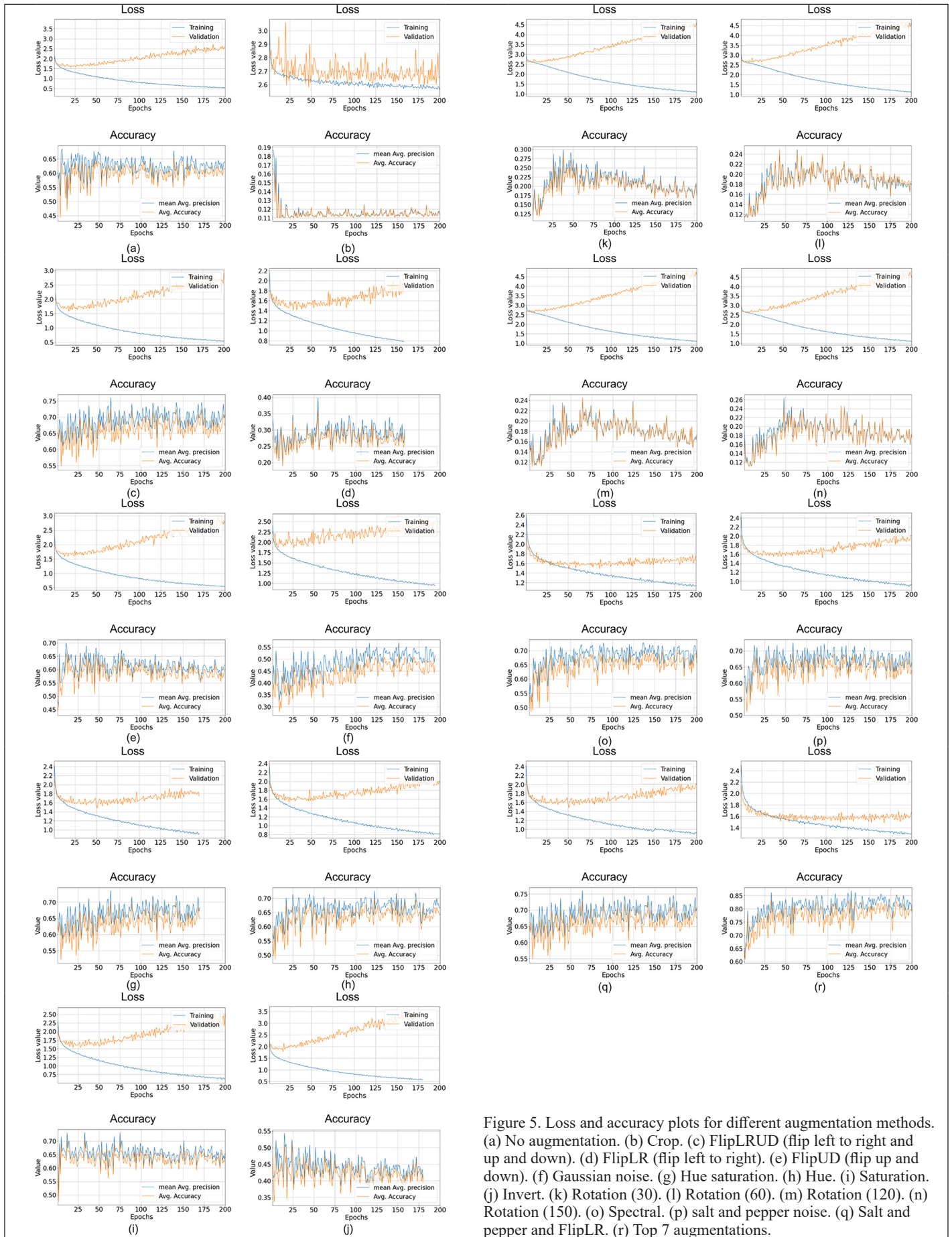
Figure 5. Loss and accuracy plots for different augmentation methods. (a) No augmentation. (b) Crop. (c) FlipLRUD (flip left to right and up and down). (d) FlipLR (flip left to right). (e) FlipUD (flip up and down). (f) Gaussian noise. (g) Hue saturation. (h) Hue. (i) Saturation. (j) Invert. (k) Rotation (30). (l) Rotation (60). (m) Rotation (120). (n) Rotation (150). (o) Spectral. (p) salt and pepper noise. (q) Salt and pepper and FlipLR. (r) Top 7 augmentations.

Figure 7. Performance analysis of augmentation methods. (a) Precision values for low-centered polygons (LCP) and high-centered polygons (HCP). (b) Recall values for LCP and HCP. (c) F1 score for LCP and HCP. (d) Mean average precision. (e) Accuracy. FlipLR = flip left to right; FlipUD = flip up and down; FlipLRUD = flip left to right and up and down).
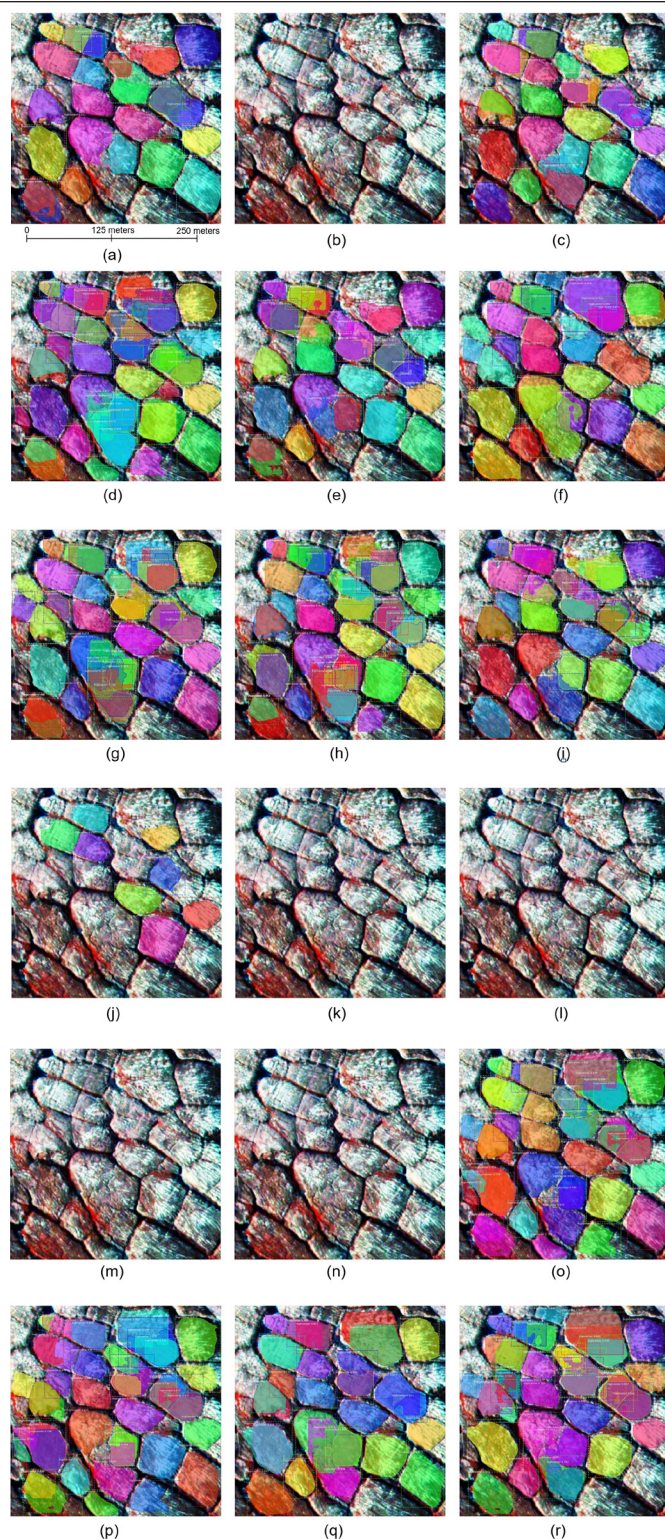
Figure 8. Sample outputs with different augmentation methods. (a) No augmentation. (b) Crop. (c) FlipLRUD (flip left to right and up and down). (d) FlipLR (flip left to right). (e) FlipUD (flip up and down). (f) Gaussian noise. (g) Hue saturation. (h) Hue. (i) Saturation. (j) Invert. (k) Rotation (30). (l) Rotation (60). (m) Rotation (120). (n) Rotation (150). (o) Spectral. (p) Salt and pepper noise. (q) Salt and pepper and FlipLR. (r) Top 7 augmentations.

Figure 9. Probability density function (PDF) and cumulative distribution function (CDF) for original image and salt and pepper noise augmented image.
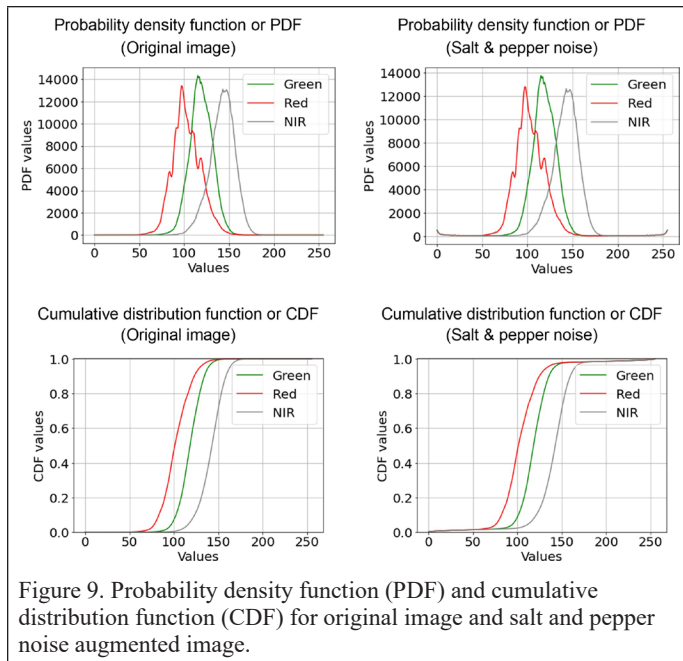
could be the similarity between these two types and the inadequate numbers of polygons of these tundra types.

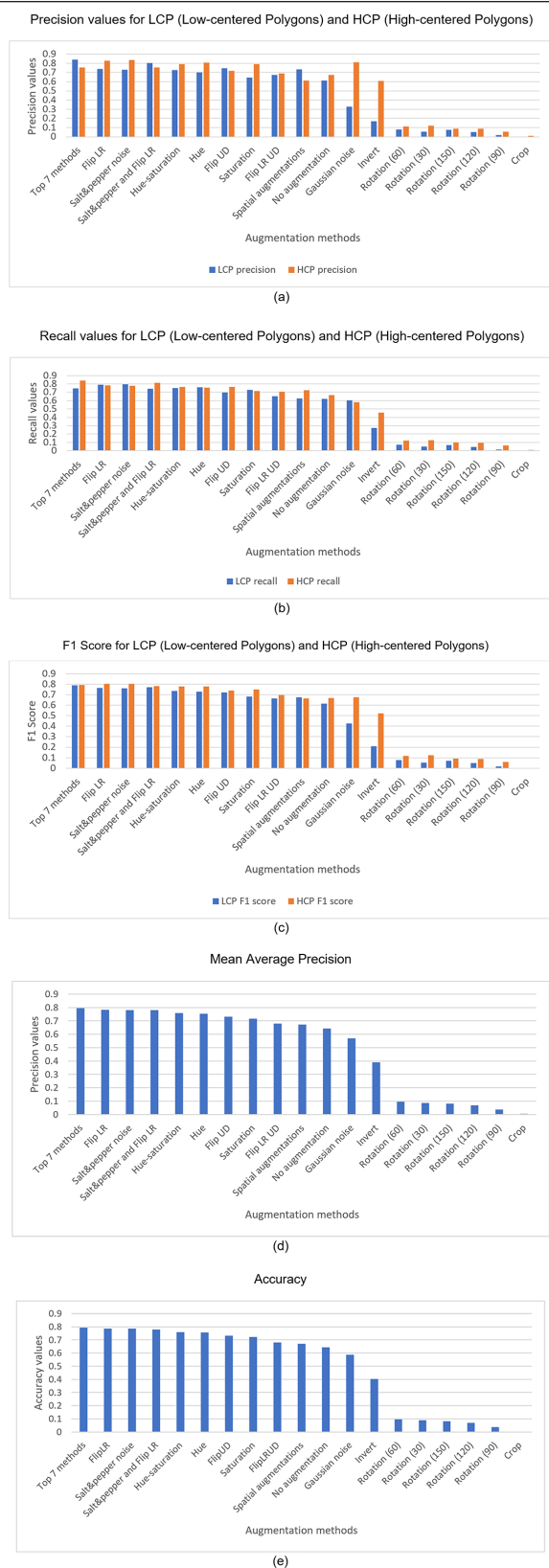Table 2. Mean average precision values for models trained on different tundra types: non–tussock sedge (G3), tussock sedge (G4), other tundra types, and sedge/grass (W1).

Mean Average Precision	G3	G4	Other Tundra Types	W1
G3	0.58	0.32	0.47	0.57
G4	0.08	0.79	0.18	0.05
Other tundra types	0.35	0.69	0.62	0.22
W1	0.75	0.35	0.54	0.8

We also predicted the overall accuracy values for the models trained and tested with different tundra types (Table 3). We observed that the models trained and tested on the same tundra types performed better. However, exceptions were found. For example, the model trained with the G3 tundra type performed the best with the W1 tundra type, and the model trained with the G4 tundra type performed the best with other tundra types. This calls for further analysis to better understand the underlying reasons linking the tundra types and model performances.

Table 3. Overall accuracy values for models trained on different tundra types: non–tussock sedge (G3), tussock sedge (G4), other tundra types, and sedge/grass (W1).

Overall Accuracy	G3	G4	Other Tundra Types	W1
G3	0.66	0.13	0.13	0.62
G4	0.08	0.66	0.66	0.05
Other tundra types	0.35	0.79	0.79	0.22
W1	0.75	0.36	0.36	0.8

Conclusion

Mapping IWPs from large satellite imagery requires a huge amount of computational resources as well as large volume of annotated images. We implemented the Mask R-CNN model for segmentation and classification of IWPs from commercially available satellite imagery. We have improved the model performance and found promising results by applying augmentation methods on top of the regular Mask R-CNN model. We explored an array of augmentation methods in the training process. Our results suggested that not all augmentation methods stand as favorable for improving prediction performance. We also trained separate Mask R-CNN models for separate tundra types. The lack of annotated data seems to be visible in the model performance when trained with separate tundra types. Our future research will further investigate the impact of augmentations methods on permafrost feature modeling efforts.

Acknowledgments

References

Arun Pandian, J., G. Geetharamani, and B. Annette. 2019. Data augmentation on plant leaf disease image dataset using image manipulation and deep learning techniques. Pages 199–204 in *Proceedings of the 2019 IEEE 9th International Conference on Advanced Computing, IACC 2019*. https://doi.org/10.1109/IACC48062.2019.8971580.

Bhuiyan, M. A. E., C. Witharana, and A. K. Liljedahl. 2020. Use of very high spatial resolution commercial satellite imagery and deep learning to automatically map ice-wedge polygons across tundra vegetation types. *Journal of Imaging* 6(12):137. https://doi.org/10.3390/JIMAGING6120137

Carvalho, O. O. de C. J.-R. Sensing, 2021. Instance segmentation for large, multi-channel remote sensing imagery using Mask-RCNN and a mosaicking approach. https://doi.org/10.3390/rs13010039.

Davidson, S. J., M. J. Santos, V. L. Sloan, J. D. Watts, G. K. Phoenix, W. C. Oechel, and D. Zona. 2016. Mapping Arctic tundra vegetation communities using field spectroscopy and multispectral satellite data in north Alaska, USA. *Remote Sensing* 8(12):978. https://doi.org/10.3390/RS8120978.

Elgendi, M., M. U. Nasir, Q. Tang, D. Smith, J.-P. Grenier, C. Batte, B. Spieler, W. D. Leslie, C. Menon, R. R. Fletcher, N. Howard, R. Ward, W. Parker, and S. Nicolaou. 2021. The effectiveness of image augmentation in deep learning networks for detecting COVID-19: A geometric transformation perspective. *Frontiers in Medicine* 8:629134. https://doi.org/10.3389/FMED.2021.629134.

Galdran, A., A. Alvarez-Gila, M. I. Meyer, C. L. Saratxaga, T. Araújo, E. Garrote, G. Aresta, P. Costa, A. M. Mendonça, and A. Campilho. 2017. Data-driven color augmentation techniques for deep skin image analysis. http://arxiv.org/abs/1703.03702

Grm, K., V. Struc, A. Artiges, M. Caron, and H. K. Ekenel. 2018. Strengths and weaknesses of deep learning models for face recognition against image degradations. *IET Biometrics* 7(1):81–89. https://doi.org/10.1049/iet-bmt.2017.0083.

He, K., G. Gkioxari, P. Dollár, and R. Girshick. 2017. Mask R-CNN. *IEEE Transactions on Pattern Analysis and Machine Intelligence* 42(2):386–397. https://arxiv.org/abs/1703.06870v3.

He, K., X. Zhang, S. Ren, and J. Sun. 2015. Deep residual learning for image recognition. Pages 770–778 in *Proceedings of the IEEE Computer Society Conference on Computer Vision and Pattern Recognition*, held in 2015. https://arxiv.org/abs/1512.03385v1.

Juutinen, S., T. Virtanen, 2017. Spatial variation and seasonal dynamics of leaf-area index in the arctic tundra-implications for linking ground observations and satellite images. https://doi.org/10.1088/1748-9326/aa7f85.

Karimov, A., A. Razumov, R. Manbatchurina, K. Simonova, I. Donets, A. Vlasova, Y. Khramtsova, and K. Ushenin. 2019. *Comparison of UNet, ENet, and BoxENet for Segmentation of Mast Cells in Scans of Histological Slices*.

Lara, M. J., A. D. McGuire, E. S. Euskirchen, H. Genet, S. Yi, R. Rutter, C. Iversen, V. Sloan, and S. D. Wullschleger. 2020. Local-scale Arctic tundra heterogeneity affects regional-scale carbon dynamics. *Nature Communications* 11(1):1–10. https://doi.org/10.1038/s41467-020-18768-z.

Lateef, F. and Y. Ruichek. 2019. Survey on semantic segmentation using deep learning techniques. *Neurocomputing* 338:321–348. https://doi.org/10.1016/J.NEUCOM.2019.02.003.

Leffingwell, E. de K. 1919. The Canning River region, northern Alaska. https://doi.org/10.3133/PP109.

Liljedahl, A. K., J. Boike, R. P. Daanen, A. N. Fedorov, G. V. Frost, G. Grosse, L. D. Hinzman, Y. Iijma, J. C. Jorgenson, N. Matveyeva, M. Necsoiu, M. K. Raynolds, V. E. Romanovsky, J. Schulla, K. D. Tape, D. A. Walker, C. J. Wilson, H. Yabuki, and D. Zona. 2016. Pan-Arctic ice-wedge degradation in warming permafrost and its influence on tundra hydrology. *Nature Geoscience* 9(4):312–318. https://doi.org/10.1038/NGEO2674.

Liu, N., P. Budkewitsch, and P. Treitz. 2017. Examining spectral reflectance features related to Arctic percent vegetation cover: Implications for hyperspectral remote sensing of Arctic tundra. *Remote Sensing of Environment* 192:58–72. https://doi.org/10.1016/J.RSE.2017.02.002.

Liu, Y. and L. Wu. 2016. Geological disaster recognition on optical remote sensing images using deep learning. *Procedia Computer Science* 91:566–575. https://doi.org/10.1016/j.procs.2016.07.144.

Long, Y., Y. Gong, Z. Xiao, and Q. Liu. 2017. Accurate object localization in remote sensing images based on convolutional neural networks. *IEEE Transactions on Geoscience and Remote Sensing* 55(5):2486–2498. https://doi.org/10.1109/TGRS.2016.2645610

Ma, L., Y. Liu, X. Zhang, Y. Ye, G. Yin, and B. A. Johnson. 2019. Deep learning in remote sensing applications: A meta-analysis and review. *ISPRS Journal of Photogrammetry and Remote Sensing* 152:166–177. https://doi.org/10.1016/J.ISPRSJPRS.2019.04.015.

Magnússon, R. Í., J. Limpens, J. van Huissteden, d. Kleijn, T. C. Maximov, R. Rotbarth, U. Sass-Klaassen, and M.M.P.D. Heijmans. 2020. Rapid vegetation succession and coupled permafrost dynamics in Arctic thaw ponds in the Siberian lowland tundra. *Journal of Geophysical Research: Biogeosciences* 125(7):e2019JG005618. https://doi.org/10.1029/2019JG005618.

Mahmoud, A., S. Mohamed, 2020. Object detection using adaptive mask RCNN in optical remote sensing images. *International Journal of Intelligent Engineering and Systems* 13(1). https://doi.org/10.22266/ijies2020.0229.07.

Mikola, J., T. Virtanen, M. Linkosalmi, E. Vähä, J. Nyman, O. Postanogova, A. Räsänen, D. Johan Kotze, T. Laurila, S. Juutinen, V. Kondratyev, and M. Aurela. 2018. Spatial variation and linkages of soil and vegetation in the Siberian Arctic tundra—Coupling field observations with remote sensing data. *Biogeosciences* 15(9):2781–2801. https://doi.org/10.5194/bg-15-2781-2018.

Paoletti, M. E., J. M. Haut, J. Plaza, and A. Plaza. 2019. Deep learning classifiers for hyperspectral imaging: A review. *ISPRS Journal of Photogrammetry and Remote Sensing* 158:279–317. https://doi.org/10.1016/J.ISPRSJPRS.2019.09.006.

Raynolds, M., D. Walker, A. Balser, 2019. A raster version of the Circumpolar Arctic Vegetation Map (CAVM). https://www.sciencedirect.com/science/article/pii/S0034425719303165.

Rizwan I Haque, I. and J. Neubert. 2020. Deep learning approaches to biomedical image segmentation. *Informatics in Medicine Unlocked* 18:100297. https://doi.org/10.1016/J.IMU.2020.100297.

Romero, A., C. Gatta, and G. Camps-Valls. 2016. Unsupervised deep feature extraction for remote sensing image classification. *IEEE Transactions on Geoscience and Remote Sensing* 54(3):1349–1362. https://doi.org/10.1109/TGRS.2015.2478379.

Shorten, C. and T. M.Khoshgoftaar. 2019. A survey on image data augmentation for deep learning. *Journal of Big Data* 6(1). https://doi.org/10.1186/S40537-019-0197-0.

Steedman, A., 2016. Spatio-temporal variation in high-centre polygons and ice-wedge melt ponds, Tuktoyaktuk coastlands, Northwest Territories. *Wiley Online Library* 28(1):66–78. https://doi.org/10.1002/ppp.1880.

Stow, D. A., B. H. Burns, and A. S. Hope. 1993. Spectral, spatial and temporal characteristics of arctic tundra reflectance. *International Journal of Remote Sensing* 14(13):2445–2462. https://doi.org/10.1080/01431169308904285.

Sturtevant, C., 2013. Spatial variation in landscape-level CO2 and CH4 fluxes from arctic coastal tundra: Influence from vegetation, wetness, and the thaw lake cycle. *Wiley Online Library* 19(9):2853–2866. https://doi.org/10.1111/gcb.12247.

Su, H., S. Wei, M. Yan, C. Wang, J. Shi, and X. Zhang. 2019. Object detection and instance segmentation in remote sensing imagery based on precise Mask R-CNN. *International Geoscience and Remote Sensing Symposium* 1454–1457. https://doi.org/10.1109/IGARSS.2019.8898573.

Verdonen, M., 2020. Periglacial vegetation dynamics in Arctic Russia: Decadal analysis of tundra regeneration on landslides with time series satellite imagery. https://doi.org/10.1088/1748-9326/abb500.

Waleed Abdulla. 2017. Mask R-CNN for object detection and instance segmentation on Keras and TensorFlow. GitHub Repository. https://github.com/matterport/Mask_RCNN.

Xie, F., M. Shi, Z. Shi, J. Yin, and D. Zhao. 2017. Multilevel cloud detection in remote sensing images based on deep learning. *IEEE Journal of Selected Topics in Applied Earth Observations and Remote Sensing* 10(8):3631–3640. https://doi.org/10.1109/JSTARS.2017.2686488.

Zabawa, L., A. Kicherer, L. Klingbeil, R. Töpfer, H. Kuhlmann, and R. Roscher. 2020. Counting of grapevine berries in images via semantic segmentation using convolutional neural networks. *ISPRS Journal of Photogrammetry and Remote Sensing* 164:73–83. https://doi.org/10.1016/j.isprsjprs.2020.04.002.

Zhang, C., I. Sargent, X. Pan, H. Li, A. Gardiner, J. Hare, and P. M. Atkinson. 2019. Joint deep learning for land cover and land use classification. *Remote Sensing of Environment* 221:173–187. https://doi.org/10.1016/J.RSE.2018.11.014.

Zhang, W., C. Witharana, A. Liljedahl, M.K.-R. Sensing, 2018. Deep convolutional neural networks for automated characterization of arctic ice-wedge polygons in very high spatial resolution aerial imagery. https://doi.org/10.3390/rs10091487.

Zhao, Z. Q., P. Zheng, S. T. Xu, and X. Wu. 2019. Object detection with deep learning: A review. *IEEE Transactions on Neural Networks and Learning Systems* 30(11):3212–3232. https://doi.org/10.1109/TNNLS.2018.2876865.

Zheng, J., X. Xu, G. Jia, and W. Wu. 2020. Understanding the spring phenology of Arctic tundra using multiple satellite data products and ground observations. *Science China Earth Sciences* 63(10):1599–1612. https://doi.org/10.1007/S11430-019-9644-8.

Zhong, L., L. Hu, and H. Zhou. 2019. Deep learning based multi-temporal crop classification. *Remote Sensing of Environment* 221:430–443. https://doi.org/10.1016/J.RSE.2018.11.032.

Zuo, L., P. He, C. Zhang, and Z. Zhang. 2020. A robust approach to reading recognition of pointer meters based on improved mask-RCNN. *Neurocomputing* 388:90–101. https://doi.org/10.1016/j.neucom.2020.01.032.

An Evaluation of Pan-Sharpening Methods for *SuperView-1* Satellite Imagery

Lei Zhang, Bowen Wen, Ming Zhang, Qiongqiong Lan, and Qian Wang

Abstract

*At present, little research focuses on the application of pan-sharpening methods to SuperView-1 satellite imagery. There is a lack of suitability assessment for existing pan-sharpening methods applied to SuperView-1 images. This study proposes an evaluation method that integrates visual evaluation, spectral analysis of typical objects, and quantitative indicators to evaluate the advantages of different pan-sharpening methods in different scenes of SuperView-1 imagery. Four scenes (urban areas, farmland, sparse vegetation, mixed surfaces) are selected to evaluate eight typical pan-sharpening methods (Brovey, principal component analysis (*PCA*), Gram-Schmidt (*GS*), band-dependent spatial-detail (*BDSD*), high-pass filtering (*HPF*), smoothing filter-based intensity modulation (*SFIM*), modulation transfer function-generalized Laplacian pyramid (*MTF-GLP*), MTF-GLP-high pass modulation (*MTF-GLP-HPM*). The results show that the suitability of each pan-sharpening method is different in various scenes.* PCA, *Brovey, and* GS *distort the spectral information greatly, and the stability of the pan-sharpening results in different scenes which are poor.* BDSD *has strong stability and can better balance the relationship between spectral distortion and spatial distortion in different scenes. The multi-resolution analysis method has better applicability and stability for SuperView-1 imagery, among which* MTF-GLP *and* MTF-GLP-HPM *perform better in the pan-sharpening results. This study provides a reference for the selection of pan-sharpening methods for SuperView-1 imagery in different application fields.*

Introduction

The rapid development of optical sensing technology has brought abundant remote sensing data with increasing resolution. Due to the constraint between spatial resolution and spectral resolution, the spatial resolution of multispectral images (MS) in satellite data is lower than that of panchromatic images (PAN). Pan-sharpening technology can fuse multispectral and panchromatic images in the same scene to generate high-resolution multispectral images. The fused image not only retains rich spectral information, but also highlights more spatial details. Vivone *et al.* (2021) analyzed in detail the latest developments in MS pan-sharpening (Vivone *et al.* 2021). Javan *et al.* (2021) reviewed 41 pan-sharpening methods and applied them to high-resolution images for testing and comparison (Javan *et al.* 2021). Meng *et al.* (2019) provided a comprehensive review of pan-sharpening methods, and evaluated existing methods based on meta-analysis (Meng *et al.* 2019). Vivone *et al.* (2015) described and extensively compared some of the most advanced pan-sharpening methods (Vivone *et al.* 2015).

Lei Zhang is with the School of Remote Sensing and Information Engineering, Wuhan University, Wuhan 430079, China.

Bowen Wen and Ming Zhang are with the School of Resources and Environmental Engineering, Wuhan University of Technology, Wuhan 430070, China (zhangming_88@whut.edu.cn).

Qiongqiong Lan is with the China Centre for Resources Satellite Data and Application, Beijing 100094, China.

Qian Wang is with the School of Geographic and Environmental Sciences, Tianjin Normal University, Tianjin 300387, China.

Ghassemian (2016) reviewed pixel-level pan-sharpening methods and discussed the assessment of fused results (Ghassemian 2016). Pan-sharpening methods realize the complementary advantages of different imagery, satisfy the ever-evolving application requirements, and play an important role in application fields such as image recognition and classification (Yuhendra *et al.* 2011).

Currently, pan-sharpening methods can be classified into three categories: component substitution (CS), multi-resolution analysis (MRA), and model-based methods (Vivone *et al.* 2021). The CS methods extract the component that determines the spatial resolution of the multispectral image and improve the resolution of the multispectral image by replacing this component with the panchromatic image. The classic CS methods include Brovey (Dong *et al.* 2021; Mandhare *et al.* 2013; Sarp 2014), Principal Component Analysis (PCA) (Ghadjati *et al.* 2019; Tambe *et al.* 2021; Wang *et al.* 2016), Gram-Schmidt (GS) (Candra 2013; Tabib Mahmoudi and Karami 2020; Yilmaz *et al.* 2020), Band-Dependent Spatial-Detail (BDSD) (Imani 2018; Vivone 2019; Zhong *et al.* 2017), etc. The CS methods are easy to implement, but the fusion results have the problem of spectral distortion. Wang *et al.* (2014) used the particle swarm optimization model to propose a new pan-sharpening method based on adaptive component substitution (Wang *et al.* 2014). Li *et al.* (2020) improved the component substitution pan-sharpening method by refining the spatial detail (Li *et al.* 2020). The MRA methods perform image transformation on the multi-source images, extract the spatial detail from the panchromatic image, and add it to the multispectral image to obtain the fused image. The classic MRA methods include High-Pass Filtering (HPF) (Gangkofner *et al.* 2007; Metwalli *et al.* 2010; Pushparaj and Hedge 2017), Smoothing Filter-Based Intensity Modulation (SFIM) (Alcaras *et al.* 2021; Liu 2000), modulation transfer function -generalized Laplacian pyramid (MTF-GLP) (Aiazzi *et al.* 2006), MTF-GLP with high pass modulation (MTF-GLP-HPM) (Lee and Lee 2009), etc. The MRA methods can better control the spectral distortion. The model-based methods assume that the low-resolution multispectral image is obtained from high-resolution multispectral image through down-sampling or other operations. They establish the relationship model between high-resolution multispectral image and low-resolution multispectral image and panchromatic image, express the model with energy functional, and then obtain the fused image by optimizing the model. Wang *et al.* (2019) proposed a regularized model-based pan-sharpening method to reduce the impact of local dissimilarities (Wang *et al.* 2019). Guo *et al.* (2020) developed a new model-based pan-sharpening method based on Bayesian theory (Guo *et al.* 2020). The model-based methods have high spectral fidelity, but their computational complexity leads to unsatisfactory time efficiency.

Most scholars used quantitative indicators to evaluate the fusion results of pan-sharpening methods. Commonly used quantitative indicators include Spectral Angle Mapper (SAM) (Alparone *et al.* 2008; Pandit and Bhiwani 2015), Erreur Relative Globale Adimensionnelle de Synthese (ERGAS) (Alparone *et al.* 2008; Pandit and Bhiwani 2015), Spatial Correlation Coefficient (SCC) (Pushparaj and Hegde 2017),

average gradient (AG) (Haddadpour *et al.* 2017), Quality with No Reference (QNR) (Alparone *et al.* 2008; Pandit and Bhiwani 2015), etc. However, the existing evaluation methods ignore the importance of typical objects recognition in different scenes of satellite images. Due to different spectral and spatial characteristics of objects, the performances of the same pan-sharpening method in different scenes are different. Thus it is necessary to analyze the applicability of the pan-sharpening method for various scenes in specific satellite images. This study proposes an evaluation method that integrates visual evaluation, spectral analysis of typical objects, and quantitative indicators to evaluate the advantages of different pan-sharpening methods in different scenes of satellite imagery.

SuperView-1 satellite launched in 2016 is currently the commercial remote sensing satellite with the highest resolution in China (Liu *et al.* 2020). It provides imaging products with 0.5 m panchromatic and 2 m multispectral bands. The imagery shows fine details of the ground objects, which is of great significance for applications in surveying and mapping, natural resources, environmental monitoring, etc. However, little research has studied the applicability of the pan-sharpening methods for this satellite imagery. Using *SuperView-1* imagery as the data source, this study analyzes and evaluates the performances of eight typical pan-sharpening methods in different scenes of the *SuperView-1* images. The purpose of this paper is to explore the applicability differences of typical fusion methods in different scenes of *SuperView-1* images, and to provide a scientific reference for the remote sensing application of *SuperView-1* data.

Methodology

Fusion Methods

This paper selects the classical CS methods of Brovey, PCA, GS, BDSD, and the MRA methods of HPF, SFIM, MTF-GLP, and MTF-GLP-HPM for comparative analysis. Model-based pan-sharpening methods are not involved in this study.

The Brovey method treats multispectral image as chrominance components, and panchromatic image as luminance components. After the two images are normalized, the fused image is obtained through arithmetic operation.

PCA performs forward PCA on the multispectral image to obtain several principal components. The panchromatic image undergoes histogram equalization and replaces the first principal component. The inverse PCA is applied to all components to obtain the fused image (Naidu and Raol 2008).

Gram–Schmidt orthogonalization transformation is applied on the multispectral image and a panchromatic band that is simulated from multispectral image. Here, the simulated band is regarded as the first band. Then the panchromatic image replaces the first Gram–Schmidt band. The inverse Gram–Schmidt transform is applied to obtain the fused image (Karathanassi *et al.* 2007).

BDSD assumes that there is a linear relationship between the various bands of the multispectral image and the panchromatic image. BDSD uses the modulation transfer function (MTF) to perform low-pass filtering on bands to solve the coefficient matrix. Based on the assumption of coefficient invariance, the relationship coefficient is applied to the original resolution image and the fused image (Garzelli *et al.* 2007; Vivone 2019).

HPF first obtains the spatial information of the panchromatic image through a high-pass filter operator, and then superimposes the spatial information on the multispectral image to achieve the fused image.

SFIM matches the panchromatic image with each band of the multispectral image. Mean filtering is applied to the matched panchromatic image, and then ratio operation is performed on the filtered and unfiltered image to obtain the spatial information of the image. Finally, the spatial information is injected into the multispectral image by the multiplication model to obtain the fused image.

MTF-GLP first matches the bands of panchromatic and multispectral images, determines the low-pass filter according to the MTF, and builds the Generalized Laplacian Pyramid (GLP) to extract high frequency information of panchromatic image. Finally, the high frequency information is directly added to the multispectral image to obtain the fused image. Based on the MTF-GLP method, MTF-GLP-HPM injects spatial information into the multispectral image by multiplicative injection model to obtain the fused image. The comparison of these eight methods is shown in Table 1.

Evaluation Methods

This study proposes an evaluation method that includes three aspects: visual evaluation, spectral analysis of typical objects, and quantitative indicators.

Visual Evaluation

Since image quality cannot be separated from the intuitive experience of the human visual system, visual evaluation can quickly and

Table 1. The comparison of eight pan-sharpening methods.

Fusion Methods	Advantages	Disadvantages	Application
Brovey	Simple and efficient for fast interactive processing (Liu 2000).	Spectral distortion is uncontrolled and hard to quantify (Liu 2000).	urban and suburban area
Principal component analysis (PCA)	Simple to operate, merge all the bands at the same time (Chavez *et al.* 1991).	Rely on the spectral overlap of panchromatic and multispectral images, which is prone to spectral distortion (Aiazzi *et al.* 2006).	urban and suburban area, farmland area
Gram-Schmidt (GS)	Maintain the spectral information of the original multispectral image, no limitation on the number of bands.	Performance degradation when the number of bands increases (Vivone *et al.* 2015).	urban and suburban area
Band-dependent spatial-detail (BDSD)	Optimal at full scale, minimizes the squared error between the multispectral image and the fusion result (Garzelli *et al.* 2007).	Typically show a higher spectral distortion than the MTF-based method (Vivone *et al.* 2015).	urban and suburban area
High-pass filtering (HPF)	Maintain the spectral characteristics of the multispectral image, simple and computationally small (Chavez *et al.* 1991).	Ringing effect caused by the spatial filter at high contrast boundaries (Chavez *et al.* 1991).	farmland area, urban area
Smoothing filter-based intensity modulation (SFIM)	Retain the spectral properties and contrast of multispectral image (Liu 2000).	Sensitive to image co-registration accuracy (Liu 2000).	mountainous area, urban area
Modulation transfer function-generalized Laplacian pyramid (MTF-GLP)	Yield sharper and cleaner geometrical structures (Aiazzi *et al.* 2006).	Not suitable for critically subsampled multispectral images (Aiazzi *et al.* 2006).	urban and suburban area
MTF-GLP-high pass modulation (MTF-GLP-HPM)	Retain spatial details and use a postprocessing technique to correct color distortion (Lee and Lee 2009).	The filtering phase significantly slows down the algorithms (Vivone *et al.* 2015).	urban and suburban area

effectively evaluate the clarity, texture details, and color changes of the fused image. Visual evaluation is based on the sensitivity of the human eye to the visual perception of the image and the professional knowledge of the evaluator to make a judgment on the quality of the image. In this paper, the criteria for visual evaluation are shown in Table 2.

This study selects four different scenes (urban areas, farmland, sparse vegetation, mixed surfaces) in multispectral images for visual assessment of fusion results. The urban areas scene is mostly regular-shaped buildings, as well as a small part of rivers and roads. The farmland scene contains lots of neatly arranged farmland and a few buildings. The sparse vegetation scene is a vegetation area with fewer types of land covers. Mixed surfaces scene includes buildings, roads, vegetation, and water bodies, and their shapes are not uniform and relatively irregular.

Table 2. The criteria for visual evaluation.

Content	Explanation	Evaluation Standard	Quality Scale
Color characteristics	The difference between the color of the fused image and the color of the original multispectral image	Basically no color change in the image	Good
		Slight difference in image color	Fair
		Severely distorted image color	Bad
Edge feature	The sharpness of object contours and edges in the fused image	Clear contours and edges	Good
		Slight double shadow phenomenon	Fair
		Severe false contour phenomenon	Bad

Spectral Analysis of Typical Objects

Different scenes contain various objects with different spectral characteristics. The degree of spectral distortion caused by the pan-sharpening method for different objects is also different. Specific applications such as target recognition and classification often rely on the accurate spectral information of the objects, which requires the fused image to maintain the spectral characteristics of the original multispectral image as much as possible. Therefore, the spectral distortion of typical objects in different scenes in the fused image can be used to evaluate the fusion result.

In this study, four types of objects are selected for spectral analysis of typical objects, including vegetation, buildings, water bodies, and roads. 30 pure pixels are selected for each object, and the average value of pure pixels is used as the spectral feature of the object. The spectral distortion of the object is defined as root-mean-square error (RMSE) between the fused image and the original multispectral image.

Quantitative Indicators

This study selects five quantitative indicators for the assessment of fusion results, including SAM, ERGAS, SCC, AG, and QNR.

SAM calculates the angle of the corresponding pixels between the fused image and the reference image. The smaller the value, the lower the spectral distortion rate and the higher the quality of the fused image.

$$\text{SAM} = \arccos\left(\frac{v,v'}{v^2 v'^2}\right) \tag{1}$$

where, v represents pixel set of the fused image, and v' represents pixel set of the reference image.

ERGAS reflects the overall quality of the fused image. The smaller the value, the higher the quality of the fused image.

$$\text{ERGAS} \triangleq 100 \frac{P_f}{P_s} \sqrt{\frac{1}{B} \sum_{i=1}^{B} \frac{\text{RMSE}_i^2}{\text{MEAN}_i^2}} \tag{2}$$

where, P_f represents the resolution of the panchromatic image, P_s represents the resolution of the multispectral image, B represents the number of multispectral image bands, MEAN_i represents the mean value of the ith band, and RMSE_i represents the root-mean-square error of the ith band between the fused image and the reference image.

SCC is determined by the correlation coefficient between the reference MS image and the fused image. Specifically, the Laplacian filter is used to perform high-pass filtering on the reference MS image, and then the correlation coefficient between high frequencies is calculated. The higher the value, the higher the degree of correlation, that is, the more spatial information is added to the fused image.

AG reflects the sharpening effect and spatial details of the image; that is, the ability of the image to express the contrast of small details. The larger the value, the clearer the image.

$$\text{AG} = \frac{1}{MN} \sum_{i=1}^{M} \sum_{j=1}^{N} \sqrt{\Delta xF(x,y)^2 + \Delta yF(x,y)^2} \tag{3}$$

where, M and N are the length and width of the image, and $\Delta xF(x, y)$ and $\Delta yF(x, y)$ are the difference of the image $F(x, y)$ along the x and y directions, respectively.

QNR is a nonreference image evaluation index that directly calculates the covariance between different bands. It is used to describe the difference in image similarity, mean and contrast. The higher the QNR index, the better the quality of the fused product.

The application of quantitative indicators is shown in Table 3.

Table 3. The application of quantitative indicators.

Quantitative Indicators	Application
Spectral Angle Mapper (SAM)	Measure the spectral distortion
Erreur Relative Globale Adimensionnelle de Synthese (ERGAS)	Represent the overall quality
Spatial Correlation Coefficient (SCC)	Represent the degree of correlation
average gradient (AG)	Reflect the clarity of the image
Quality with No Reference (QNR)	Account for both spectral distortion and spatial distortion

Experiments and Results

Data Sets

The *SuperView-1* satellite is a high-resolution commercial remote sensing satellite independently developed by China. The *SuperView-1* 01/02 satellite was successfully launched at the Taiyuan Satellite Launch Center on 28 December 2016. The *SuperView-1* 03/04 satellite was successfully launched on 9 January 2018. The four-star network of *SuperView-1* can realize one-day revisit for any point on Earth, marking the first step of China's fully autonomous commercial operation of remote sensing satellite. The *SuperView-1* has a panchromatic band with a spatial resolution of 0.5 m, four multi-spectral bands of blue, green, red, and near-infrared at 2.0 m spatial resolution, with orbital altitude of 530 km and width of 12 km. The experimental data sets come from the *SuperView-1* satellite. The size of the multispectral image (MS) is 512 pixels × 512 pixels, and the PAN is 2048 pixels × 2048 pixels. This study selected multispectral images of four different scenes (urban areas, farmland, sparse vegetation, mixed surfaces), as shown in Figure 1. Among them, the sparse vegetation is a false-color composite image with fewer types of land covers. Red represents vegetation and the background is mountainous. In order to better show the scene details, the white box area is selected to display the fusion results. This study selects *SuperView-1* images with appropriate temporal information according to the image quality of the four scenes. Since image quality is one of the important factors affecting pan-sharpening, the temporal information of each selected image is determined by the image quality of the scene. The temporal information and geographic location of each scene in this paper is shown in the Table 4.
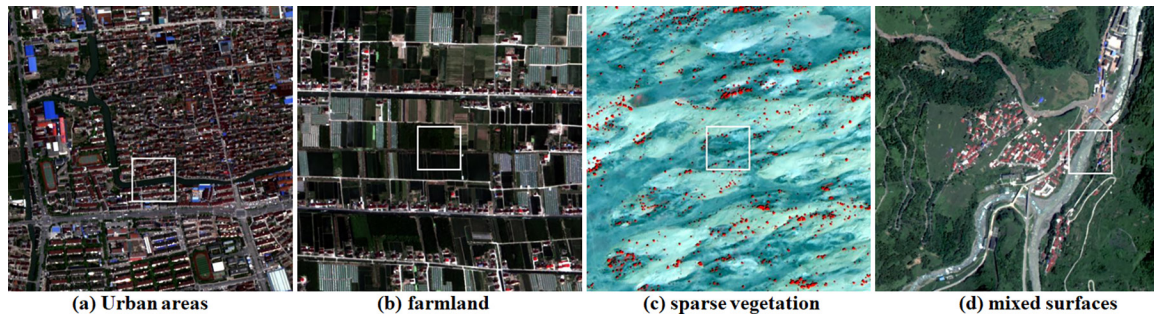
(a) Urban areas   **(b) farmland**   **(c) sparse vegetation**   **(d) mixed surfaces**

Figure 1. Multispectral images of SuperView-1.

Table 4. The temporal information and geographic location of four scenes.

Scenes	Satellite	Temporal Information	Geographic Location
Urban Areas	*SuperView-1* 02	2019.5.03	Fengxian District, Shanghai
Farmland	*SuperView-1* 01	2019.7.30	Pudong New Area, Shanghai
Sparse Vegetation	*SuperView-1* 02	2017.6.27	Xiwuzhumuqin Banner, Xilingol League, Inner Mongolia Autonomous Region
Mixed Surfaces	*SuperView-1* 02	2019.8.16	Ebian Yi Autonomous County, Leshan, Sichuan

(a) MS   **(b) PAN**   **(c) Brovey**   **(d) PCA**   **(e) GS**

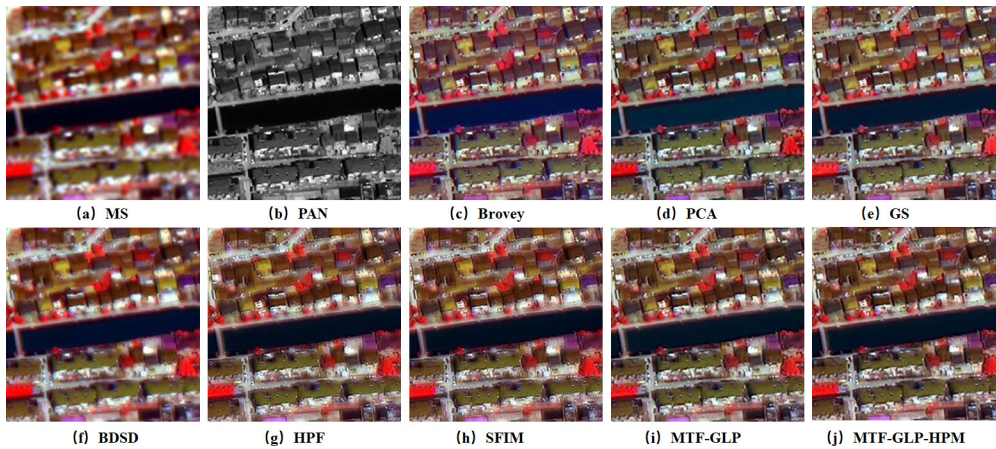**(f) BDSD**   **(g) HPF**   **(h) SFIM**   **(i) MTF-GLP**   **(j) MTF-GLP-HPM**

Figure 2. Comparison of fusion results in urban areas. MS = multispectral images; PAN = panchromatic images; PCA = principal component analysis; GS = Gram-Schmidt; BDSD = band-dependent spatial-detail; HPF = high-pass filtering; SFIM = smoothing filter-based intensity modulation; MTF-GLP = modulation transfer function-generalized Laplacian pyramid; MTF-GLP-HPM: MTF-GLP-high pass modulation.

(a) MS   **(b) PAN**   **(c) Brovey**   **(d) PCA**   **(e) GS**

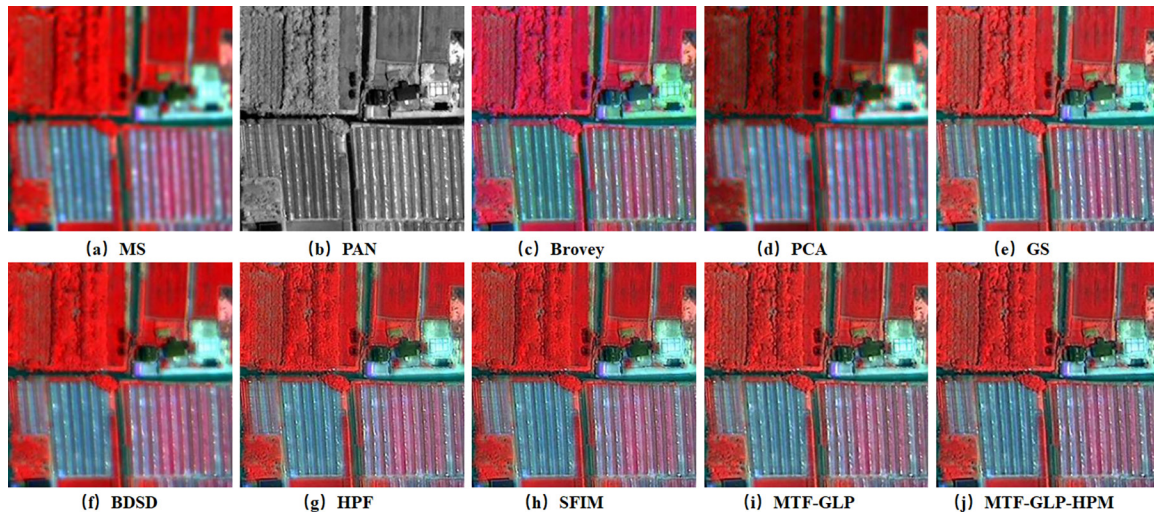**(f) BDSD**   **(g) HPF**   **(h) SFIM**   **(i) MTF-GLP**   **(j) MTF-GLP-HPM**

Figure 3. Comparison of fusion results in farmland. MS = multispectral images; PAN = panchromatic images; PCA = principal component analysis; GS = Gram-Schmidt; BDSD = band-dependent spatial-detail; HPF = high-pass filtering; SFIM = smoothing filter-based intensity modulation; MTF-GLP = modulation transfer function-generalized Laplacian pyramid; MTF-GLP-HPM: MTF-GLP-high pass modulation.

Visual Evaluation

Figure 2 shows the comparison of MS, PAN, and fused images obtained by eight fusion algorithms in urban areas. Figure 3 shows the comparison of MS, PAN, and fused images obtained by eight fusion algorithms in farmland. Figure 4 shows the comparison of MS, PAN, and fused images obtained by eight fusion algorithms in sparse vegetation. Figure 5 shows the comparison of MS, PAN, and fused images obtained by eight fusion algorithms in mixed surfaces.

It can be seen that the fused images based on Brovey and GS greatly improve the spatial quality of MS, and can clearly retain the edge details of the ground objects and the high-frequency information of the images. However, the fused images based on Brovey have spectral distortion, which is mainly manifested as blueish green farmland and purplish sparse vegetation. The PCA-based fusion images have more spectral distortion and blurry edges, and the sharpening effect is not obvious. The fused images based on BDSD have spectral fidelity equivalent to that of MRA algorithms, but they are not as good as Brovey and GS for the enhancement of spatial quality because the fused images are slightly blurred. Fused images based on HPF, SFIM, MTF-GLP, and MTF-GLP-HPM have roughly the same performance in maintaining the spectral information of ground objects, and the spectral distortion is relatively small. In urban areas, MTF-GLP and MTF-GLP-HPM can enhance spatial quality of images better than HPF and SFIM algorithms. In mixed surfaces, the fusion results based on HPF and MTF-GLP are better, and green noise appears on the edges of the ground objects in the fused images based on SFIM and MTF-GLP-HPM.

Spectral Distortion of Typical Objects

A *SuperView-1* image has a high spatial resolution and a large number of pure pixels, which is suitable for spectral analysis of typical objects in different scenes. Figure 6 shows the degree of spectral distortion of different objects. The colored solid dots represent the lowest degree of spectral distortion in each scene.

PCA algorithm basically causes the largest spectral distortion in all scenes, and the distortion mainly comes from the near-infrared band, while the visible light band has a smaller degree of distortion. Therefore, the color effect of the fused image based on PCA is visually the same as the original multispectral image. However, when comparing the road in the urban area with the road in the mixed surfaces in the fused image, it is not difficult to find that the spectral distortion caused by PCA in the urban area is much smaller than that in the mixed surfaces. The results of Brovey and GS algorithms in different scenes are more different. The spectral distortions of other algorithms on the buildings in the urban areas and mixed surfaces are increased, while
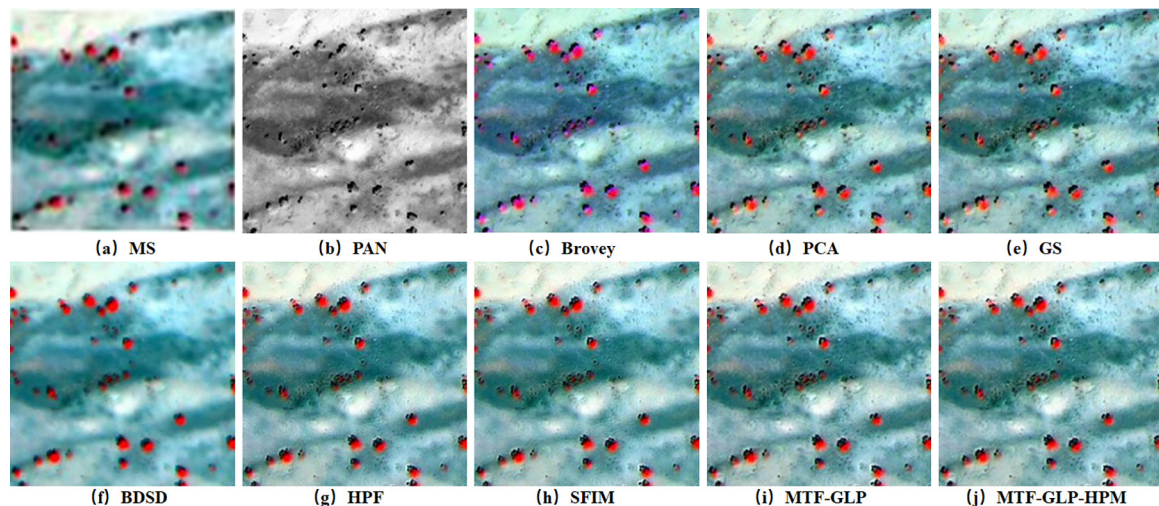

Figure 4. Comparison of fusion results in sparse vegetation. MS = multispectral images; PAN = panchromatic images; PCA = principal component analysis; GS = Gram-Schmidt; BDSD = band-dependent spatial-detail; HPF = high-pass filtering; SFIM = smoothing filter-based intensity modulation; MTF-GLP = modulation transfer function-generalized Laplacian pyramid; MTF-GLP-HPM: MTF-GLP-high pass modulation.
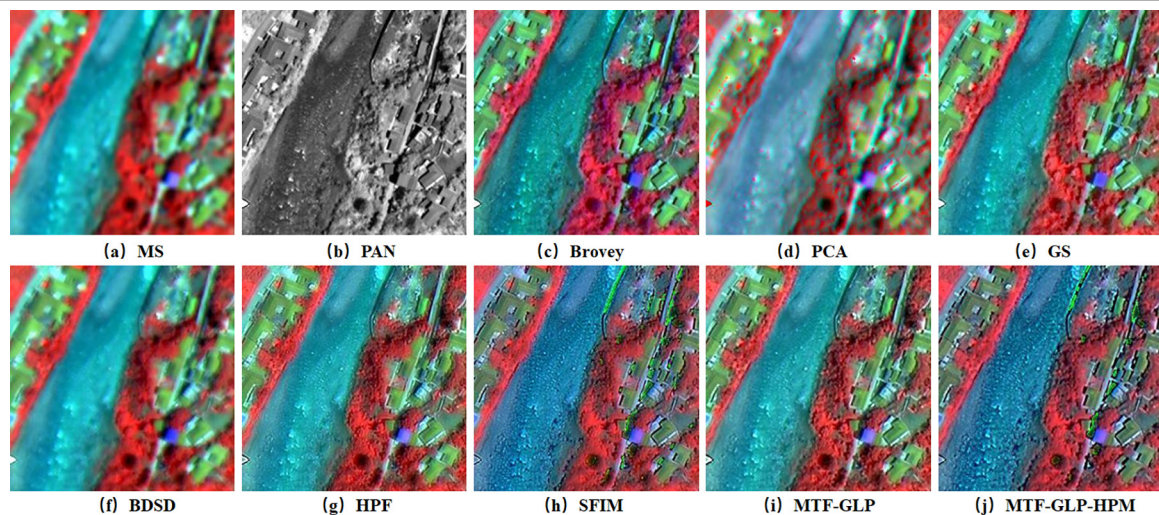

Figure 5. Comparison of fusion results in mixed surfaces. MS = multispectral images; PAN = panchromatic images; PCA = principal component analysis; GS = Gram-Schmidt; BDSD = band-dependent spatial-detail; HPF = high-pass filtering; SFIM = smoothing filter-based intensity modulation; MTF-GLP = modulation transfer function-generalized Laplacian pyramid; MTF-GLP-HPM: MTF-GLP-high pass modulation.

the Brovey and GS algorithms appear to be significantly reduced. The BDSD algorithm has little change in the spectral distortion of ground objects in different scenes, and the spectral distortion is always at an intermediate level. Compared with the component substitution methods, the other four multi-resolution analysis algorithms have a lower degree of spectral distortion, which is consistent with the visual evaluation. However, in each scene, HPF and SFIM are slightly better than MTF-GLP and MTF-GLP-HPM in maintaining the spectral characteristics of typical objects.

Quantitative Evaluation

The SAM and SCC of Brovey and GS in the mixed surfaces have improved greatly, but the effects in the other three scenes are not outstanding. The BDSD always has the highest QNR index in scenes outside of sparse vegetation, indicating that it can find a better balance between spectral distortion and spatial distortion.

In the sparse vegetation, due to the lack of high-frequency information in the image and the inability of the CS method to enhance the spatial details, the indicators of the MRA algorithm are always better than the CS algorithms, and the results of the HPF algorithm are the best.

In most cases, MTF-GLP and MTF-GLP-HPM have better performance in SAM, ERGAS, SCC, and AG indicators. While maintaining the original image spectral information, they significantly improve the spatial quality of the fused image.

Conclusions

In this paper, eight pan-sharpening methods are used to conduct fusion experiments on *SuperView-1* satellite imagery in four different scenes, and subjective and objective evaluation methods are used to evaluate the fusion results. The main conclusions are as follows:

(1) These eight fusion algorithms have different degrees of improvement in the quality of *SuperView-1* images, and each has its own advantages and disadvantages. Among them, the Brovey and GS algorithms can significantly enhance the spatial characteristics and clarity of the images, but they damage the spectral information of the objects. BDSD algorithm has strong stability and can better balance spectral distortion and spatial distortion, but the sharpness of the images is weaker than other algorithms. The four MRA algorithms can maintain the spectral information of objects, and the MTF-GLP and MTF-GLP-HPM algorithms are generally better than HPF and SFIM algorithms.

(2) The MRA method has basically the same applicability in different scenes and can better retain the spectral information of the image. The CS method is sensitive to the composition of objects in the scene. Therefore, the MRA methods have better applicability and stability for the pan-sharpening of *SuperView-1* images, and the MTF-GLP and MTF-GLP-HPM algorithms have the best performance.

(3) PCA, Brovey, and GS algorithms have different performances in different scenes, which are mainly reflected in the different degrees of spectral distortion of typical objects. When using a *SuperView-1* image to perform pan-sharpening, the algorithm with the best
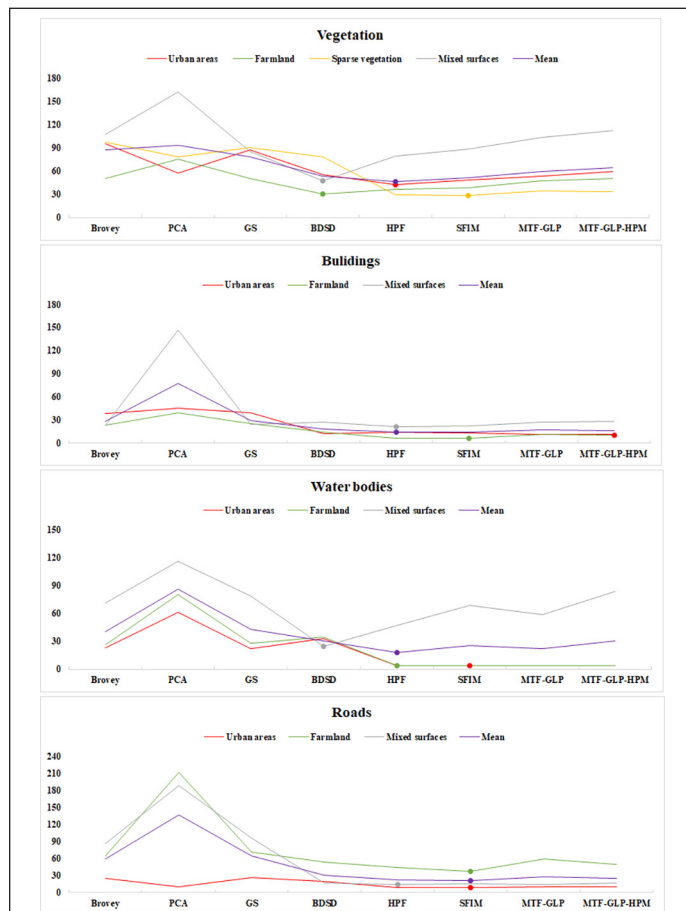

Figure 6. The degree of spectral distortion of different objects. PCA = principal component analysis; GS = Gram-Schmidt; BDSD = band-dependent spatial-detail; HPF = high-pass filtering; SFIM = smoothing filter-based intensity modulation; MTF-GLP = modulation transfer function-generalized Laplacian pyramid; MTF-GLP-HPM = MTF-GLP-high pass modulation.
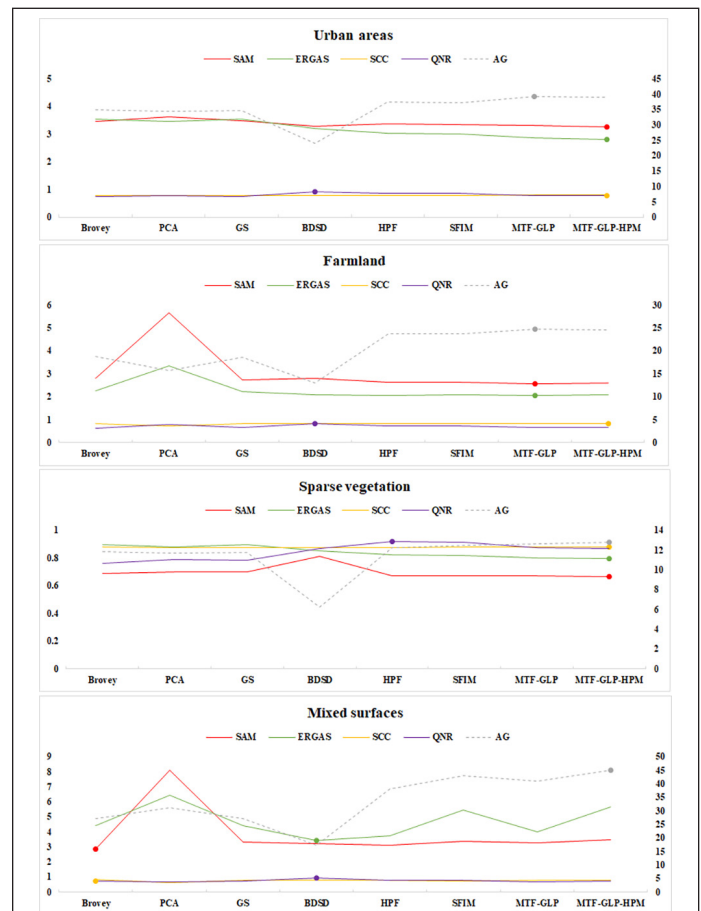

Figure 7. Quantitative evaluation in different scenes. PCA: principal component analysis; GS: Gram-Schmidt; BDSD: band-dependent spatial-detail; HPF: high-pass filtering; SFIM: smoothing filter-based intensity modulation; MTF-GLP: modulation transfer function-generalized Laplacian pyramid; MTF-GLP-HPM: MTF-GLP-high pass modulation.

suitability for the scene can be selected according to the characteristics of the scene.

Although this study only focused on the SuperView satellite, the results provided in this study could be extended to other satellite with similar spatial and spectral characteristics.

Acknowledgments

References

Aiazzi, B., L. Alparone, S. Baronti, A. Garzelli and M. Selva. 2006. MTF-tailored multiscale fusion of high-resolution MS and Pan imagery. *Photogrammetric Engineering and Remote Sensing* 72(5):591–596.

Alcaras, E., C. Parente and A. Vallario. 2021. Automation of pan-sharpening methods for Pléiades images using GIS basic functions. *Remote Sensing* 13(8):1550.

Alparone, L., B. Aiazzi, S. Baronti, A. Garzelli, F. Nencini and M. Selva. 2008. Multispectral and panchromatic data fusion assessment without reference. *Photogrammetric Engineering and Remote Sensing* 74(2):193–200.

Candra, D. S. 2013. Analysis of SPOT-6 data fusion using Gram-Schmidt spectral sharpening on rural areas. *International Journal of Remote Sensing and Earth Sciences (IJReSES)* 10(2).

Chavez, P., S. C. Sides and J. A. Anderson. 1991. Comparison of three different methods to merge multiresolution and multispectral data- Landsat TM and SPOT panchromatic. *Photogrammetric Engineering and Remote Sensing* 57(3):295–303.

Dong, W., Y. Yang, J. Qu, S. Xiao and Q. Du. 2021. Hyperspectral pansharpening via local intensity component and local injection gain estimation. *IEEE Geoscience and Remote Sensing Letters*. https://doi.org/10.1109/LGRS.2021.3094216.

Gangkofner, U. G., P. S. Pradhan and D. W. Holcomb. 2007. Optimizing the high-pass filter addition technique for image fusion. *Photogrammetric Engineering and Remote Sensing* 73(9):1107–1118.

Garzelli, A., F. Nencini and L. Capobianco. 2007. Optimal MMSE pan sharpening of very high resolution multispectral images. *IEEE Transactions on Geoscience and Remote Sensing* 46(1):228–236.

Ghadjati, M., A. Moussaoui and A. Boukharouba. 2019. A novel iterative PCA–based pansharpening method. *Remote Sensing Letters* 10(3):264–273.

Ghassemian, H. 2016. A review of remote sensing image fusion methods. *Information Fusion* 32:75–89.

Guo, P., P. Zhuang and Y. Guo. 2020. Bayesian pan-sharpening with multiorder gradient-based deep network constraints. *IEEE Journal of Selected Topics in Applied Earth Observations and Remote Sensing* 13:950–962.

Haddadpour, M., S. Daneshvar and H. Seyedarabi. 2017. PET and MRI image fusion based on combination of 2-D Hilbert transform and IHS method. *Biomedical Journal* 40(4):219–225.

Imani, M. 2018. Band dependent spatial details injection based on collaborative representation for pansharpening. *IEEE Journal of Selected Topics in Applied Earth Observations and Remote Sensing* 11(12):4994–5004.

Javan, F. D., F. Samadzadegan, S. Mehravar, A. Toosi, R. Khatami and A. Stein. 2021. A review of image fusion techniques for pan-sharpening of high-resolution satellite imagery. *ISPRS Journal of Photogrammetry and Remote Sensing* 171:101–117.

Karathanassi, V., P. Kolokousis and S. Ioannidou. 2007. A comparison study on fusion methods using evaluation indicators. *International Journal of Remote Sensing* 28(10):2309–2341.

Lee, J. and C. Lee. 2009. Fast and efficient panchromatic sharpening. *IEEE Transactions on Geoscience and Remote Sensing* 48(1):155–163.

Li, X., H. Chen, J. Zhou and Y. Wang. 2020. Improving component substitution pan-sharpening through refinement of the injection detail. *Photogrammetric Engineering and Remote Sensing* 86(5):317–325.

Liu, J. 2000. Smoothing filter-based intensity modulation: A spectral preserve image fusion technique for improving spatial details. *International Journal of Remote Sensing* 21(18):3461–3472.

Liu, Y.-K., L.-L. Ma, N. Wang, Y.-G. Qian, Y.-G. Zhao, S. Qiu, C.-X. Gao, X.-X. Long and C.-R. Li. 2020. On-orbit radiometric calibration of the optical sensors on-board SuperView-1 satellite using three independent methods. *Optics Express* 28(8):11085–11105.

Mandhare, R. A., P. Upadhyay and S. Gupta. 2013. Pixel-level image fusion using Brovey transforme and wavelet transform. *International Journal of Advanced Research in Electrical, Electronics and Instrumentation Engineering* 2(6):2690–2695.

Meng, X., H. Shen, H. Li, L. Zhang and R. Fu. 2019. Review of the pansharpening methods for remote sensing images based on the idea of meta-analysis: Practical discussion and challenges. *Information Fusion* 46:102–113.

Metwalli, M. R., A. H. Nasr, O. S. Farag Allah, S. El-Rabaie and F. E. Abd El-Samie. 2010. Satellite image fusion based on principal component analysis and high-pass filtering. *JOSA A* 27(6):1385–1394.

Naidu, V. and J. R. Raol. 2008. Pixel-level image fusion using wavelets and principal component analysis. *Defence Science Journal* 58(3):338.

Pandit, V. R. and R. Bhiwani. 2015. Image fusion in remote sensing applications: A review. *International Journal of Computer Applications* 120(10).

Pushparaj, J. and A. V. Hegde. 2017. Evaluation of pan-sharpening methods for spatial and spectral quality. *Applied Geomatics* 9(1):1–12.

Sarp, G. 2014. Spectral and spatial quality analysis of pan-sharpening algorithms: A case study in Istanbul. *European Journal of Remote Sensing* 47(1):19–28.

Tabib Mahmoudi, F. and A. Karami. 2020. Quantitative assessment of transformation based satellite image pan-sharpening algorithms. *Journal of Electrical and Computer Engineering Innovations (JECEI)* 8(2):161–168.

Tambe, R. G., S. N. Talbar and S. S. Chavan. 2021. Fusion of multispectral and panchromatic images by integrating standard PCA with rotated wavelet transform. *Journal of the Indian Society of Remote Sensing* 49:2033–2055.

Vivone, G., M. Dalla Mura, A. Garzelli, R. Restaino, G. Scarpa, M. O. Ulfarsson, L. Alparone and J. Chanussot. 2021. A new benchmark based on recent advances in multispectral pansharpening: Revisiting pansharpening with classical and emerging pansharpening methods. *IEEE Geoscience and Remote Sensing Magazine* 9(1):53–81.

Vivone, G. 2019. Robust band-dependent spatial-detail approaches for panchromatic sharpening. *IEEE Transactions on Geoscience and Remote Sensing* 57(9):6421–6433.

Vivone, G., L. Alparone, J. Chanussot, M. Dalla Mura, A. Garzelli, G. A. Licciardi, R. Restaino and L. Wald. 2015. A critical comparison among pansharpening algorithms. *IEEE Transactions on Geoscience and Remote Sensing* 53(5):2565–2586.

Wang, Z., J. R. Deller Jr. and B. D. Fleet. 2016. Pixel-level multisensor image fusion based on matrix completion and robust principal component analysis. *Journal of Electronic Imaging* 25(1):013007.

Wang, W., L. Jiao and S. Yang. 2014. Novel adaptive component-substitution-based pan-sharpening using particle swarm optimization. *IEEE Geoscience and Remote Sensing Letters* 12(4):781–785.

Wang, W., H. Liu, L. Liang, Q. Liu and G. Xie. 2019. A regularised model-based pan-sharpening method for remote sensing images with local dissimilarities. *International Journal of Remote Sensing* 40(8):3029–3054.

Yilmaz, V., C. Serifoglu Yilmaz, O. Güngör and J. Shan. 2020. A genetic algorithm solution to the Gram-Schmidt image fusion. *International Journal of Remote Sensing* 41(4):1458–1485.

Yuhendra, J., J. Sri Sumantyo and H. Kuze. 2011. Performance analyzing of high resolution pan-sharpening techniques: Increasing image quality for classification using supervised kernel support vector machine. *Research Journal of Information Technology* 3(1):12–23.

Zhong, S., Y. Zhang, Y. Chen and D. Wu. 2017. Combining component substitution and multiresolution analysis: A novel generalized BDSD pansharpening algorithm. *IEEE Journal of Selected Topics in Applied Earth Observations and Remote Sensing* 10(6):2867–2875.

Call for Submissions

AI-Based Environmental Monitoring with UAV Systems

Photogrammetric Engineering and Remote Sensing (*PE&RS*) is seeking submissions for a special issue on AI-Based Environmental Monitoring with UAV Systems.

Global warming and climate change have become the most important factor threatening the world. Climate change results in dramatical environmental hazards and threatens the planet and human life. A wide variety of policies have been proposed to decrease the effects of global warming and climate change. The most important one is the Paris Agreement which aims to limit global warming to well below two degrees Celcius. Many countries have formulated long term low greenhouse gas emission development strategies related to the Paris Agreement which aimed to meet the essential strategies addressing issues with climate change, environmental protection and low carbon.

The astonishing developments on unmanned aerial vehicle (UAV) systems and artificial intelligence (AI) technologies enables a great opportunity to monitor the environment and propose reliable solutions to restore and preserve the planet and human health.

Data acquisition and processing paradigm has been changed as a result of technological developments. It is obvious that new solutions, innovative approaches will make significant contributions to solve the problems which our planet is facing. UAV data can be collected by various platforms (planes or helicopters, fixed wing systems, drones) and sensors for earth observation and sustainable environmental monitoring which are also utilized by the United Nations to support the delivery of its mandates, resolutions, and activities.

UAV based earth observation data and AI techniques have a wide range of applications such as risk management, disaster monitoring and assessment, environmental impact evaluation and restoration, monitoring agriculture and food cycles, urban analysis, digital twin and smart city applications and providing increased situation awareness. This growth of widely available UAV data associated with the exponential increase in digital computing power, machine learning and artificial intelligence plays a key role in the environmental monitoring and solution generation of geospatial information for the benefit of humans and the planet.

The proposed special issue aims to contributes ASPRS's key mission on 'Simplify and promote the use of image-based geospatial technologies for the end-user', 'Promote collaboration between end users and geospatial experts to match data and technology to applications and solutions' and 'promote the transfer of geospatial data and information technology to developing nations' by serving as an innovative knowledge exchange platform for authors from the globe to deliberate on the latest advancements, state-of-the-art developments and solutions that can help the community to solve many real-world challenges on the topic of "*AI-Based Environmental Monitoring with UAV Systems.*"

This special issue aims to bring researchers to share knowledge and their expertise about state-of-art developments and contribute to the goal of a livable world by integrating human creativity with UAV and AI technologies for environmental monitoring to combat global threats on ecosystems. We wish to discuss the latest developments, opportunities and challenges that can solve many real-world challenges in environmental monitoring including but not limited to:

- AI-Based UAV and GIS Applications
- AI-Based Object Detection and Recognition from UAV Imagery
- AI-Based Digital Twin Applications
- AI-Based Smart City Applications

Papers must be original contributions, not previously published or submitted to other journals. Submissions based on previous published or submitted conference papers may be considered provided they are considerably improved and extended. Papers must follow the instructions for authors at http://asprs-pers.edmgr.com/.

Deadline for Manuscript Submission
May 1, 2022

Submit your Manuscript to
http://asprs-pers.edmgr.com

Guest Editor
Tolga Bakirman, PhD, Yildiz Technical University**, Turkey**
Dr. Tolga Bakirman. bakirman@yildiz.edu.tr. is an assistant professor at Yildiz Technical University in the Department of Geomatic Engineering.

Floating Solar Park Impacts Urban Land Surface Temperature Distribution Pattern

Bo Yingjie, Li Guoqing, Zeng Yelong, and Liu Zhe

Abstract

In recent years, the global photovoltaic industry has developed rapidly. It is significant for evaluating the impact of large-scale solar parks on the environment for the sustainable development of the photovoltaic industry. At present, researchers have paid attention to changes in the local thermal environment caused by solar parks. As a new type of solar park, the influence of floating solar parks on urban land surface temperature distribution patterns is still unclear. In this article, we (1) take the floating solar parks in Huainan City, China, as the study area; (2) calculate the land surface temperature (LST) of the study area and its adjacent areas by using Landsat 8 remote sensing data and the radiation transfer equation method; and (3) judge the influence of solar parks on the distribution pattern of LST. On this basis, we analyzed the influence range and seasonal differences of floating solar parks on LST. Our results revealed that, first, the floating solar park has a warming effect in the summer and winter, and the warming area is concentrated mainly within 200 m of the photovoltaic panels' coverage area. Second, during the construction phase and after the completion of the floating solar parks, the average monthly LST of the solar panels is generally higher than the water, and the average annual temperature increase in the above two stages is 3.26°C and 4.50°C, respectively. The change of floating solar parks on urban LST distribution patterns may impact the local ecosystem. In the future, it is necessary to consider the impact of floating solar parks on local LST during the construction of floating solar parks.

Introduction

Unlike fossil energy sources, such as coal, oil, and natural gas, solar energy has the advantages of cleanness, safety, sustainable regeneration, and convenient access (Parida *et al.* 2011). The global development of photovoltaic power generation has been expected to change energy production and consumption based on fossil energy since the industrial revolution and effectively alleviate the energy crisis, global carbon emissions, and environmental pollution (Kerr 2010; Schmela *et al.* 2016; Forstner *et al.* 2018; Raturi 2019). In recent years, China's photovoltaic power generation has developed rapidly under the encouragement of diversified policies. In 2013 and 2015, China successively surpassed Italy and Germany to become the country with the largest installed capacity of photovoltaic power generation worldwide and has been leading up to now (Li *et al.* 2016; Li and Liu 2020; Raturi 2020). By the end of 2020, the cumulative installed capacity of photovoltaic power generation in China reached 253 GW, an increase of 23.5% year on year (Wong 2021).

However, the construction of large-scale solar park projects will inevitably impact the region's local land, ecology, and energy cycle (Tawalbeh *et al.* 2021). The impact of large-scale solar parks on the

environment during construction is similar to that of other industrial manufacturing processes. For example, engineering activities, such as land leveling and installing solar panels, directly change the original soil, vegetation, topography, and land use status. These activities further change their original form and even destroy the stable structure of the original environmental elements, resulting in land disturbance, vegetation destruction, and soil erosion (Li *et al.* 2017; Choi *et al.* 2020; Tawalbeh *et al.* 2021; Yue *et al.* 2021). After the solar parks are built, solar panels will absorb short-wave radiation to convert solar energy into electric energy and at the same time radiate long-wave radiation outward. This will change the energy flow mode of the local surface and affect the power generation efficiency of solar panels, local climate, and energy cycle of the ecosystem (Yang *et al.* 2015, 2017; Fan and Wang 2020; Pimentel Da Silva *et al.* 2020). Using remote sensing to analyze land surface temperature (LST) change can effectively judge the influence of large-scale solar parks on the energy cycle (Liou *et al.* 2017; Shao *et al.* 2019a; Wang *et al.* 2021). Studies have shown that the daily average LST around the solar park is reduced by 0.53°C (Zhang and Xu 2020). However, in the desert and Gobi, the cooling effect of the solar park is more obvious, and the average annual decrease of LST can reach 4°C with an influence range of about 100–600 m (Chang *et al.* 2018; Liu *et al.* 2019; Li and Liu 2020).

In recent years, with the continuous expansion of the scale of the photovoltaic industry, the water surface in cities and towns has become one of the available areas for building solar parks, which has explored a new model for the development of global new energy and cleaner production (Sahu *et al.* 2016). However, there is no effective analysis to judge the influence range and variation range of the floating solar parks on the local temperature due to the significant difference between the underlying surface of the floating solar parks and the solar land parks. Because of this, we take the floating solar parks in Huainan City, Anhui Province, China, as the research area and use remote sensing data to judge the influence of the floating solar parks on the surrounding LST. Our research objectives are as follows:

1. Based on Google Earth Engine and *Landsat 8* remote sensing images, the radiation transfer equation method constructed LST data sets of floating solar parks and their adjacent areas.
2. Using LST data sets, we can judge the influence of solar parks on the spatial distribution pattern of LST.
3. On this basis, the spatial range and warming or cooling range of the solar parks on the LST is obtained.

Data and Methods

Study Area

The study area is located in Huainan City, Anhui Province. The climate in this area is warm temperate semi-humid monsoon, with high-temperature and rainy summers and cold and dry winters. The annual sunshine hours are 2000 hours, and the annual solar radiation is 4,800 MJ/m^2 (1990–2020, data from Bengbu and Lu'an meteorological stations).

Bo Yingjie, Li Guoqing, and Liu Zhe are with Ludong University, Institute of Resources and Environmental Engineering, Yantai 264025, China (corresponding author, Li Guoqing: ligqing@foxmail.com).

Zeng Yelong is with the Aerospace Information Research Institute, Beijing, China, 100101; the Chinese Academy of Sciences, Beijing 100101, China; and the State Key Laboratory of Remote Sensing Science, Beijing 100101, China.

The sunshine time is long, and the solar energy resources are abundant. In recent years, relying on the advantages of resources and policies, the local government has built large-scale floating solar parks on the water surface in the coal mining subsidence area. The location of the floating solar park in this study is shown in Figure 1. It is located on the water surface of the coal mining subsidence area and adopts the mode of solar power generation on water and aquaculture underwater. The total installed capacity is 20 MWp, one of the largest floating solar parks in the world at present. The construction of the floating solar park started in November 2015 and was officially completed in October 2016. The construction period of the floating solar park ranged from November 2015 to October 2016.
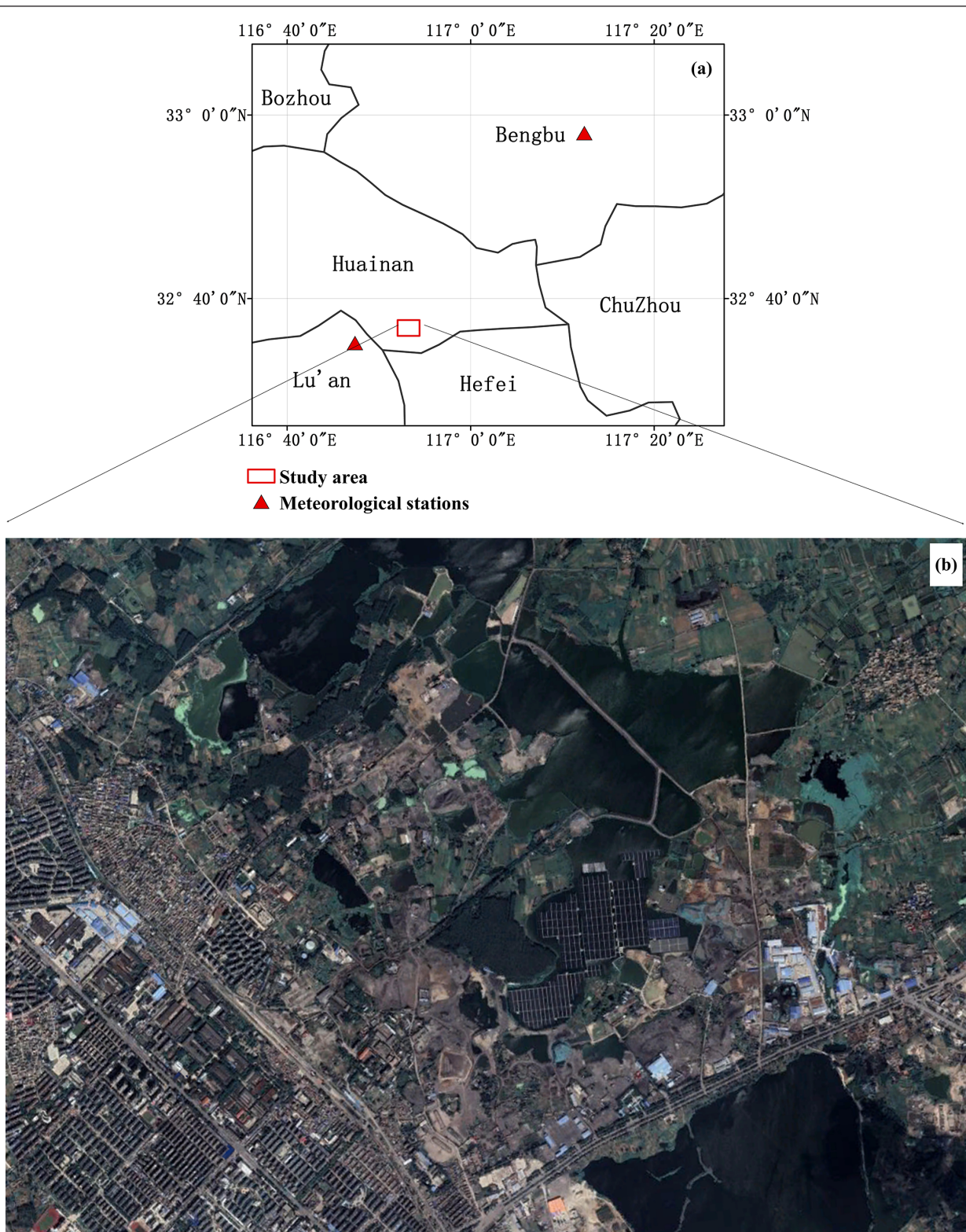
Figure 1. (a) Location of the study area. (b) Part of the Landsat 8 OLI true color image of the study area acquired on 12 January 2021 (the path-row is 121-37).

It is generally believed that the influence of solar park on LST is within 600 m (Liu *et al.* 2019; Li and Liu 2020). Therefore, we take the floating solar park as the center, and we take the buffer zone of 1 km around the solar park as the potential influence area, totaling 25 km². According to the construction phases of the floating solar park and comparing them with the historical images of *Landsat 8* and Google Earth, the typical types of land use are obtained by visual interpretation. Finally, we retrieve the distributions of the floating solar park, water, forests, crops, nudation, and buildings within 25 km².

Remote Sensing and Climate Data

Landsat 8 remote sensing image data sets (USGS *Landsat 8* surface reflectance Tier 1, image collection ID, Landsat/lc08/c01/t1_sr) with path-row numbers of 121-38 and 121-37 from March 2013 to February 2019 were obtained on Google Earth Engine. This was done to obtain as many cloudless remote sensing images as possible and improve the continuity of data in this study. The spatial resolution of the data set is 30 m, including five visible light and near-infrared bands, two shortwave infrared bands and quality information bands (pixel_qa). A total of 292 images were collected in the study area, and their temporal distribution is shown in Figure 2.
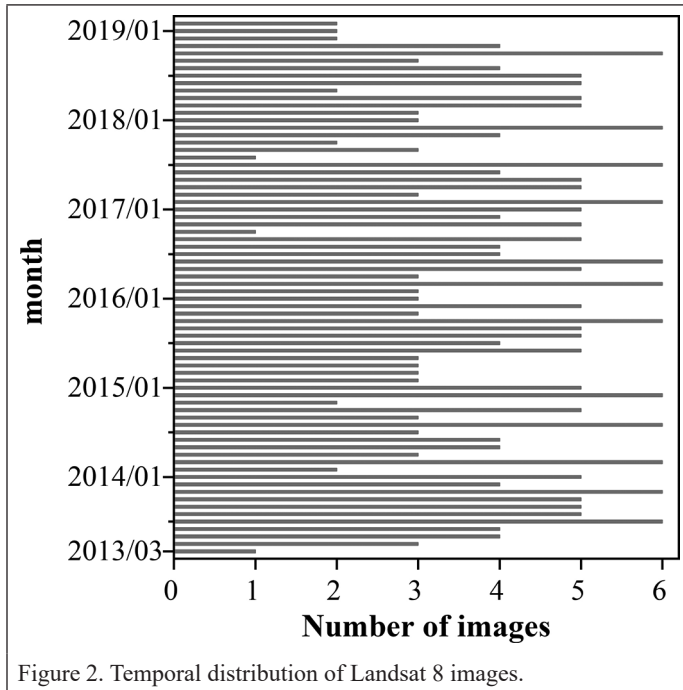

Figure 2. Temporal distribution of Landsat 8 images.

The monthly air temperature of the Bengbu meteorological station and Lu'an meteorological station comes from the monthly surface climate data set of the China meteorological data network (http://data.cma.cn). The locations of the meteorological stations are shown in Figure 1.

Calculation of LST

Because standard deviations about the mean bias are significantly higher for *Landsat 8* band 11 (11.50–12.51 μm) (Cook *et al.* 2014), we chose band 10 (10.60–11.19 μm) and adopted the single-channel method proposed to calculate the LST (Jimenez-Munoz and Sobrino 2003; Jimenez-Munoz *et al.* 2014). This method is suitable for the LST calculation of Landsat data in a long time series. It is also widely used in urban land surface environment assessment and human activity impact assessment (Eldesoky *et al.* 2021; Firozjaei *et al.* 2021; Wang *et al.* 2021). Its calculation formulas are as follows:

$$T_s = \gamma \left[\frac{1}{\varepsilon} \left(\psi_1 L_{\text{sen}} + \psi_2 \right) + \psi_3 \right] + \delta \tag{1}$$

$$\gamma \approx \frac{T_{\text{sen}}^2}{b_s L_{\text{sen}}} \ , \ \varphi \approx T_{\text{sen}} - \frac{T_{\text{sen}}^2}{b_s}, \tag{2}$$

where T_s is the land surface temperature, ε is surface emissivity, and L_{sen} is the radiance at the sensor (W·m^{-2}·sr^{-1}·μm^{-1}). Further, T_{sen} is the sensor brightness temperature, b_y equals 1324 K, and ψ_1, ψ_2, and ψ_3 are atmospheric functions, which can be obtained by the following formula:

$$\psi_1 = \frac{1}{\tau}; \psi_2 = -L_{\text{d}} - \frac{L_{\text{u}}}{\tau}; \psi_3 = L_d \tag{3}$$

where τ, L_{u}, and L_{d} are atmospheric transmittance, upwelling radiance (W·m^{-2}·sr^{-1}·μm^{-1}), and downwelling radiance (W·m^{-2}·sr^{-1}·μm^{-1}), respectively. These atmospheric profile parameters can be calculated at http://atmcorr.gsfc.nasa.gov (Sobrino *et al.* 2008; Jimenez-Munoz *et al.* 2014). The surface emissivity is calculated by the following:

$$\varepsilon = \begin{cases} 0.99, \text{NDVI} < 0\ 00 \\ 0.97, \ \ 0.00 \le \text{NDVI} < 0.15 \\ \varepsilon_v P_v + \varepsilon_s \left(1 - P_v\right), 0\ 15 \le \text{NDVI} \le 0.45 \\ 0.985, \ \text{NDVI} > 0.45 \end{cases} \tag{4}$$

where the surface emissivity of water is 0.99, ε_s is 0.97, and ε_v is 0.985. P_v is the vegetation coverage, and its calculation formula is as follows (Sobrino *et al.* 2008; Jimenez-Munoz *et al.* 2014):

$$P_v = \left(\frac{\text{NDVI}_i - \text{NDVI}_s}{\text{NDVI}_v - \text{NDVI}_s} \right)^2 \tag{5}$$

where NDVI_i is the normalized difference vegetation index of pixels, and NDVI_s is the NDVI value of bare soil with a value of 0.15. Further, NDVI_v is the NDVI value of vegetation with a value of 0.45. The calculation formula of NDVI is as follows (Sobrino *et al.* 2008):

$$\text{NDVI} = \frac{\rho_{\text{NIR}} - \rho_{\text{R}}}{\rho_{\text{NIR}} + \rho_{\text{R}}} \tag{6}$$

where ρ_{NIR} is the surface reflectance in the near-infrared band and ρ_{R} is the surface reflectance in the red band.

We use pixel_qa band and methods to filter pixels with clouds and get the cloudless LST of all images (Shao *et al.* 2019b) to reduce the influence of the cloud on the calculation results of LST. Then the LST of the remote sensing images in each month is averaged, and the monthly average LST from March 2013 to February 2019 is obtained. Because there are too many clouds in remote sensing images in April 2014, July 2014, and May 2015, the LST of the above date is not calculated. In addition, our purpose is to compare the difference of LST in different construction periods of floating solar parks. There is no strict requirement on the absolute accuracy of LST calculation. Therefore, the influence of the error of the LST algorithm on the results can be ignored basically.

Impact of Climate Change on LST

We constructed the calculation formula of the difference LST_{s-a} between LST and the air temperature in the corresponding month to eliminate the influence of climate change on LST as much as possible, which is as follows:

$$\text{LST}_{s-a} = \text{LST}_i - T_{ai} \tag{7}$$

where LST_i is the LST of the *i* month and T_{ai} is the air temperature of the *i* month, which is the monthly average value of two meteorological stations in Figure 1.

LST Distribution Pattern

We chose summer and winter as the two seasons with the most obvious temperature changes for comparative analysis to judge the influence of a floating solar park on the LST distribution pattern. Based on formula (7), the LST_{s-a} of the floating solar park construction area and its adjacent areas in summer (June–August) and winter (December–February of the following year) are extracted. Further, the LST_{s-a} difference between the completion and before the construction of the floating solar

park is calculated. On this basis, local Moran's I is used to analyze the influence of the solar park on the surrounding area's LST. Then the influence distance of the solar park on LST is judged.

The local Moran's I that passed the significance test (p ≤ 0.05) has four output modes: high-value (HH) clustering; low-value (LL) clustering; abnormal value (HL), whose high value is surrounded mainly by a low value; and abnormal value (LH), whose low value is surrounded mainly by a high value (Anselin 1995; Kan *et al.* 2018; Bartesaghi-Koc *et al.* 2019; Chen *et al.* 2021). In this study, the HH mode represents a spatial agglomeration of LST_{s-a} with a high value as the center. The LL mode represents a spatial agglomeration of LST_{s-a} with a low value as the center. The HL mode represents an abnormal value of LST_{s-a} with a high value surrounded mainly by a low value. Finally, the LH mode represents LST_{s-a} with a low value surrounded mainly by a high value. Notably, the LST in the summer before construction and completion is the average value of the summer from 2013 to 2014 and 2017 to 2018, respectively, to eliminate the deviation of the analysis results caused by a single year. Further, the LST in the winter before construction and completion is the average value of the winter from 2013 to 2014 and 2017 to 2018, respectively.

Phases of LST
According to the construction cycle of the floating solar park, the LST variation curves of the preconstruction phase (March 2013–October 2015), construction phase (November 2015–October 2016), and completion phase (November 2016–February 2019) are obtained.

Then ArcGIS 10.2 is used to extract the mean and standard deviation of monthly LST and LST_{s-a} of typical land use types around the floating solar park. By comparing the changes of the above indexes, the influence of different construction phases of the floating solar park on LST is analyzed.

Results and Analysis

Range and Seasonal Differences
Figure 3 shows that there is a warming effect of the floating solar park on LST in summer. In summer, the "cold island" formed by the original water before the construction of the solar park is cut off, and a warm area is formed (Figure 3a and 3b). The construction of a floating solar park has increased the LST in its occupied area (Figure 3c), the maximum temperature increase of LST_{s-a} exceeding 7°C and the average temperature increase of LST_{s-a} reaching 4.9°C. The LST in the forest decreased, and LST_{s-a} decreased by 1.1°C on average, forming a local low-temperature center. The LST of crops near the edge of the floating solar park increased, and the LST_{s-a} increased by 3°C to 5°C. Meanwhile, the LST of crops far away from the warm area of the floating solar park had no obvious changes. Nudation is blocked by forests, and its LST has no obvious change. According to local Moran's I (Figure 3d), the LST of the floating solar park conforms to the HH mode in the summer, and the warming effect on adjacent areas is concentrated within 200 m. This is mainly in the waters of the construction area
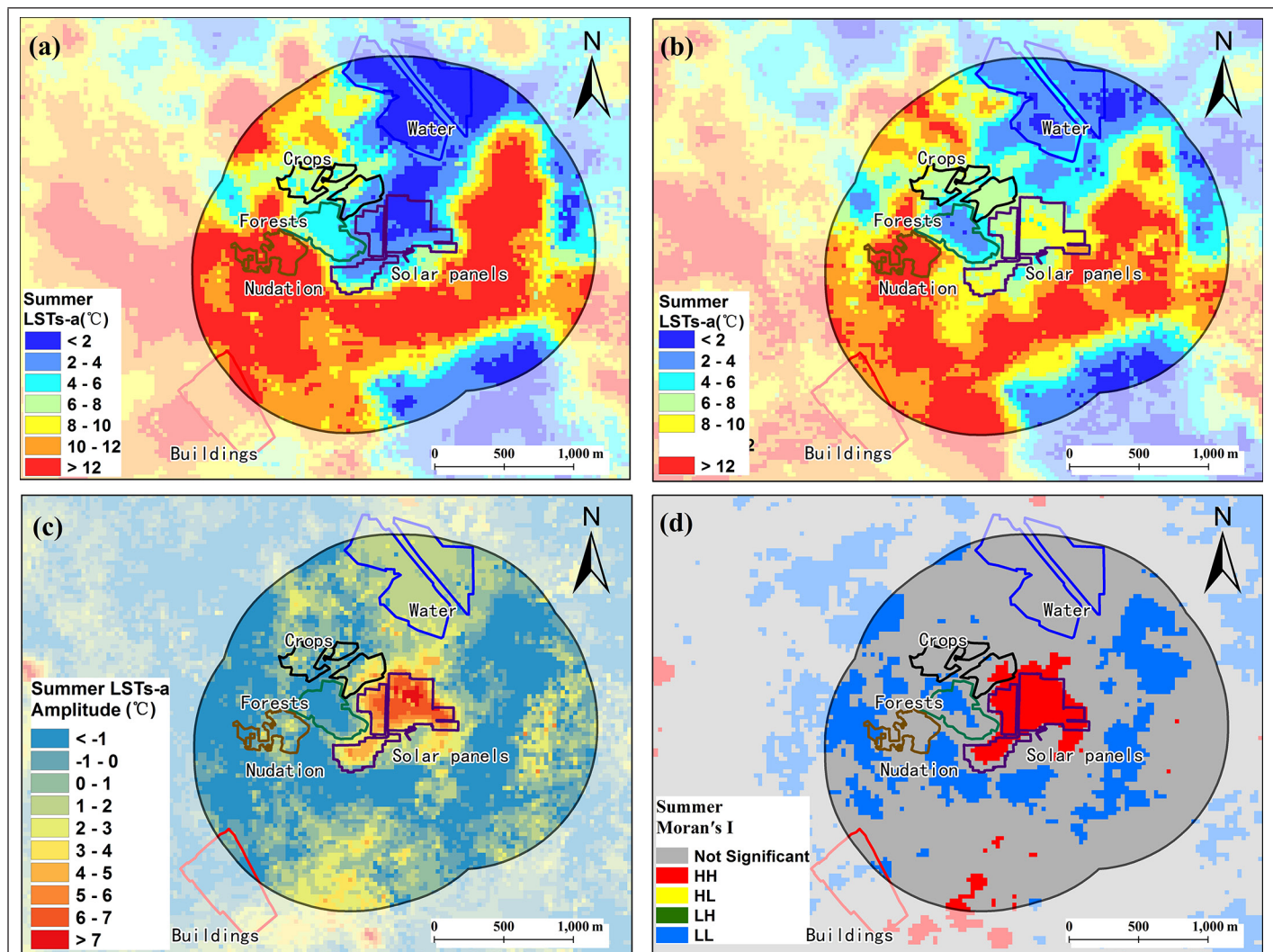

Figure 3. The influence of the floating solar park on the spatial distribution of LST_{s-a} in summer. (a) The spatial distribution of LST_{s-a} in the preconstruction phase in summer. (b) The spatial distribution of LST_{s-a} in the completion phase in summer. (c) The LST_{s-a} change range (Figure 3b minus Figure 3a) in summer. (d) Local Moran's I of the LST_{s-a} change range in summer.

in the north, the crops in the west, and the water edge in the southeast adjacent to the floating solar park.

Figure 4c shows that in winter, the construction of a floating solar park increases the LST within the solar panels' area, and the average temperature increase of $LST_{s–a}$ is 3.5°C, smaller than that in summer. The cold island area formed by the water before the construction of the floating solar park is cut off, and a warm area is formed in the solar panels' area (Figure 4a and 4b). The floating solar park forms a warm area with forests and crops. Nudation is blocked by forests, and its LST has no obvious change. The local Moran's I (Figure 4d) shows that the warming effect of the floating solar park in the winter is weaker than that in the summer and concentrates on the solar panels' area and the waters only within 200 m.

Different Construction Phases of LST

Figure 5 shows that before the construction phase of the floating solar park, the LST change curves of the proposed solar panels' area and the waters are consistent, which are 20.2°C and 19.6°C, respectively. Further, the monthly average LST is lower than that of other areas. In the construction phase and completion phase of the floating solar park, the average monthly LST of the area where solar panels are located is generally higher than that of water, close to the LST of forests and the LST of buildings in some periods.

According to local Moran's I results, the influence of the floating solar park on LST is concentrated mainly within 200 m of the solar panels, and its warming effect on the surrounding typical land use types is very weak. We use the $LST_{s–a}$ variation range to determine the warming level of the floating solar park in different construction phases. Figure 6 shows that before the construction of the floating solar park, the difference of $LST_{s–a}$ between the proposed solar panels and water was weak at only 0.06°C. The $LST_{s–a}$ difference in the construction phase increases to 2.77°C. Further, the difference of $LST_{s–a}$ between solar panels and water reached 3.96°C, indicating that the construction of the floating solar park had an obvious warming effect on LST.

The $LST_{s–a}$ in the preconstruction phase is the average value from March 2013 to February 2015, the $LST_{s–a}$ in the construction phase is the average value from November 2015 to October 2016, and the $LST_{s–a}$ in the completion phase is the average value from March 2017 to February 2019. The shadow is the standard deviation of the $LST_{s–a}$.

Discussion and Conclusion

Discussion

Cloud coverage impacted the results. Cloud coverage impacts the calculation of LST using *Landsat 8* and reduces LST accuracy, potentially leading to deviation in judging the influence of the floating solar park on LST. We have also considered using MODIS LST products with a higher temporal resolution to analyze the influence of the floating solar park on the LST distribution pattern. However, the spatial details of LST cannot be displayed, and the influence range of solar park on the LST cannot be obtained due to the low spatial resolution (1 km) of MODIS.
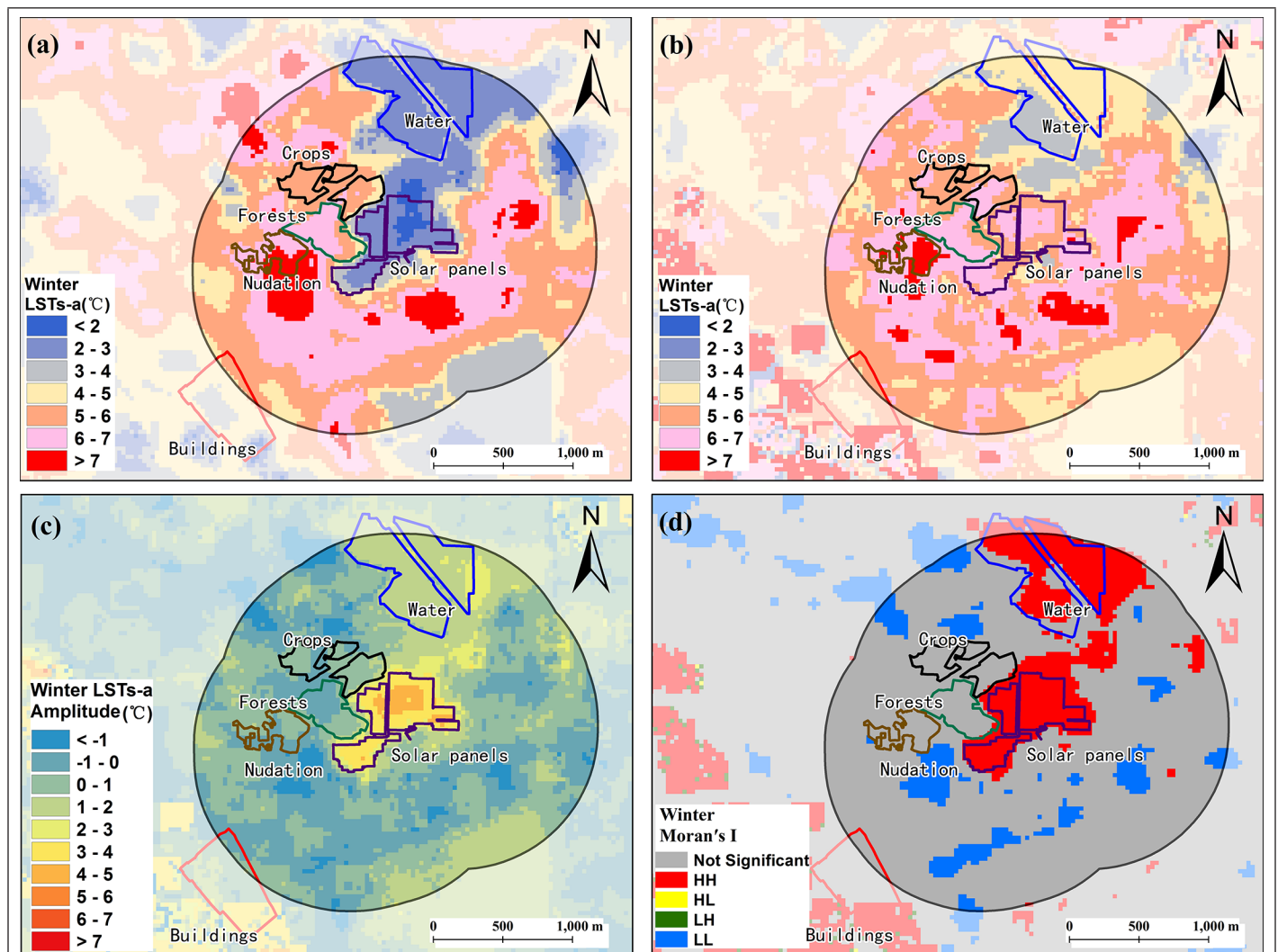

Figure 4. The influence of the floating solar park on the spatial distribution of $LST_{s–a}$ in winter. (a) The spatial distribution of $LST_{s–a}$ in the preconstruction phase in winter. (b) The spatial distribution of $LST_{s–a}$ in the completion phase in winter. (c) The $LST_{s–a}$ change range (Figure 4b minus Figure 4a) in winter. (d) Local Moran's I of the $LST_{s–a}$ change range in winter.
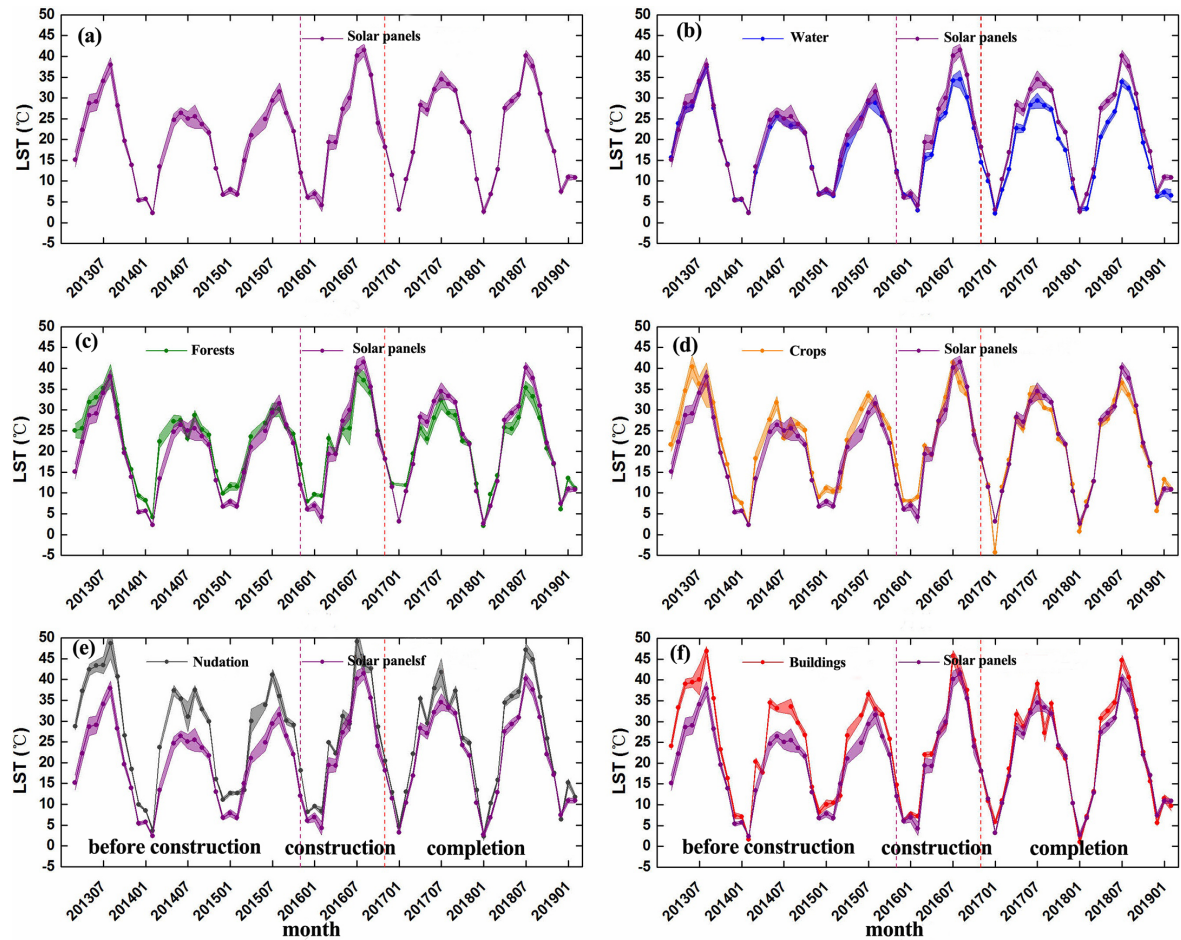
Figure 5. Monthly LST curve of the floating solar park and typical land use types in different construction phases. The LST change curves of (a) solar panels, (b) solar panels and water, (c) solar panels and forests, (d) solar panels and crops, (e) solar panels and nudation, and (f) solar panels and buildings.
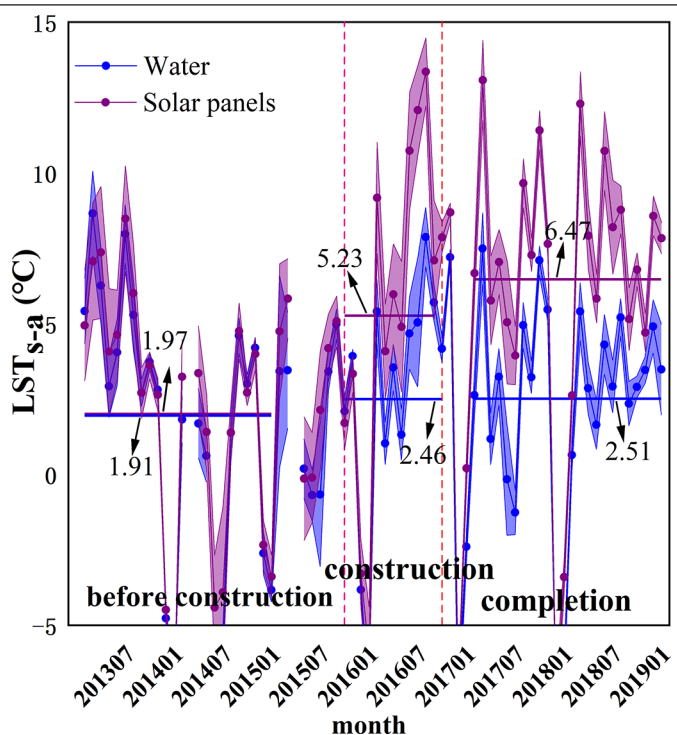

Figure 6. Changes of LST_{s-a} in different construction phases of the floating solar park.

Therefore, this article analyzes the influence of the floating solar park on the LST by using *Landsat 8* data.

The influence range and extent of the solar park on the LST of different land use types are inconsistent (Li *et al.* 2021). The solar park in our study area is located on the water surface, which has a warming effect within 200 m of the construction area and its vicinity, but 23 of the largest solar land parks in the world show that the daily average LST around the solar parks decreases by 0.53°C (Zhang and Xu 2020). However, in the solar parks of the desert and Gobi, the average annual decrease of LST can reach 4°C (Chang *et al.* 2018). Therefore, it is necessary to make a comparative study on different types of solar parks to judge the influence of solar parks on LST. Even for the floating solar parks, the influence range and extent of floating solar parks on LST may differ due to the difference in water depth, local climate, and distribution range of solar parks. Therefore, we need to consider the above factors in future research.

The combination of actual measurement and unmanned aerial vehicle remote sensing is the key way to judge floating solar parks' influence on LST. There are not only seasonal differences but also day and night differences in the influence of solar parks on LST distribution patterns (Li and Liu 2020). However, it is still impossible to judge the influence of floating solar parks on LST at night due to the limited data of Aster night remote sensing images and the low spatial resolution of MODIS night remote sensing images. While the measured data can obtain the change of LST at night, the measured data are only some representative "points", making it very difficult to judge the influence of floating solar parks on LST as a whole. Therefore, it is a reference method to acquire the LST changes around the solar parks by unmanned aerial vehicle in different seasons, days and nights, and then combine the measured LST data.

The change of LST distribution pattern may affect the local urban ecosystem (Shao *et al.* 2020). While the results of this study show that the floating solar park will not significantly affect the LST outside 200 m, the coverage of the solar panels will significantly reduce the energy obtained by algae through photosynthesis in water, affecting the energy cycle of the ecosystem in water. In addition, the increase of LST will affect the material and energy flow of the local urban ecosystem and produce a series of ecological and environmental effects, such as the change of atmospheric environment and urban biological habits. No matter whether this effect is positive or negative, there is still a lack of further research.

Conclusion

Land take for solar parks has increased all over the world and is projected to continue. Despite this, the impacts on the ecosystem such as carbon sequestration and feedback to electricity carbon intensity are poorly understood in comparison to what is known for wind energy and other land use and land cover changes. This article analyzed the LST of floating solar parks in different construction phases and seasons. Our results showed that the floating solar park has a warming effect on the solar panels' coverage area and their vicinity within 200 m. Further, its warming range in summer was greater than that in winter, providing a reference for judging the impact of the solar park on the local climate and environment. Moreover, the impact was evident in the field despite smaller measurement areas.

Given the projected deployment of photovoltaics, increasing land use pressures, and growing recognition of the importance of our eco-systems, there is a critical need for a better understanding of the temperature impacts of solar parks and associated cascading impacts on ecosystem function. This knowledge will inform energy and land use policies and enable better design, location, and surrounding land management use decisions. In the follow-up study, we should focus mainly on judging the impact of the floating solar park on LST at night. We should further consider combining ground observation and unmanned aerial vehicle remote sensing observation, which is very important to judge the overall impact of floating solar parks on the local ecosystem.

References

Anselin, L. 1995. Local indicators of spatial association—LISA. *Geographical Analysis* 27(2):93–115.

Bartesaghi-Koc, C., P. Osmond and A. Peters. 2019. Spatio-temporal patterns in green infrastructure as driver of land surface temperature variability: The case of Sydney, *International Journal of Applied Earth Observation and Geoinformation* 83:101903.

Chang, R. Y. Shen, Y. Luo, B. Wang Z. Yang and P. Guo. 2018. Observed surface radiation and temperature impacts from the large-scale deployment of photovoltaics in the barren area of Gonghe, China. *Renewable Energy* 118:131–137.

Chen, L., X. L. Wang, X. B. Cai, C. Yang and X. R. Lu. 2021. Seasonal variations of daytime land surface temperature and their underlying drivers over Wuhan, China. *Remote Sensing* 13(2):323.

Choi, C. S., A. E. Cagle, J. Macknick, D. E. Bloom, J. S. Caplan and S. Ravi. 2020. Effects of revegetation on soil physical and chemical properties in solar photovoltaic infrastructure. *Frontiers in Environmental Science* 8:140.

Cook, M., J. R. Schott, J. Mandel, and N. Raqueno. 2014. Development of an operational calibration methodology for the Landsat Thermal Data Archive and initial testing of the atmospheric compensation component of a land surface temperature (LST) product from the Archive. *Remote Sensing* 6(11):11244–11266.

Eldesoky, A.H.M., J. Gil and M. B. Pont. 2021. The suitability of the urban local climate zone classification scheme for surface temperature studies in distinct macroclimate regions. *Urban Climate* 37(1):100823.

Fan, C. and Z. Wang. 2020. Spatiotemporal characterization of land cover impacts on urban warming: A spatial autocorrelation approach. *Remote Sensing* 12(10):1631.

Firozjaei, M. K,. A. Sedighi, H. K. Firozjaei, M. Kiavarz, M. Homaee, J. J. Arsanjani, M. Makki, B. Naimi and S. K. Alavipanah. 2021. A historical and future impact assessment of mining activities on surface biophysical characteristics change: A remote sensing-based approach. *Ecological Indicators* 122:107264.

Forstner, H.J.L., S. Bandil, G. Coletti, W. C. Sinke, J. H. Bultman, M. Fischer, T. Spiess, M. Mette, A. Mette, K. Petter, A. Gerlach and P. Engelhart. 2018. International technology roadmap for photovoltaic results 2017. *International Technology Roadmap for Photovoltaics*. Berlin, Germany: German Engineering Federation.

Jimenez-Munoz, J. C. and J. A. Sobrino. 2003. A generalized single-channel method for retrieving land surface temperature from remote sensing data. *Journal of Geophysical Research: Atmospheres* 108(D22):4688.

Jimenez-Munoz, J. C., J. A. Sobrino, D. Skokovic, C. Mattar and J. Cristobal. 2014. Land surface temperature retrieval methods from Landsat-8 thermal infrared sensor data. *IEEE Geoscience and Remote Sensing Letters* 11(10):1840–1843.

Kan, A. K., G. Q. Li, X. Yang, Y. L. Zeng, L. Tesren and J. He. 2018. Ecological vulnerability analysis of Tibetan towns with tourism-based economy: A case study of the Bayi District. *Journal of Mountain Science* 15(5):1101–1114.

Kerr, T. 2010. Global gaps in clean energy RD&D: Update and recommendations for international collaboration. *Report for the Clean Energy Ministerial*. Paris, France: International Energy Agency.

Li, G., R. R. Hernandez, G. A. Blackburn, G. Davies, M. Hunt, J. D. Whyatt and A. Armstrong. 2021. Ground-mounted photovoltaic solar parks promote land surface cool islands in arid ecosystems. *Renewable and Sustainable Energy Transition* 1:100008.

Li, G. A. and Z. Liu. 2020. Effect of solar power plants on land surface temperature. *Acta Energiae Solaris Sinica* 41(12):117–123.

Li, L., T. Chi, M. Zhang and S. Wang. 2016. Multi-layered capital subsidy policy for the PV industry in China considering regional differences. *Sustainability* 8(1):45.

Li, S., J. Weigand and S. Ganguly. 2017. The potential for climate impacts from widespread deployment of utility-scale solar energy installations: An environmental remote sensing perspective. *Journal of Remote Sensing & GIS* 6(1):1000190.

Liou, Y.I.A., A. K. Nguyen and M. H. Li. 2017. Assessing spatiotemporal eco-environmental vulnerability by Landsat data. *Ecological Indicators* 80:52–65.

Liu, Z., H. Yang, X. Chen and B. Shen. 2019. Impact analysis of solar park on land surface temperature. *Geospatial Information* 17(10):20–23.

Parida, B., S. Iniyan and R. Goic. 2011. A review of solar photovoltaic technologies. *Renewable and Sustainable Energy Reviews* 15(3):1625–1636.

Pimentel Da Silva, G. D., A. Magrini and D.A.C. Branco. 2020. A multicriteria proposal for large-scale solar photovoltaic impact assessment, *Impact Assessment Project Appraisal* 38(1):3-15

Raturi, A. K. 2019. Renewables 2019 global status report, *Global Status Report*. Paris, France: Renewables Now 21.

Raturi, A. K. 2020. Renewables 2020 global status report. *Global Status Rrport*. Paris, France: Renewables Now 21.

Sahu, A., N. Yadav and K. Sudhakar. 2016. Floating photovoltaic power plant: A review. *Renewable and Sustainable Energy Reviews* 66:815–824.

Schmela, M., G. Masson and N. T. Mai. 2016. Global market outlook for solar power 2016–2020. *Solar Power Europe*. Brussels, Belgium: European Photovoltaic Industry Association.

Shao, Z. F., J. J. Cai, P. Fu, L. Q. Hu and T. Liu. 2019a. Deep learning-based fusion of Landsat-8 and Sentinel-2 images for a harmonized surface reflectance product. *Remote Sensing of Environment* 235(11):14–125.

Shao, Z. F., L. Ding, D. R. Li, O. Altan, M. E. Huq and C. M. Li. 2020. Exploring the relationship between urbanization and ecological environment using remote sensing images and statistical data: A case study in the Yangtze River Delta. China. *Sustainability* 12(14):5620.

Shao, Z. F., Y. Pan, C. Y. Diao and J. J. Cai. 2019b. Cloud detection in remote sensing images based on multiscale features-convolutional neural network. *IEEE Transactions on Geoscience and Remote Sensing* 57(6):4062–4076.

Sobrino, J. A., J. C. Jimenez-Munoz, G. Soria, M. Romaguera, L. Guanter, J. Moreno, A. Plaza and P. Martínez. 2008. Land surface emissivity retrieval from different VNIR and TIR sensors. *IEEE Transactions on Geoscience and Remote Sensing* 46(2):316–327.

Tawalbeh, M., A. Al-Othman, F. Kafiah, E. Abdelsalam, F. Almomani and M. Alkasrawi. 2021. Environmental impacts of solar photovoltaic systems: A critical review of recent progress and future outlook. *Science of the Total Environment* 759:143528.

Wang, Y. F., Z. B. Ni, M. M. Hu, S. Q. Chen and B. C. Xia. 2021. A practical approach of urban green infrastructure planning to mitigate urban overheating: A case study of Guangzhou. *Journal of Cleaner Production* 287:124995.

Wong, S. 2021. Cumulative installed solar power capacity in China 2012–2020. *Energy and Environment* 5:135–139.

Yang, L. W., X. Q. Gao, F. Lv, X. Y. Hui, L. Y. Ma and X. H. Hou. 2017. Study on the local climatic effects of large photovoltaic solar farms in desert areas. *Solar Energy* 144:244–253.

Yang, L., X, Gao and F. Lyu. 2015. Study on the impact of large solar farm on radiation field in desert areas of Golmud. *Acta Energiae Solaris Sinica* 36(9):2160–2166.

Yue, S., M. Guo, P. Zou, W. Wu and X. Zhou. 2021. Effects of photovoltaic panels on soil temperature and moisture in desert areas. *Environmental Science and Pollution Research* 28(14):17506–17518.

Zhang, X. H. and M. Xu. 2020. Assessing the effects of photovoltaic powerplants on surface temperature using remote sensing techniques. *Remote Sensing* 12(11):18–25.

WHO'S WHO IN ASPRS

Founded in 1934, the American Society for Photogrammetry and Remote Sensing (ASPRS) is a scientific association serving thousands of professional members around the world. Our mission is to advance knowledge and improve understanding of mapping sciences to promote the responsible applications of photogrammetry, remote sensing, geographic information systems (GIS) and supporting technologies.

BOARD OF DIRECTORS
BOARD OFFICERS

President
Christopher Parrish, Ph.D
Oregon State University

President-Elect
Lorraine B. Amenda, PLS, CP
Towill, Inc.

Vice President
Bandana Kar
Oak Ridge National Lab

Past President
Jason M. Stoker, Ph.D,
U.S. Geological Survey

Treasurer
Stewart Walker, Ph.D.
photogrammetry4u

Secretary
Harold Rempel
ESP Associates, Inc.

COUNCIL OFFICERS
ASPRS has six councils. To learn more, visit https://www.asprs.org/Councils.html.

Sustaining Members Council
Chair: Ryan Bowe
Deputy Chair: Melissa Martin

Technical Division Directors Council
Chair: Bill Swope
Deputy Chair: Hope Morgan

Standing Committee Chairs Council
Chair: David Stolarz
Deputy Chair: TBA

Early-Career Professionals Council
Chair: Madeline Stewart
Deputy Chair: Kyle Knapp

Region Officers Council
Chair: Demetrio Zourarakis
Deputy Chair: Jason Krueger

Student Advisory Council
Chair: Lauren McKinney-Wise
Deputy Chair: Oscar Duran

TECHNICAL DIVISION OFFICERS
ASPRS has seven professional divisions. To learn more, visit https://www.asprs.org/Divisions.html.

Geographic Information Systems Division
Director: Denise Theunissen
Assistant Director: Jin Lee

Lidar Division
Director: Ajit Sampath
Assistant Director: Mat Bethel

Photogrammetric Applications Division
Director: Ben Wilkinson
Assistant Director: Hank Theiss

Primary Data Acquisition Division
Director: Greg Stensaas
Assistant Director: Srini Dharmapuri

Professional Practice Division
Director: Bill Swope
Assistant Director: Hope Morgan

Remote Sensing Applications Division
Director: Amr Abd-Ehrahman
Assistant Director: Tao Liu

Unmanned Autonomous Systems (UAS)
Director: Jacob Lopez
Assistant Director: Bahram Salehi

REGION PRESIDENTS
ASPRS has 13 regions to serve the United States. To learn more, visit https://www.asprs.org/regions.html.

Alaska Region

Cascadia Region
Robert Hariston-Porter

Eastern Great Lakes Region
Michael Joos, CP, GISP

Florida Region
Xan Fredericks

Heartland Region
Whit Lynn

Intermountain Region
Robert T. Pack

Mid-South Region
David Hughes

Northeast Region

North Atlantic Region

Pacific Southwest Region
John Erickson, PLS, CP

Potomac Region
Dave Lasko

Rocky Mountain Region

Western Great Lakes Region
Adam Smith

SUSTAININGMEMBERS

ACI USA Inc.
Weston, Florida
https://acicorporation.com/
Member Since: 2/2018

Aerial Services, Inc.
Cedar Falls, Iowa
www.AerialServicesInc.com
Member Since: 5/2001

Airworks Solutions Inc.
Boston, Massachusetts
Member Since: 3/2022

Applanix
Richmond Hill, Ontario, Canada
http://www.applanix.com
Member Since: 7/1997

Ayres Associates
Madison, Wisconsin
www.AyresAssociates.com
Member Since: 1/1953

Dewberry
Fairfax, Virginia
www.dewberry.com
Member Since: 1/1985

Environmental Research Incorporated
Linden, Virginia
www.eri.us.com
Member Since: 8/2008

Esri
Redlands, California
www.esri.com
Member Since: 1/1987

GeoCue Group
Madison, Alabama
http://www.geocue.com
Member Since: 10/2003

Geographic Imperatives LLC
Centennial, Colorado
Member Since: 12/2020

GeoWing Mapping, Inc.
Richmond, California
www.geowingmapping.com
Member Since: 12/2016

Halff Associates, Inc.
Richardson, Texas
www.halff.com
Member Since: 8/2021

Keystone Aerial Surveys, Inc.
Philadelphia, Pennsylvania
www.kasurveys.com
Member Since: 1/1985

Kucera International
Willoughby, Ohio
www.kucerainternational.com
Member Since: 1/1992

L3Harris Technologies
Broomfield, Colorado
www.l3harris.com
Member Since: 6/2008

Merrick & Company
Greenwood Village, Colorado
www.merrick.com/gis
Member Since: 4/1995

NV5 Geospatial
Sheboygan Falls, Wisconsin
www.quantumspatial.com
Member Since: 1/1974

Pickett and Associates, Inc.
Bartow, Florida
www.pickettusa.com
Member Since: 4/2007

Riegl USA, Inc.
Orlando, Florida
www.rieglusa.com
Member Since: 11/2004

Robinson Aerial Surveys, Inc.(RAS)
Hackettstown, New Jersey
www.robinsonaerial.com
Member Since: 1/1954

Sanborn Map Company
Colorado Springs, Colorado
www.sanborn.com
Member Since: 10/1984

Scorpius Imagery Inc.
Newark, Delaware
aerial@scorpiusimagery.com
Member Since: 6/2021

Surdex Corporation
Chesterfield, Missouri
www.surdex.com
Member Since: 12/2011

Surveying And Mapping, LLC (SAM)
Austin, Texas
www.sam.biz
Member Since: 12/2005

T3 Global Strategies, Inc.
Bridgeville, Pennsylvania
https://t3gs.com/
Member Since: 6/2020

Terra Remote Sensing (USA) Inc.
Bellevue, Washington
www.terraremote.com
Member Since: 11/2016

Towill, Inc.
San Francisco, California
www.towill.com
Member Since: 1/1952

Woolpert LLP
Dayton, Ohio
www.woolpert.com
Member Since: 1/1985

SUSTAININGMEMBERBENEFITS

Membership

- ✓ Provides a means for dissemination of new information
- ✓ Encourages an exchange of ideas and communication
- ✓ Offers prime exposure for companies

Benefits of an ASPRS Membership

- Complimentary and discounted Employee Membership*
- E-mail blast to full ASPRS membership*
- Professional Certification Application fee discount for any employee
- Member price for ASPRS publications
- Discount on group registration to ASPRS virtual conferences
- Sustaining Member company listing in ASPRS directory/website
- Hot link to company website from Sustaining Member company listing page on ASPRS website

- Press Release Priority Listing in *PE&RS* Industry News
- Priority publishing of Highlight Articles in *PE&RS* plus, 20% discount off cover fee
- Discount on *PE&RS* advertising
- Exhibit discounts at ASPRS sponsored conferences (exception ASPRS/ILMF)
- Free training webinar registrations per year*
- Discount on additional training webinar registrations for employees
- Discount for each new SMC member brought on board (Discount for first year only)

*quantity depends on membership level

LEARN
DO
GIVE
BELONG

ASPRS

ASPRS Offers

» Cutting-edge conference programs

» Professional development workshops

» Accredited professional certifications

» Scholarships and awards

» Career advancing mentoring programs

» *PE&RS*, the scientific journal of ASPRS

asprs.org